High-resolution focal-plane wavefront sensing for time-varying aberrations

Piscaer, P.J.

DOI
10.4233/uuid:6b3801df-3151-4f7e-a04e-419d5460e84a

Publication date
2021

Document Version
Final published version

Citation (APA)
Piscaer, P. J. (2021). *High-resolution focal-plane wavefront sensing for time-varying aberrations*. [Dissertation (TU Delft), Delft University of Technology]. https://doi.org/10.4233/uuid:6b3801df-3151-4f7e-a04e-419d5460e84a

HIGH-RESOLUTION FOCAL-PLANE WAVEFRONT SENSING FOR TIME-VARYING ABERRATIONS

HIGH-RESOLUTION FOCAL-PLANE WAVEFRONT SENSING FOR TIME-VARYING ABERRATIONS

Proefschrift

ter verkrijging van de graad van doctor
aan de Technische Universiteit Delft,
op gezag van de Rector Magnificus Prof. dr. ir. T.H.J.J van der Hagen,
voorzitter van het College voor Promoties,
in het openbaar te verdedigen op woensdag 9 juni 2021 om 10:00 uur

door

Pieter Johan PISCAER

Master of Science in Systems and Control, Technische Universiteit Delft, Nederland
geboren te Vlissingen, Nederland.

Dit proefschrift is goedgekeurd door de promotor

Samenstelling promotiecommissie:

Rector Magnificus,	voorzitter
Prof. dr. ir. M. Verhaegen	Technische Universiteit Delft, promotor
Onafhankelijke leden:	
Prof. dr. ir. J.W. van Wingerden	Technische Universiteit Delft
Prof. dr. ir. A.W. Heemink	Technische Universiteit Delft
Prof. dr. F. Gustafsson	Linköping University
Dr. P. Massioni	Institut National des Sciences Appliquées de Lyon
Prof. dr. ir. N.J. Doelman	Universiteit Leiden
Overige leden:	
Dr. O.A. Soloviev	Technische Universiteit Delft

The research leading to these results has received funding from the European Research Council under the European Union's Seventh Framework Programme (FP7/2007- 2013). ERC grant agreement 339681.

Keywords: adaptive optics, focal-plane wavefront sensing, phase retrieval, Kalman filtering, large-scale optimization.

ISBN 978-94-6419-234-6

An electronic version of this dissertation is available at
http://repository.tudelft.nl/.

ACKNOWLEDGEMENTS

I would like to thank a number of people who have helped and supported me in every way possible during the past few years.

First, I would like to thank Michel Verhaegen for giving me the opportunity to do this research and without whose expertise, ideas and feedback, this thesis would have not been possible. I would also like to thank Oleg for all the help and interesting discussions that have significantly contributed to my research. For their insights and expertise that have influenced the course of my PhD, I would like to thank my other colleagues at DCSC with whom I have worked with: Baptiste, Carlas, Chengpu, Gleb, Kim, Manon, Reinier and Thao. I would also like to thank Francy, Heleen, Kiran, Kitty and Marieke for their support and for the organization of all the activities that makes for such a friendly working environment at DCSC. To the master students I had the pleasure of supervising: Abhimanyu, Daniel, Paulo and Wiegert, I would like to say that I have greatly enjoyed working with you and your research has been a very important part of my work as a PhD student.

Besides the ones already mentioned above, my thanks also go out to my other colleagues at DCSC: Barbara, Coen, Dean, Elisabeth, Hai, Hans, Huichen, Jacopo, Iurie, Jacques, Jelmer, Laurens, Lukasz, Markus, Nikos, Niloofar, Pascal, Paolo, Peter, Shrinivas, Sina, Tijmen, Tope, Vinod and Yasin. It has been a pleasure working with you all. Thank you for the interesting discussions that have kept my research on track, the daily table football matches that cleared my head and our sometimes ridiculous conversations that have lightened up my breaks. I have enjoyed the dinners, drinks and board game nights that have resulted in many friendships. After almost a year of social distancing and working from home, it is these things that I value and miss the most.

Furthermore, I would like to thank some of my other friends who have supported me. Thank you Katerina for being the best housemate I could imagine. Thank you Bart, Dylan, Mark and Mike for occasionally disturbing me during my work to get a cup of coffee and for the continued friendship. I also want to thank Jasper, Sander, Thierry and Thomas, whose friendship of fifteen years is still as strong as ever.

Finally, I would like to thank my parents and my sister for always supporting and believing in me throughout my whole life. It is because of your support that I have come this far. And Thea, thank you for being wonderful and for being there for me, during both the happy and stressful times.

Pieter Piscaer
Delft, January 2021

CONTENTS

Acknowledgements v

Summary xi

Samenvatting xiii

1 Introduction 1
- 1.1 Imaging through atmospheric turbulence . . . 1
  - 1.1.1 Image formation and phase aberrations . . . 1
  - 1.1.2 Atmospheric turbulence . . . 3
- 1.2 The phase retrieval problem . . . 5
  - 1.2.1 The principles of phase retrieval . . . 5
  - 1.2.2 Phase retrieval as a least squares problem . . . 7
  - 1.2.3 Phase retrieval algorithms . . . 8
  - 1.2.4 Modal representation using basis functions . . . 10
- 1.3 Adaptive optics . . . 12
  - 1.3.1 The main idea of adaptive optics . . . 12
  - 1.3.2 Closing the loop . . . 16
  - 1.3.3 Focal-plane sensing and wavefront sensorless AO . . . 17
  - 1.3.4 Temporal dynamics in atmospheric turbulence . . . 19
- 1.4 Prediction for adaptive optics systems . . . 19
  - 1.4.1 Modelling the wavefront dynamics . . . 20
  - 1.4.2 Optimal prediction from WFS measurements . . . 21
  - 1.4.3 Prediction and focal-plane sensing . . . 23
- 1.5 Structured modelling for large-scale adaptive optics systems . . . 24
  - 1.5.1 Sparsity structures in AO systems . . . 24
  - 1.5.2 System matrices as a sum of Kronecker product . . . 26
  - 1.5.3 The importance of the FFT algorithm . . . 27
  - 1.5.4 Other matrix structures . . . 27
- 1.6 Motivation and outline of the thesis . . . 28
  - 1.6.1 Motivation of the thesis . . . 28
  - 1.6.2 Outline of the thesis . . . 30

References . . . 33

2 Modal-based phase retrieval using Gaussian radial basis functions 41
- 2.1 Introduction . . . 42
- 2.2 Modal based phase retrieval . . . 43
  - 2.2.1 Extended Nijboer-Zernike polynomials . . . 44
  - 2.2.2 Gaussian radial basis functions . . . 45
  - 2.2.3 Phase retrieval as an optimization problem . . . 46

2.3 Simulation Design . . . 47
2.3.1 Generation of low-order aberrations . . . 47
2.3.2 Generation of high-order aberrations . . . 48
2.3.3 Approximating the generalized pupil function . . . 49
2.3.4 Phase retrieval experiment . . . 49
2.4 Fitting accuracy of GRBF . . . 50
2.4.1 Node distribution . . . 51
2.4.2 Shape parameter . . . 51
2.4.3 Comparison to ENZ . . . 53
2.5 Phase retrieval simulation results . . . 53
2.5.1 Low- and high-order aberrations . . . 53
2.5.2 Non-circular aperture . . . 55
2.5.3 Gaussian measurement noise . . . 56
2.6 Conclusion . . . 58
References . . . 59

3 Phase retrieval of large-scale time-varying aberrations using a non-linear Kalman filtering framework 61
3.1 Introduction . . . 62
3.2 Modelling the AO system . . . 63
3.2.1 Overview of the AO system . . . 63
3.2.2 Dynamic aberration model . . . 66
3.2.3 Measurement noise model . . . 66
3.3 Structures and efficient computations in AO systems . . . 67
3.3.1 Identification of structured matrices in dynamic aberration models . . . 67
3.3.2 Efficient computations of the output equation . . . 69
3.4 Kalman filters for WFSless AO . . . 69
3.4.1 Kalman filtering and the phase retrieval problem . . . 70
3.4.2 Solving the phase retrieval problem using a Kalman filter . . . 71
3.4.3 Advantage dynamic versus static approach . . . 71
3.5 Efficient Non-linear Kalman filter implementation . . . 72
3.5.1 State measurement update . . . 73
3.5.2 Error-covariance measurement update . . . 74
3.5.3 Error-covariance time update . . . 75
3.6 Simulation design . . . 76
3.7 Results . . . 77
3.7.1 Computational efficiency . . . 77
3.7.2 Influence of the wavefront dynamics and RMS-value . . . 77
3.7.3 Robustness to measurement noise . . . 78
3.8 Conclusions . . . 80
References . . . 80

4 Predictive wavefront sensorless adaptive optics for time-varying aberrations 85
4.1 Introduction . . . 86
4.2 Second moment-based wavefront sensorless adaptive optics . . . 87
4.2.1 Static aberration correction . . . 88

4.2.2 Challenges for time-varying aberrations . . . 89
4.2.3 Diagonalizing the linear system . . . 90
4.3 Predictive second moment-based WFSless AO . . . 90
4.3.1 Dynamic aberration model . . . 91
4.3.2 Kalman filter implementation . . . 92
4.3.3 Optimal control . . . 94
4.3.4 Actuator selection algorithm . . . 95
4.4 Simulation of AO for atmospheric turbulence . . . 96
4.4.1 Adaptive optics simulation design . . . 96
4.4.2 Measurement noise . . . 97
4.5 Simulation results . . . 98
4.5.1 Increasing wind speed . . . 98
4.5.2 Number of images in output . . . 100
4.5.3 Stronger aberrations . . . 101
4.5.4 Noise sensitivity . . . 101
4.6 Conclusion . . . 102
References . . . 103

5 Conclusions and future research **105**
5.1 Conclusions . . . 105
5.2 Future research . . . 108

Curriculum Vitæ **113**

List of Publications **115**

SUMMARY

Phase aberrations in optical systems, which occur in various applications such as astronomy, microscopy and ophthalmology, degrade the quality of obtained images. The exact cause and nature of the aberrations depends on the application. In astronomy, turbulence within the Earth's atmosphere creates fluctuations of the refractive index, leading to phase aberrations.

In order to compensate for the distorting effect of aberrations, adaptive optics (AO) systems are used to correct for phase aberrations in real-time. A deformable mirror (DM) is often used to apply the necessary corrections to improve the image quality. Due to the temporally dynamic nature of atmospheric turbulence and the corresponding phase aberrations, estimation errors caused by delays within the AO control loop are a significant part of the total estimation error. Accurate prediction of the phase aberrations is therefore an important aspect when aiming to improve the performance of AO systems.

Reconstructing the phase aberrations from focal plane images only is known as focal plane wavefront sensing. Many focal plane sensing methods are based on solving the phase retrieval problem, which is the problem of reconstructing the phase aberrations from the point spread function (PSF). Due to the non-linear optimization problem that underlies phase retrieval, developing real-time solvers is very challenging and a wavefront sensor (WFS) is often included to avoid the phase retrieval problem. Due to the linear relation between the phase aberration (i.e. wavefront) and WFS signal, WFS-based AO is often preferred over the wavefront sensorless (WFSless) AO systems that use focal plane sensing. There are, however, also a number of disadvantages. First, the addition of extra hardware components, including the WFS and a beam splitter, makes the system more complex and expensive than WFSless systems. Second, splitting the light between the focal plane camera and WFS results in non-common path aberrations (NCPAs), which can be a limiting factor in high-resolution imaging systems.

This thesis addresses challenges in WFSless AO systems regarding the temporal evolution of the phase aberrations to obtain accurate predictions and the development of computationally efficient methods. Three methods are presented.

Firstly, a method is presented which reduces the number of variables in the phase retrieval problem by representing the complex-valued generalized pupil function (GPF) as a linear combination of Gaussian radial basis functions (GRBFs). The almost local character of the GRBFs make them a flexible basis with respect to the pupil geometry and a suitable modal decomposition when representing aberrations with higher spatial frequencies.

Secondly, a method to obtain a high-resolution prediction of time-varying aberrations using a single focal plane image is presented. By reformulating phase retrieval for temporally dynamic aberrations into a non-linear Kalman filtering framework, this method is able to obtain more accurate predictions. The knowledge of a model for the aberration dynamics is shown to be a valuable source of prior information that can help

with problems regarding uniqueness and convergence. An efficient implementation of a non-linear Kalman filter algorithm is presented, whose computational complexity scales almost linearly with the number of pixels of the focal plane camera.

Thirdly, another predictive WFSless AO method is presented, which relies on the linear relation between the mean square of the aberration gradient and the change in second moment of the PSF. By applying a Kalman filter, this method is able to predict and compensate for time-varying aberrations using a single focal plane image. Only a small number of DM actuators are updated based on new measurements each sampling time, where the information provided by the Kalman filter is used to select the actuators that are expected to lead to the largest improvements in performance. An optimal controller is designed to sequentially update these selected DM modes.

SAMENVATTING

Fase-aberraties in optische systemen komen voor in verschillende toepassingen zoals astronomie, microscopie en oftalmologie, en verminderen de beeldkwaliteit. De exacte oorzaak en aard van de afwijkingen is afhankelijk van de toepassing. In astronomie worden de fase-aberraties veroorzaakt door fluctuaties van de brekingsindex wegens turbulentie in de atmosfeer van de aarde.

Adaptieve optica (AO) systemen worden gebruikt om in real-time te compenseren voor het verstorende effect van fase-aberraties. Vaak wordt een vervormbare spiegel gebruikt om de nodige correcties aan te brengen en zo de beeldkwaliteit te verbeteren. Vanwege de dynamische aard van atmosferische turbulentie en de bijbehorende fase-aberraties, zijn fouten die worden veroorzaakt door vertragingen binnen de AO-regellus een significant deel van de totale schattingsfout. Een nauwkeurige voorspelling van de fase-aberratie is daarom een belangrijk aspect van het verbeteren van de prestaties van AO-systemen.

Het reconstrueren van de fase-aberraties met alleen brandvlakbeelden staat bekend als *focal plane wavefront sensing* (brandvlak golffront detectie). Veel brandvlakdetectiemethoden zijn gebaseerd op het oplossen van het *phase retrieval* probleem (faseherstelprobleem): het reconstrueren van de fase-aberraties van de puntspreidingsfunctie (PSF). Vanwege het niet-lineaire optimalisatieprobleem dat ten grondslag ligt aan het *phase retrieval* probleem, is het ontwikkelen van real-time algoritmes een grote uitdaging en wordt er vaak een *wavefront sensor* (golffrontsensor), WFS, gebruikt om het *phase retrieval* probleem te vermijden. Door de lineaire relatie tussen de fase-aberraties en het WFS-signaal, heeft op WFS gebaseerde AO vaak de voorkeur boven de *wavefront sensorless* (golffrontsensorloze), WFSless, AO-systemen die gebruikmaken van *focal plane sensors*. Er zijn echter ook een aantal nadelen. Ten eerste maakt de toevoeging van extra hardwarecomponenten, waaronder de WFS en een *beam splitter*, het systeem complexer en duurder dan *WFSless*-systemen. Ten tweede resulteert het splitsen van het licht tussen de *focal plane* camera en WFS in *non-common path* aberraties (NCPAs), die een beperkende factor kunnen zijn in beeldvormingssystemen met hoge resolutie.

Dit proefschrift behandelt uitdagingen in *WFSless* AO-systemen met betrekking tot het verkrijgen van nauwkeurige voorspellingen van dynamische fase-aberraties en het ontwikkelen van computationeel efficiënte *phase retrieval* algoritmes. Er worden drie methoden gepresenteerd.

Eerst wordt een methode gepresenteerd die het aantal variabelen in het *phase retrieval* vermindert door de gegeneraliseerde pupilfunctie (GPF) voor te stellen als een lineaire combinatie van Gaussische radiale basisfuncties (GRBFs). Het lokale karakter van de GRBFs maakt ze een flexibele basis met betrekking tot de vorm van de pupil en een geschikte modale decompositie voor het benaderen van aberraties met hogere ruimtelijke frequenties.

Ten tweede wordt een methode gepresenteerd om in hoge resolutie tijdsvariërende aberraties te voorspellen met behulp van een enkel brandvlakbeeld. Door *phase retrieval* voor temporeel dynamische aberraties te herformuleren in een niet-lineair Kalman-filterraamwerk, is deze methode in staat om nauwkeurigere voorspellingen te verkrijgen. Het hebben van een dynamisch model van de aberratie blijkt een waardevolle bron van informatie te zijn die kan helpen bij problemen zoals uniciteit en convergentie. Daarnaast wordt er een efficiënte implementatie van een niet-lineair Kalman-filteralgoritme gepresenteerd, waarvan de rekencomplexiteit bijna lineair schaalt met het aantal pixels van de camera.

Ten derde wordt een andere voorspellende *WFSless* AO-methode gepresenteerd, die berust op de lineaire relatie tussen het gemiddelde kwadraat van de aberratiegradiënt en de verandering in het tweede moment van de PSF. Door gebruikt te maken van een Kalman-filter kan deze methode dynamische aberraties voorspellen en corrigeren met behulp van een enkel brandvlakbeeld. Per tijdsstap wordt slechts een klein aantal spiegelactuatoren in *real-time* bijgewerkt op basis van nieuwe metingen, waarbij de informatie van de Kalman-filter wordt gebruikt om de spiegelactuatoren te selecteren die naar verwachting tot de grootste prestatieverbeteringen zullen leiden. Ook is een optimale controller ontworpen om deze geselecteerde spiegelactuatoren bij te werken.

1

INTRODUCTION

This chapter contains the necessary background information of the remaining chapters in this thesis. The applications that are central to this thesis are static wavefront reconstruction and phase retrieval on one side, and optimal prediction and control for dynamic aberrations in AO systems on the other. Besides the basics of imaging and adaptive optics, it will present several insights relevant to these applications in the field of linear algebra, system modelling, system identification and Kalman filter theory as well as an analysis of the current problems with prediction and phase retrieval methods in AO systems. Since the theory will always be paired to an application, they will be introduced as such. Section 1.1 will introduce the basics of imaging atmospheric turbulence. Section 1.2 presents the phase retrieval problem and contains an overview of existing methods to solve it. Afterwards, the main applications of the theory presented in this thesis, adaptive optics (AO), is introduced in Section 1.3. Section 1.4 will continue on this topic and focuses on the methods used to predict temporal dynamic aberrations for AO systems and will address the importance of accurately modelling the aberration dynamics. The problems with existing methods for large-scale AO systems will be discussed in Section 1.5, here an overview of the recent advances of structured modelling of AO systems to decrease this computational burden is presented. Finally, the motivation and structure of this thesis will be presented in Section 1.6.

1.1. IMAGING THROUGH ATMOSPHERIC TURBULENCE

Before focusing on the challenges arising in adaptive optics systems, an introduction to some basic theory regarding imaging through atmospheric turbulence is given.

1.1.1. IMAGE FORMATION AND PHASE ABERRATIONS

This thesis focuses on phase aberrations caused by atmospheric turbulence in optical systems for astronomy. The representation of optical systems using Fourier optics is central to this thesis. There exists many textbooks and papers that treat Fourier optics and optical image formation in detail [1–4], the reader is referred to these works if more

background knowledge is required.

The resolution of imaging through atmospheric turbulence is defined by two main factors. Firstly, due to the finite size of the aperture, diffraction becomes a limiting factor on the resolution. Secondly, *phase aberrations* to the optical field has a deteriorating effect on the image. These phase aberrations are caused by changes in the refractive index due to turbulent air, which will be further discussed in Section 1.1.2. The complex optical field at the telescope aperture, also known as the *generalized pupil function* (GPF), will be defined as follows:

$$X(\rho,\theta) = A(\rho,\theta)exp(i\Phi(\rho,\theta)), \tag{1.1}$$

where ρ,θ are the polar coordinates in the pupil plane and $A(\rho,\theta)$ and $\Phi(\rho,\theta)$ are the amplitude apodisation function and phase aberration respectively.

When the propagation distance of the light between the pupil and focal plane is sufficiently large, the obtained image can be accurately approximated by the *Fraunhofer diffraction integral* [2, 3]. This approximation states that the field in the back focal plane is proportional to the Fourier transform of the GPF, i.e. when defining $\mathscr{F}_c(\cdot)$ as the two-dimensional (continuous) Fourier transform, the complex field at the focal plane becomes

$$I(\zeta,\omega) \propto \mathscr{F}_c\big(X(\rho,\theta)\big), \tag{1.2}$$

where ζ,ω are polar coordinates in the focal plane. The intensity of this field is known as the *point spread function* (PSF), as it can be seen as the image of a point source. Denoting the PSF by Y, it is defined by the following non-linear relation:

$$Y(\zeta,\omega) \propto |\mathscr{F}_c\big(X(\rho,\theta).\big)|^2. \tag{1.3}$$

When there are no phase aberrations, i.e. $\Phi = 0$, diffraction due to finite the aperture size creates an image known as the *Airy disk* [4]. When introducing the angular distance, $\psi = \zeta/f$, f being the focal length of the lens, the Airy disk is described by

$$Y_a(\psi) = \frac{\pi D^2}{4\lambda^2}\left(\frac{2J_1(\pi D\psi/\lambda)}{\pi D\psi/\lambda}\right)^2 \tag{1.4}$$

where J_1 is the Bessel function of the first kind. The first dark ring of the Airy disk is located at an angular distance of $1.22\lambda/D$ rad from the center. This distance is significant as it defines the *Rayleigh resolution criterion*, stating that objects at an angular distance smaller than $1.22\lambda/D$ can no longer be distinguished.

When considering an extended object instead of a point source and assuming incoherent illumination, the image in the focal plane is given by the convolution between the object intensity and the PSF. Hence, the PSF can be seen as the smoothing or blurring effect on the projection of the object onto the image plane. This also means that the PSF can be used as a measure of the quality of the image of interest. Typically, the "width" of the PSF is an important measure for the resolution of an optical system. Often, measures such as the *full width at half maximum* (FWHM), *Encircled energy* and *Strehl ratio* are used to quantify this width. This thesis will occasionally use the notion of the Strehl

ratio, defined as the ratio between the aberrated PSF and the aberration free PSF. Often, the Strehl ratio S and the mean squared error of the phase σ_ϕ^2 are related via the *extended Marechal approximation*, stating that

$$S \approx \exp\left(-\sigma_\phi^2\right), \tag{1.5}$$

which is considered to be valid as long as $\sigma_\phi^2 \lesssim 4$ rad [4]. This shows that maximizing the Strehl ratio also means that the phase variance is minimized [5]. Because of this direct relation, σ_ϕ^2 will commonly be used as a measure of the resolution of the imaging system, but this can be converted into an expression of S via (1.5).

When the Fourier transform of the PSF is taken, the *optical transfer function* (OTF) is obtained [4]. The OTF is a complex valued function that gives useful insights into the range of spatial frequencies the imaging system is able to see. Due to the finite aperture, the amplitude of the OTF is zero for any frequency larger than D/λ, known as the *cut-off frequency*. In the absence of phase aberrations, this cut-off frequency defines the resolution of the imaging system and such systems are referred to as *diffraction limited*. In contrast, for very large aperture diameters D, the phase aberrations become the limiting factor. These systems are called *seeing limited*. In astronomy, the cause of these phase aberrations is turbulence inside the Earth's atmosphere.

1.1.2. ATMOSPHERIC TURBULENCE

The main cause of phase aberrations in AO systems for astronomy is caused by fluctuations of the refractive index in the Earth's atmosphere. The behaviour of the atmospheric turbulence is commonly modelled statistically, because the process has too many random variables to formulate a closed-form solution. The most well-known model of the effect of turbulence on the wavefront was presented almost a century ago by Kolmogorov [6] and has often been clearly summarized and explained in literature [3].

The central idea in the Kolmogorov turbulence model is that kinetic energy in pockets of air, called eddies, is transferred into smaller eddies. The outer scale L_0 is used to define the average size of the largest eddies, whereas the inner scale l_0 represents the average size of the smallest eddies. When considering a scale smaller than the inner scale, the turbulence is no longer self-sustaining due to energy dissipation caused by friction.

Phase aberrations perceived by a telescope are related to the change of refractive index via the following integral:

$$\phi(x,y,z) = \frac{2\pi}{\lambda}\int_0^\infty n(x,y,z)\,dz, \tag{1.6}$$

where z is the spatial coordinate in the direction of propagation of the light, x, y are the spatial coordinates orthogonal to z and λ is the wavelength. According to Kolmogorov's model, the change of refractive index between two points in space, $\boldsymbol{\rho} \in \mathbb{R}^3$ and $\boldsymbol{\rho} + \Delta\boldsymbol{\rho}$, only depends on their absolute distance $\Delta\rho = |\Delta\boldsymbol{\rho}|$ apart. The change is often represented by a statistical measure of random fields called a *structure function*, which is closely related to its auto-correlation. The refractive index structure function $D_n(\Delta\boldsymbol{\rho})$, following Kolmogorov's model, is defined as

$$D_n(\Delta\boldsymbol{\rho}) = \int \left(n(\boldsymbol{\rho}) - n(\boldsymbol{\rho}+\Delta\boldsymbol{\rho})\right)^2 d\boldsymbol{\rho} = C_n^2 \Delta\rho^{2/3}, \tag{1.7}$$

where C_n is called the refractive index structure parameter, which generally varies with the height above the ground. Due to this dependency on the height above the ground, the total atmosphere is usually represented by a finite number of discrete thin layers at different heights, called *phase screens*. For each phase screen, a structure function for the phase difference defined in (1.6) can be formulated. This so-called phase structure function can be found to equal

$$D_\phi(\Delta\boldsymbol{\zeta}) = 6.88\frac{\Delta\zeta}{r_0}, \tag{1.8}$$

where $\Delta\boldsymbol{\zeta} \in \mathbb{R}^2$ is the vector between two points within the phase screen and $\Delta\zeta = |\Delta\boldsymbol{\zeta}|$. The parameter r_0 is called the *Fried parameter* [7], and is a measure of the turbulence strength along the line of sight for a specific wavelength λ, where a smaller value of r_0 indicates more severe atmospheric conditions. Typical values of r_0 range from 5 cm to 20 cm depending on the atmospheric conditions. The ratio of the telescope diameter D over the Fried parameter defines the severity of the aberrations on the optical system. Assuming the Kolmogorov model, it follows that [8]

$$\sigma_\phi^2 = \left(\frac{D}{r_0}\right)^{5/3}. \tag{1.9}$$

One interpretation of the Fried parameter is that the RMS phase aberration over a circle of diameter r_0 (i.e. $D = r_0$ in the equation above) is approximately 1 rad. As a consequence, for a telescope with a diameter larger than r_0, the phase aberration will become the limiting factor on the system's resolution instead of the diffraction limit. Increasing the telescope diameter will not lead to a better resolution, which shows the importance of compensating for phase aberrations for larger ground based telescopes.

The power spectral density (PSD) of the phase aberrations can be derived from the structure function. The PSD for the Kolmogorov model is

$$\Psi_\phi^K(\kappa) = 0.49 r_0^{-5/3}\kappa^{-11/3}, \tag{1.10}$$

showing that the power is larger for smaller values of the *angular spatial frequency* κ in rad/m. This insight can be used to show that the main contribution within the phase aberration is caused by modes with lower spatial frequencies [8]. This insights implies that, rather than a zonal basis, a modal basis might be an efficient way to represent the wavefront aberrations caused by turbulence using a smaller number of variables, see also Section 1.2.4 for more details on a modal representation of the wavefront. However, it should be noted that this expression is only valid for κ within the range $1/L_0 \ll \kappa \ll 1/l_0$. Other models have been proposed to represent the PSDs, including the Von Karman model [3, 9], which is also used for simulation purposes throughout this thesis. The Von Karman PSD takes into account the saturation given by the outer scale L_0:

$$\Psi_\phi^{VK}(k) = \left(0.49 r_0^{-5/3}\right)\left(\kappa^2 + \kappa_0^2\right)^{-11/6}, \tag{1.11}$$

where $\kappa_0 = 2\pi/L_0$. The covariance function of the phase aberration can be deduced from the PSD. For the Von Karman model, the covariance function can be shown to equal [10]

$$C_\phi(\Delta\zeta) = \alpha\left(\frac{L_0}{r_0}\right)^{5/3}\left(\frac{2\pi\Delta\zeta}{L_0}\right)^{5/6}\mathcal{K}_{5/6}\left(2\pi\frac{\Delta\zeta}{L_0}\right), \tag{1.12}$$

where $\mathcal{K}_{5/6}$ is the modified Bessel function of the third type and α is a constant: $\alpha = \Gamma(11/6)2^{-5/6}\pi^{8/3}(24/5\Gamma(6/5))^{5/6}$. Finally, the modified Von Karman model includes the influence of both the inner and outer scale on the PSD [3, 9]:

$$\Psi_\phi^{mVK}(\kappa) = \left(0.49 r_0^{-5/3}\right) \exp\left(-\kappa^2/\kappa_m^2\right) \left(\kappa^2 + \kappa_0^2\right)^{-11/6}, \tag{1.13}$$

with $\kappa_m = 5.92/l_0$.

Kolmogorov's model only describes the spatial changes of the phase aberrations. However, atmospheric turbulence also is subject to temporal changes. These temporal changes, or *temporal dynamics*, of the wavefront can be represented using *Taylor's frozen flow hypothesis* [11], which states that each phase screen moves at a constant speed in a constant direction. When considering multiple layers, the overal windspeed can be approximated by a weighted average velocity:

$$\bar{v} = \left(\frac{\int C_n^2(z) |v(z)|^{5/3} dz}{\int C_n^2(z) dz} \right)^{5/3}. \tag{1.14}$$

The time it takes for the turbulence to move a distance r_0, is called the coherence time $\tau_0 = r_0/\bar{v}$ and it plays an important role in quantifying the strength of the turbulence dynamics.

A technique that aims to correct for these phase aberrations is *adaptive optics* (AO) [4, 12, 13], which will be discussed in Section 1.3.

1.2. THE PHASE RETRIEVAL PROBLEM

The previous section discussed how phase aberrations deteriorate the image quality in telescopes. This section will discuss the problem that aims to retrieve the phase aberration from one or multiple PSF measurements.

1.2.1. THE PRINCIPLES OF PHASE RETRIEVAL

When observing the image of a point source though a distorting medium, a camera would capture the aberrated PSF defined in (1.3). As discussed in Section 1.1.1, it is common in optical systems with large apertures, such as large ground-based telescopes, for the aberrations to be the limiting factor on the resolution of the optical system. Therefore, the phase aberrations have to be compensated for in order to obtain a higher resolution. As a consequence, estimating the existing phase aberrations (or the complete GPF) becomes a topic of interest. Reconstructing the phase aberrations from the PSF is known as the phase retrieval problem and is widely studied in literature, see [14, 15] for a recent overview.

Unfortunately, cameras only capture the amplitude of the complex field I. If the full complex field in the image plane would be known, the GPF could simply be calculated by applying the two-dimensional inverse-DFT operator on this complex field. This relation shows that finding the GPF is trivial as soon as the phase of I is known, such that this problem is also known as the phase retrieval problem.

The most general formulation of the phase retrieval problem is to define it as the problem of obtaining a complex vector $\boldsymbol{x} \in \mathbb{C}^n$ based on a set of measurements:

$$y_i = |\langle \boldsymbol{f_i}, \boldsymbol{x} \rangle|^2, \; k = 1, \ldots, p \,, \tag{1.15}$$

1

where $\boldsymbol{f}_i \in \mathbb{C}^n$ will be referred to as *measurement vectors*. In the case of Fourier optics, the problem is also known as Fourier phase retrieval, where the elements in the measurement vectors $\boldsymbol{f}_i$ are based on the underlying relation given by the two-dimensional Fourier transform as in (1.3).

Compared to the notation of the theory introduced in Section 1.1.1, a clear difference is that the phase retrieval problem considers a (discrete) vector representation of the problem, rather than the (continuous) functions that were used to define the relation between the GPF and PSF in (1.3). The PSF is usually captured using a charge-coupled device (CCD) camera, which is a photon detector that captures the arriving photons on a discrete grid of pixels. By sampling the output of the function in (1.3), the relation can be rewritten using the *discrete Fourier transform* (DFT) instead:

$$Y = |\mathscr{F}(X)|^2, \tag{1.16}$$

where $Y \in \mathbb{R}^{\bar{p}\times\bar{p}}$, $X \in \mathbb{C}^{\bar{n}\times\bar{n}}$ are the sampled PSF and GPF respectively and $\mathscr{F}$ represents the *oversampled two-dimensional DFT*, such that $\bar{p} > \bar{n}$. The reason for this oversampling is to satisfy the *Nyquist sampling theorem* in order to avoid aliasing. This theorem states that, when the measurements are performed on a $\bar{p} \times \bar{p}$ grid of pixels, the highest resolution grid on which the GPF can be reconstructed is of size $\bar{n} \times \bar{n}$ with $\bar{n} = \bar{p}/2$.

The oversampled DFT can be computed by applying the DFT on a matrix $X_p \in \mathbb{C}^{\bar{p}\times\bar{p}}$, which is constructed by zero-padding the matrix X around the edges to the corresponding size. This means that in practice, the resolution of the reconstruction is always limited to half the resolution of the camera capturing the PSF. Often, a vectorized formulation of the (1.16) will be used, which is defined as

$$\boldsymbol{y} = |\mathscr{F}_{vec}(\boldsymbol{x})|^2, \tag{1.17}$$

such that $\boldsymbol{y} \in \mathbb{R}^p$, $\boldsymbol{x} \in \mathbb{C}^n$, $p = \bar{p}^2$ and $n = \bar{n}^2$. The operator $\mathscr{F}_{vec}$ represents the vectorized formulation of the DFT, i.e. $\mathscr{F}_{vec}(\boldsymbol{x}) = vec(\mathscr{F}(X))$.

The one-dimensional DFT can be expressed as a matrix-vector multiplication by using the *DFT matrix* D. Also here, oversampling is assumed with $p = 2n$, such that the resulting DFT matrix will be of dimensions $D \in \mathbb{C}^{\bar{p}\times\bar{n}}$. For the two-dimensional DFT, (1.17) can be reformulated as the intensity of a matrix-vector product as follows:

$$\boldsymbol{y} = |F\boldsymbol{x}|^2, \tag{1.18}$$

where $F := D \otimes D$, with $\otimes$ being the Kronecker product. Notice that, considering the standard definition of (1.15), the matrix F contains all the vectors $\boldsymbol{f}_i$ on its rows.

Although this matrix formulation shows how the Fourier phase retrieval problem is a specific case of the general phase retrieval problem, the DFT is usually not computed via this matrix vector multiplication. Due to efficient algorithms such as the *fast Fourier transform* (FFT), computing the DFT via a matrix-vector multiplication is not computationally efficient. However, when only one (or a few) elements of the DFT have to be computed, this formulation becomes more efficient than computing the complete transform using the FFT.

1.2.2. PHASE RETRIEVAL AS A LEAST SQUARES PROBLEM

The above definition allows for the (Fourier) phase retrieval problem to be formulated as a *non-linear least-squares* problem:

$$\min_{\boldsymbol{x}\in\mathbb{C}^n} \left\| \boldsymbol{y} - |\mathscr{F}(\boldsymbol{x})|^2 \right\|_2^2. \tag{1.19}$$

Although this thesis will focus on the Fourier phase retrieval case, the theory presented in this section can easily be extended to other types of measurements.

The optimization problem in (1.19) is *non-convex*, making it more difficult to solve and it is often not possible to guarantee that the global optimum is found. Over the past decades, many different types of algorithms have been proposed to solve the phase retrieval problem, which will be discussed in Section 1.2.3. One major difficulty with the phase retrieval problem is that there is not a unique solution when only a single PSF image is available. For more information regarding the uniqueness of the phase retrieval problem, the reader is referred to the overview papers [14, 15] and the references therein.

The non-uniqueness has led to a large body of literature that considers the availability of possible prior information to the optimization problem of (1.19) [1]. Prior information can be used as a constraint to the optimization problem, which might not only overcome the uniqueness problem, but may also help with the general issue of having a non-convex cost function.

There are many possible sources that can give useful prior information. One possible source concerns knowledge of the amplitude of the GPF, $\boldsymbol{a}$ in (1.1). This could be knowledge of the support of the GPF, i.e. whether pixels are inside or outside the aperture, or (partial) knowledge of the values of $\boldsymbol{a}$. In general, prior information on the amplitude $\boldsymbol{a}$ can be included into the following constrained optimization problem:

$$\min_{\boldsymbol{x}\in\mathbb{C}^n} \|\boldsymbol{y} - |\mathscr{F}(\boldsymbol{x})|^2\| \tag{1.20}$$

$$\text{s.t.} \boldsymbol{a} \in \mathscr{A}, \tag{1.21}$$

where $\mathscr{A}$ defines the set of vectors that satisfies the prior knowledge of $\boldsymbol{a}$.

Another common method to obtain extra information is to increase the number of sensors. The availability of multiple simultaneous measurements with different additional known phase aberrations, known as *phase diversity* [16–18], is a frequently used technique to resolve uniqueness issues and improve the overall performance of phase retrieval algorithms. By taking multiple images along the optical axis around the focal plane, a known *defocus* phase aberration is added to each measurement. When adding a known phase aberration $\boldsymbol{\phi}_D$ to system, the observed PSF changes as follows:

$$\boldsymbol{y}_D = |\mathscr{F}\left(\boldsymbol{x} \odot \exp(j\boldsymbol{\phi}_D)\right)|^2 := |\mathscr{F}_D(\boldsymbol{x})|^2, \tag{1.22}$$

where the vector $\boldsymbol{\phi}_D$ is usually referred to as the phase diversity. By stacking the measurements into a larger vector, the phase diversity technique leads to the following opti-

mization problem:

$$\min_{\boldsymbol{x}\in\mathbb{C}^n} \left\| \begin{bmatrix} \boldsymbol{y}_{D_1} \\ \boldsymbol{y}_{D_2} \\ \vdots \\ \boldsymbol{y}_{D_L} \end{bmatrix} - \left| \begin{bmatrix} \mathscr{F}_{D_1}(\boldsymbol{x}) \\ \mathscr{F}_{D_2}(\boldsymbol{x}) \\ \vdots \\ \mathscr{F}_{D_L}(\boldsymbol{x}) \end{bmatrix} \boldsymbol{x} \right|^2 \right\|_2^2 \tag{1.23}$$

$$\text{s.t.} \boldsymbol{a} \in \mathscr{A}, \tag{1.24}$$

with the subscript D_ℓ denoting the ℓ-th measurement with diversity term $\boldsymbol{\phi}_{D_\ell}$.

Finally, when solving the phase retrieval problem over a time-series of phase aberrations, in which the aberrations slowly change over time, knowledge of the temporal behaviour of the wavefront can be used as a source of additional information. In Section 1.3, an application that deals with such temporally dynamic aberrations, called adaptive optics, is introduced. A common assumption in adaptive optics algorithms is that the temporal dynamics are constant between two consecutive measurements. It will be argued in Section 1.4 and further in Chapters 3 and 4 that accurately modelling the aberration dynamics and using this knowledge can significantly improve the performance of many adaptive optics algorithms.

1.2.3. PHASE RETRIEVAL ALGORITHMS

With the phase retrieval problem defined, this subsection focuses on the different classes of algorithms that have been developed over the past decades. Throughout this thesis, the many phase retrieval methods are divided into three categories: alternating projection methods, convex optimization-based methods and non-convex optimization-based methods. A detailed overview of phase retrieval algorithms can be found in [14, 15].

ALTERNATING PROJECTION METHODS

The earliest algorithms that were developed to solve the phase retrieval problem all belong to the so-called *alternating projection (AP)* methods. The pioneering work was done by Gerchberg & Saxton [19] and Fienup [20]. However, these early methods have severe limitations when high levels of noise are present. Over the years, many other algorithms have been introduced that aim to overcome these limitations [21–26]. A more detailed overview and explanation of projection methods and the difference between algorithms can be found in [1, 14, 27].

When applied to the Fourier phase retrieval problem, the required projections can be carried out efficiently using the fast Fourier transform (FFT). This makes alternating projection methods in many cases still the fastest class of methods to solve the Fourier phase retrieval problem. However, there are several drawbacks. First of all, there does not exist a global convergence result [28]. Furthermore, in contrast to the other classes to be presented, AP methods do not explicitly minimize a cost function, making them more difficult to use when certain prior knowledge has to be taken into account. This last item will become a bigger issue when dealing with a temporal dynamic wavefront as, for example, taking into account the prior information on the distribution of the stochastic variable $\boldsymbol{x}$ is more challenging.

CONVEX OPTIMIZATION METHODS

A different approach to solve the phase retrieval problem is to reformulate it using a convex relaxation of the non-linear optimization problem in (1.19). This class of methods was first presented after the realization that the relation in (1.15) can be reformulated as: $y_i = \text{trace}\left(\bar{F}_i \bar{X}\right)$, where $\bar{F}_i = \boldsymbol{f}_i \boldsymbol{f}_i^H$ and $\bar{X} = \boldsymbol{x}\boldsymbol{x}^H$. By replacing the original parameter vector $\boldsymbol{x}$ by rank 1 matrix $\bar{X}$, the measurement becomes linear in terms of this new higher dimensional variable. This technique is called "lifting" and was first used to solve the phase retrieval problem in the PhaseLift algorithm [29, 30]. Since $\bar{X}$ should be of rank 1, a rank constraint should be added to the optimization problem. However, due to the non-convexity of a rank constraint, a convex relaxation applied by replacing the rank constraint with its convex surrogate $\text{trace}(\bar{X})$, resulting in a complex semi-definite program. Once this has been solved for $\bar{X}$, an estimate for $\boldsymbol{x}$ can be retrieved form the singular value decomposition of $\bar{X}$.

Besides the PhaseLift algorithm, other algorithms have been presented that use convex relaxations of the original non-convex optimization problem, such as: PhaseCut [31], which uses a different convex relaxation, PhaseMax [32], which presents a convex optimization method that avoids lifting the variable and COPR [33], which is a fast iterative method for large-scale phase retrieval problems that also avoids lifting.

An important advantage of this class of phase retrieval methods is the existence of recovery guarantees. It has been shown that under certain conditions, the true solution is recovered with high probability [31, 34, 35]. These results often only hold for random measurement vectors, i.e. in cases where the vectors $\boldsymbol{f}_i$ in (1.15) would be drawn from a random distribution instead of given by the Fourier transform. However, numerical experiments have shown that they often perform well on certain structured non-random phase retrieval problems [31]. Despite the theoretical guarantees, convex optimization methods also have a number of drawbacks. Firstly, the methods are computationally demanding since lifting the variable means a quadratic increase in the number of unknowns, making them challenging to use for large-scale applications. Secondly, by substituting the true parameter vector with a quadratic expression, adding prior knowledge to the optimization problem is still not straightforward.

NON-CONVEX OPTIMIZATION METHODS

A third class of phase retrieval methods has gained a lot of attention in the past years. Starting with the Wirtinger flow algorithm [36], many algorithms have been formulated that solve the phase retrieval problem in its original non-convex optimization formulation using various non-linear optimization algorithms [37–41].

An advantage of these algorithms over AP methods is that there exist recovery guarantees under specific conditions. Usually, the convergence of the optimization algorithms heavily relies on accurate initializers, random measurement vectors and a sufficiently large number of measurements [36–38, 41]. Since these methods directly operate in the original parameter dimension, they have an advantage over the convex optimization methods in terms of algorithm run-time and storage requirements. However, for the Fourier phase retrieval case, finding an accurate initializer is often difficult, which causes problems regarding the convergence of the non-linear optimization algorithms.

1

1.2.4. MODAL REPRESENTATION USING BASIS FUNCTIONS

The introduction of the phase retrieval problem in Section 1.2 assumed that the GPF is reconstructed in terms of a zonal and discretized (i.e. pixel) basis. However, other types of basis functions have been used to represent the wavefront or GPF.

A general advantage of any modal decompositions is that it is an efficient way to decrease the number of parameters that are needed to characterize the wavefront or GPF, while maintaining the desired resolution of the reconstruction. Especially for computationally demanding phase retrieval methods, such as the (non-)convex optimization-based methods presented in Section 1.2.3, this decrease in computational burden can lead to significantly faster algorithms, see e.g. [33, 42]. Moreover, when the basis consists of smooth functions, a modal decomposition can be a way to enforce a certain smoothness in the reconstruction, which can be advantageous under noisy circumstances.

MODAL REPRESENTATION OF THE WAVEFRONT

As mentioned in Section 1.1.2, Kolmogorov's turbulence model states that the PSD of the wavefront decreases in value when the spatial frequency of a certain mode in the wavefront decreases. Therefore, choosing a modal basis instead of a zonal basis to represent the wavefront can be a good way to reduce the dimensionality of the phase retrieval problem.

The most well-known set of basis functions to represent the wavefront are the *Zernike polynomials* [8]. Representing the wavefront in terms of Zernike polynomials gives a modal decomposition of the wavefront in terms of a set of orthogonal basis functions:

$$\Phi(\rho,\theta) = \sum_{n,m} \zeta_n^m \mathcal{Z}_n^m(\rho,\theta), \tag{1.25}$$

where the indices $n \in \mathbb{N}_0$ and $m \in \mathbb{Z}$ denote the radial order and the azimuthal frequency of the Zernike polynomial $\mathcal{Z}_n^m$. The polynomials are the product of a radial polynomial $R_n^{|m|}(\rho)$ and a trigonometric function $\Theta_n^m(\theta)$,

$$\mathcal{Z}_n^m(\rho,\theta) = \alpha_n^m R_n^{|m|}\Theta_n^m(\theta), \tag{1.26}$$

with the following definitions of $R_n^m(\rho)$ and $\Theta_n^m(\theta)$:

$$\begin{aligned} \Theta_n^m(\theta) &= \begin{cases} cos(m\theta) & \text{for } m \geq 0 \\ -sin(m\theta) & \text{for } m < 0 \end{cases}, \\ R_n^m(\rho) &= \sum_{s=0}^{(n-m)/2} \frac{(-1)^s (n-s)!}{s!\left(\frac{n+m}{2}-s\right)!\left(\frac{n-m}{2}-s\right)!} \rho^{n-2s}. \end{aligned} \tag{1.27}$$

Throughout this thesis, the normalization coefficients α_n^m are given by

$$\alpha_n^m = \begin{cases} \sqrt{n+1} & \text{for } m = 0 \\ \sqrt{2(n+1)} & \text{for } m \neq 0 \end{cases}. \tag{1.28}$$

Due to the fact that Zernike polynomials are widely used in optics, a number of modes are given conventional names. This thesis will use the following names for the polynomials with indices (m,n): $(0,0)$ is called *piston*, $(1,1)$ *tip*, $(-1,1)$ *tilt* and $(0,2)$ is called

defocus. Defocus was mentioned before in Section 1.2 as one of the most common aberrations applied by the phase diversity method.

Zernike polynomials are particularly interesting when considering wavefront aberrations due to atmospheric turbulence since they can be ordered based on their spatial frequencies. This means that according to Kolmogorov's model, the modes with a small order n will be most prevalent in the wavefront [8]. For example, it was shown that when removing tip, tilt and defocus, the total phase variance of (1.9) is reduced from $1.029(D/r_0)^{5/3}$ to $0.111(D/r_0)^{5/3}$. Using this insight, the necessary order of the Zernike polynomials to represent the wavefront can be chosen, depending on the desired residual phase variance of the decomposition.

MODAL REPRESENTATION OF THE GPF

In the general phase retrieval problem, not only the wavefront, but the complete (complex-valued) GPF is reconstructed. Therefore, it can be desired to extend the modal basis to fit a complex valued field. By extending Zernike polynomials into the complex domain, the so-called *extended Nijboer-Zernike (ENZ)* polynomials are obtained [43, 44]. Using a set of complex-valued polynomials, the GPF can be approximated as a series of ENZ polynomials:

$$X(\rho,\theta) = \sum_{n,m} \beta_n^m \mathcal{N}_n^m(\rho,\theta). \tag{1.29}$$

n and m denote respectively the radial order and azimuthal frequency of the ENZ polynomial $\mathcal{N}_n^m(\rho,\theta)$, which is defined by

$$\mathcal{N}_n^m(\rho,\theta) = \sqrt{n+1} R_n^{|m|}(\rho) \exp(i m\theta). \tag{1.30}$$

Similar to the ordering of Zernike polynomials, also the ENZ polynomials can be ordered according to their radial order and they share similar advantageous properties with the real-valued Zernike polynomials. Although ENZ polynomials have been proven to be suitable polynomials in representing the GPF of an aberrated optical system, they have a number of drawbacks. First of all, they are defined on a circular aperture only, making them less flexible for systems with different aperture shapes. Secondly, they are subject to Runge's phenomenon, which leads to oscillations on the edges of the pupil. ENZ polynomials have been used to represent the GPF to solve the phase retrieval problem in [42], where it was shown that a few polynomials can accurately capture the wavefront while significantly speeding up the computations, especially for convex optimization-based phase retrieval methods.

Recently, the use of Gaussian radial basis functions (GRBFs) was proposed as an alternative to ENZ polynomials [45], where the GPF was approximated by a linear combination of real-valued GBBFs:

$$X(\rho,\theta) = A_{\mathcal{G}}(\rho,\theta) \sum_{k=1}^{N_\gamma} \gamma_k \mathcal{G}_k(\rho,\theta), \tag{1.31}$$

where $\mathcal{G}_k(\rho,\theta)$ are the GRBFs:

$$\mathcal{G}_k(\rho,\theta) = e^{-\lambda_k(\rho^2+\varrho_k^2-2\rho\varrho_k\cos(\theta-\vartheta_k))}, \tag{1.32}$$

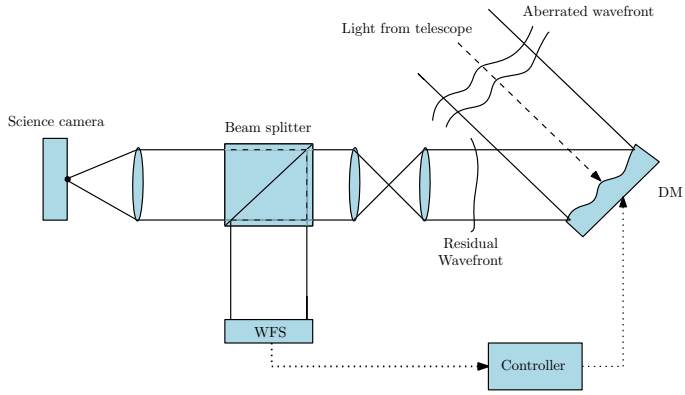

Figure 1.1: Schematic representation of a typical AO system. Adapted from Fig. 3.1

$\gamma_i \in \mathbb{C}$ are complex-valued coefficients and (ϱ_k, ϑ_k) are the polar coordinates of the GRBFs' centers. The function $A_{\mathscr{G}}(\rho,\theta)$ is an optional pupil function, with unit values inside and zero values outside of the aperture. The parameter λ_k is often referred to as the shape parameter and defines the width of the GRBFs.

It was shown that by using GRBFs for an analytic evaluation of the diffraction integral, an improvement in terms of accuracy and execution time was achieved [45]. The freedom to choose the locations and width of each GRBF separately results in a flexible basis that is easy to adapt. For example, it can be fitted to non-circular apertures or the number of GRBFs can be increased and decreased locally to create a multi-resolution scheme when desired. This increased flexibility can be further extended by considering multiple layers of GRBFs with different centers and widths per layer to improve the accuracy. An important drawback of the GRBF method is, however, that the functions are not orthogonal, which can lead to ill-conditioned optimization problems when solving the phase retrieval problem. Methods have been proposed to improve the conditioning in which a new set of basis functions is formulated that spans the same basis as the original set of basis functions, see e.g. [46]. A method that solves the phase retrieval problem using a decomposition in terms of GRBFs is presented in Chapter 2.

1.3. ADAPTIVE OPTICS

This section will address the basic idea of a classic single conjugate adaptive optics (AO) system. For a more detailed theory on adaptive optics, the reader is referred to one of the many textbooks [4, 12, 13]. A schematic representation of an AO system is shown in Figure 1.1.

1.3.1. THE MAIN IDEA OF ADAPTIVE OPTICS

As discussed in Section 1.1.1, wavefront aberrations result into a deterioration of the image quality in optical systems. In astronomy, these wavefront aberrations are caused by turbulence in the Earth's atmosphere. Adaptive optics systems aim at compensating for this deteriorating effect by using a wavefront modulating device, such as a *deformable*

mirror (DM). Usually, a *wavefront sensor* (WFS) is used to obtain an estimate of the aberrated wavefront, which is then processed by a controller to compute the shape of the DM. This subsection will introduce the main components in a classical AO system and shortly addresses adaptive optics from the perspective of control theory. More advanced control methods for AO systems will be discussed in Sections 1.4 and 1.5.

THE DEFORMABLE MIRROR

To compensate for the wavefront aberrations, one or multiple actuators, typically deformable mirrors, are included within the AO system. Deformable mirrors are, as their name suggests, able to change the shape of their reflective surface. In this way, they are able to modulate the wavefront observed by the camera.

In practice, systems often contain multiple deformable mirrors, each of them having a specific function. Recall from Section 1.2.4 that Kolmogorov's model of atmospheric turbulence states that modes with low spatial frequencies, e.g. low-order Zernike polynomials such as tip, tilt and defocus, are most prevalent in the wavefront. Therefore, it is common that there is a separate mirror to correct for the tip and tilt modes in the wavefront. Furthermore, a so-called *woofer-tweeter* setup is frequently used, where the woofer aims to compensate for the low-frequency but large-amplitude modes, and the tweeter is included to compensate for the modes with high spatial frequencies but small amplitudes.

In this thesis, the temporal dynamics of a deformable mirror will be ignored. This is based on the assumption that one sampling time of the AO loop is much longer than the time it takes for the transient response of the DM to fade out. Moreover, DMs typically have their first resonant frequency much larger than the sampling frequencies of the sensor. The temporal dynamics of the DM are often approximated by a one step time delay.

The phase modulating effect of the DM can be represented on a discrete $\bar{n} \times \bar{n}$ sampling grid, which will be denoted by $\Phi_{DM}(k), \in \mathbb{R}^{\bar{n}\times\bar{n}}$. It is commonly modelled via a linear combination of the effect that each actuator has on the wavefront, their so-called *influence functions* $H_i \in \mathbb{R}^{\bar{n}\times\bar{n}}$, $i = 1, \ldots, m$. This, combined with the one step delay, implies the following model of the DM:

$$\Phi_{DM}(k) = \sum_{i=1}^{m} H_i u_i(k-1). \tag{1.33}$$

By vectorizing the wavefront into a vector $\boldsymbol{\phi}_{DM}(k) \in \mathbb{R}^n$, this becomes

$$\boldsymbol{\phi}_{DM}(k) = H\boldsymbol{u}(k-1), \tag{1.34}$$

such that $\boldsymbol{u}(k) \in \mathbb{R}^m$ contains all the input signals u_i to the DM and $H \in \mathbb{R}^{n\times m}$ is known as the mirror's *influence matrix*. The space spanned by the columns of this influence matrix defines the shapes the mirror is able to take with respect to the sampling grid. Since any mirror with a finite amount of actuators cannot take any arbitrary shape, a so-called *fitting error* is introduced, which is defined as the difference between the desired induced phase by the DM and the true applied correction. The fitting error has been

found to scale as follows [4]:

$$\sigma_{fit}^2 = c_f \left(\frac{d_a}{r_0} \right)^{5/3} \tag{1.35}$$

where d_a is the distance between actuators projected on the aperture and c_f is a constant depending on the type of deformable mirror. For membrane mirrors, $c_f = 0.28$.

FOCAL-PLANE CAMERA

The *focal-plane camera*, sometimes referred to as the science camera, is usually only used to obtain an image of the object of interest. Improving the sharpness of this image is eventually the main goal of the AO system. However, the image captured by the focal-plane camera does contain information on the wavefront aberrations. The process of using a camera located in a focal plane of the telescope to reconstruct the wavefront is often referred to as *focal-plane sensing*. When the observed object is a point source, focal-plane sensing requires solving the phase retrieval problem discussed in Section 1.2.

In this thesis, it is assumed that the focal-plane camera is a CCD camera that captures the aberrated PSF of (1.16). In practice the images are corrupted by measurement noise. There are multiple sources of measurement noise in CCD cameras, including the *shot noise*, which has a Poissonian distribution, and *read-out noise*, which is usually assumed to be zero-mean white Gaussian noise. Considering a single pixel value of a captured image, denoted by y, the combined influence of these noise sources can be modelled as follows:

$$y = y_{true} + v_{shot} + v_{read}, \tag{1.36}$$

where y_{true} is the number of photons in a hypothetical noiseless case. The read-out noise modelled as a zero-mean white Gaussian noise $v_{read} \sim \mathcal{N}(0, \sigma_r^2)$, whereas the contribution of the shot noise is represented by v_{shot}, such that $(y_{true} + v_{shot}) \sim Pois(y_{true})$. When this reasoning is extended to the vectorized camera measurement containing all pixels, the focal-plane camera measurement can be modelled as

$$\boldsymbol{y}(k) = |\mathscr{F}_{vec}(\boldsymbol{x})|^2 + \boldsymbol{v}_y(k), \tag{1.37}$$

where the vector $\boldsymbol{v}_y$ is the combined influence of both the shot noise and read-out noise.

Since the Poisson distribution is known to converge to a Gaussian distribution when the number of arriving photons is large, i.e.,

$$\lim_{y_{true} \to \infty} Pois(y_{true}) = \mathcal{N}(y_{true}, y_{true}), \tag{1.38}$$

the following Gaussian approximation is implied:

$$Pois(y_{true}) \approx \mathcal{N}(y_{true}, y_{true}). \tag{1.39}$$

Using this as an approximation, the total measurement noise $v = v_{shot} + v_{read}$ can be modelled as follows when y_{true} is large:

$$v_y \sim \mathcal{N}(0, y_{true} + \sigma_r^2). \tag{1.40}$$

THE WAVEFRONT SENSOR

Since retrieving the wavefront estimation from focal-plane images alone is complicated and computationally demanding, dedicated pupil-plane wavefront sensors are a crucial element in AO systems when a fast reconstruction of the wavefront is desired. An important difference between the pupil-plane wavefront sensor and the focal-plane camera is, as the name suggest, the placement of the sensor. Pupil-plane sensors are placed in a plane that is conjugated to the pupil plane of the telescope. Although there exist a number of different pupil-plane wavefront sensors, the most commonly used sensor in astronomy is the *Shack-Hartmann (SH) sensor*.

The SH sensor consists of a grid of small lenses (referred to as lenslets), each of which focuses a local part of the aperture (referred to as a subaperture) onto a photon sensor. When considering a single guide star, the image obtained by the SH sensor is an array of focused images of guide stars. These focused images are usually referred to as (focal) spots. When the wavefront is perfectly flat within each subaperture, the spots are visible as a set of Airy patterns located on a regular grid, and the center of each spot is in the center of their corresponding subaperture. When the wavefront within each subaperture is not flat, the spots will get distorted as well. In particular, the average tilt within each subaperture moves the center of the spot away from the center of the subaperture. Therefore, the distance between the spot location and the center of the subaperture defines the local tilt in this particular subaperture. By measuring these distances for all subapertures, an estimate of the spatial gradient of the wavefront can be computed.

One main advantage of the SH sensor with respect to focal-plane sensing is that it provides a measurement that is linearly related to the wavefront aberrations. This significantly simplifies the wavefront reconstruction problem. Considering a discretized wavefront $\boldsymbol{\phi} \in \mathbb{R}^n$ and its corresponding discretized grid of local gradients $\boldsymbol{s} \in \mathbb{R}^q$, the following linear relation can be defined:

$$\boldsymbol{s} = G\boldsymbol{\phi}, \tag{1.41}$$

where $G \in \mathbb{R}^{q \times n}$ is known as the *geometry matrix*. Due to camera noise, the discretization into pixels and the discretization of the pixel values, the measurement values are corrupted by noise. Usually, the measurement noise is approximated by a zero-mean white Gaussian noise. That is, the WFS measurements are modelled by

$$\boldsymbol{s}(k) = G\boldsymbol{\phi}(k) + \boldsymbol{v}_s(k), \tag{1.42}$$

with $\boldsymbol{v}_s(k) \sim \mathcal{N}(0, R_s)$, $R_s = r_s I$.

Since the WFS signal only contains information about the average gradient of the wavefront within each subaperture, i.e. the local tip-tilt modes, all higher order aberrations per suberapertures are not measured. According to the Nyquist-Shannon sampling theorem, the maximum spatial frequency of the wavefront captured by the WFS is $1/(2d_s)$, d_s being the diameter of each subaperture. Furthermore, because of the geometry of the WFS lenslets, there are two modes in the wavefront for which the sensor is blind, known as the *piston* and *waffle* mode. This is reflected by the fact that the matrix G is rank-deficient and the unobservable modes span the nullspace of the matrix G. The piston mode is just the average value of the phase aberration and does not affect

the image quality, such that it is often neglected. The waffle mode is a very high spatial frequency mode, so Kolmogorov's model of turbulence suggests that its influence on the wavefront aberrations is limited.

1.3.2. CLOSING THE LOOP

The last remaining component of the AO system in the scheme of Figure 1.1 is the *controller*. The controller computes the signal to the DM, $\boldsymbol{u}(k)$, based on the sensor measurements and aims to flatten the *residual wavefront*. Assuming a turbulent wavefront denoted by $\boldsymbol{\phi}(k)$ and wavefront induced by the DM $\boldsymbol{\phi}_{DM}(k)$ as in (1.34), the residual wavefront is defined as

$$\boldsymbol{\epsilon}(k) = \boldsymbol{\phi}(k) - \boldsymbol{\phi}_{DM}(k) = \boldsymbol{\phi}(k) - H\boldsymbol{u}(k-1), \tag{1.43}$$

such that the SH sensor measurement of (1.42) becomes

$$\boldsymbol{s}(k) = G\boldsymbol{\epsilon}(k) + \boldsymbol{v}_s(k). \tag{1.44}$$

Usually, the controller uses the signal from the WFS. However, there are AO control systems that do not use a dedicated WFS, but instead the image from the focal-plane camera directly. These systems are known as *wavefront sensorless* (WFSless) adaptive optics systems. This subsection will be limited to the classical control methods, which do use a dedicated WFS. WFSless control will be discussed in Section 1.3.3.

In general, the computation of the "optimal" control signal $\boldsymbol{u}(k)$ can be split into two separate steps. The first step is a *wavefront reconstruction* step, which can be defined as finding an estimate of the wavefront given the sensor measurement $\boldsymbol{s}(k)$. The second step is a projection of the estimated wavefront onto the actuator space of the DM.

Early methods have treated the wavefront reconstruction problem as a deterministic least-squares problem [47–49]. In a deterministic setting, the wavefront estimate becomes the solution to a linear least squares problem of the form:

$$\hat{\boldsymbol{\epsilon}}(k) = \arg\min_{\boldsymbol{\epsilon}(k)} \|\boldsymbol{s}(k) - G\boldsymbol{\epsilon}(k)\|_2^2 = G^\dagger \boldsymbol{s}(k), \tag{1.45}$$

where $\hat{\boldsymbol{\epsilon}}(k)$ represents the reconstructed wavefront and $G^\dagger$ represents the *pseudo-inverse* of the matrix G. Due to the low-rank property of the matrix G, $G^\dagger$ is usually computed using the truncated SVD, see [50] for details.

The drawback of treating wavefront reconstruction as a deterministic least squares problem is that its solution is usually very sensitive to measurement noise. Therefore, methods have been proposed that take the stochastic nature of the problem into account [51–53]. Treating wavefront reconstruction as a *stochastic least squares* problem requires a priori knowledge of the distribution of the wavefront. In Section 1.1.2, it was discussed that the spatial covariance of the wavefront is assumed to be zero-mean white noise:

$$\boldsymbol{\phi} \sim \mathcal{N}(0, C_\phi), \quad \text{where } C_\phi = E\left[\boldsymbol{\phi}(k)\boldsymbol{\phi}^T(k)\right] \in \mathbb{R}^{n\times n}, \tag{1.46}$$

where the entries of the covariance matrix C_ϕ can be computed via (1.12). In the closed-loop case, however, the WFS measures the residual wavefront $\boldsymbol{\epsilon}(k)$ rather than $\boldsymbol{\phi}(k)$. Therefore, the assumption is made that $E[\boldsymbol{\epsilon}(k)\boldsymbol{\epsilon}^T(k)] = C_\phi$. With this assumption, the

stochastic least squares problem can be formulated as a regularized weighted least-squares problem:

$$\begin{aligned}\hat{\boldsymbol{\epsilon}}(k) &= \underset{\boldsymbol{\epsilon}(k)}{\arg\min} \ \|\boldsymbol{s}(k) - G\boldsymbol{\epsilon}(k)\|^2_{R_s^{-1}} + \|\boldsymbol{\epsilon}(k)\|^2_{C_\phi^{-1}} \\ &= \left(G^T R_s^{-1} G + C_\phi^{-1}\right)^{-1} G^T R_s^{-1} \boldsymbol{s}(k). \end{aligned} \tag{1.47}$$

The stochastic least-squares problem is much more robust against measurement noise, and therefore preferred when (an estimate of) the matrices C_ϕ and R_s are available.

The second step of the control problem is the projection of the reconstructed wavefront $\hat{\boldsymbol{\epsilon}}(k)$ onto the actuator space of the DM. Using the linear model of the DM given in (1.34) and since $\hat{\boldsymbol{\phi}}(k) = \hat{\boldsymbol{\epsilon}}(k) + H\boldsymbol{u}(k-1)$, this boils down to solving a simple deterministic least squares problem which has the following closed-form solution:

$$\boldsymbol{u}(k) = H^\dagger \hat{\boldsymbol{\phi}}(k+1) = H^\dagger \hat{\boldsymbol{\epsilon}}(k+1) + \boldsymbol{u}(k-1). \tag{1.48}$$

The problem with this method is that, as shown in the above equation, it requires knowledge of $\hat{\boldsymbol{\epsilon}}(k+1)$ at time instance k. Typically, this is where the classical controller makes the assumption that, when the sampling frequency is large enough, $\hat{\boldsymbol{\phi}}(k+1) = \hat{\boldsymbol{\phi}}(k)$. Under this assumption, the overall controller becomes

$$\boldsymbol{u}(k) = \underbrace{H^\dagger \left(G^T R_s^{-1} G + C_\phi^{-1}\right)^{-1} G^T R_s^{-1}}_{M} \boldsymbol{s}(k) + \boldsymbol{u}(k-1), \tag{1.49}$$

where the matrix M is often referred to as the controller gain matrix. Of course, this controller is but an example, and there are many other methods possible to compute a gain matrix M.

Although the gain matrix derived above is optimal in theory, practical issues, such as model inaccuracies or limitations of the range in which the DM can be controlled, mean that adaptations of this control method can lead to a better performance. Therefore, it is common to use a proportional-integrator (PI) controller based on this gain matrix [53]:

$$\boldsymbol{u}(k) = c_1 M \boldsymbol{s}(k) + c_2 \boldsymbol{u}(k-1) \tag{1.50}$$

where c_1, c_2 are two tuning parameters.

It will be discussed in Section 1.3.4 that the assumption $\hat{\boldsymbol{\phi}}(k+1) = \hat{\boldsymbol{\phi}}(k)$ is the source of the so-called *temporal error*. Therefore, including a better *one-step-ahead prediction* of $\hat{\boldsymbol{\phi}}(k+1)$ based on $\hat{\boldsymbol{\phi}}(k)$ can significantly improve the controller performance, which will be the topic of Section 1.4.

1.3.3. FOCAL-PLANE SENSING AND WAVEFRONT SENSORLESS AO

Although AO systems typically have a dedicated WFS, there is a second class of control methods for AO often called *wavefront sensorless (WFSless)* AO methods. One class of WFSless AO methods typically uses optimization methods to maximize a certain performance metric by iteratively updating the DM. Various of such WFSless AO algorithms have been developed using different optimization techniques [54–58]. These methods

typically require many iterations in which a new image is obtained in order to converge. Therefore, a recent development in WFSless AO is a class of methods, often referred to as *model-based* WFSless AO, in which a model of the metric is used to speed up the correction [59], see [59–66] and the references therein for examples of such algorithms. Model-based WFSless AO methods are, due to their faster convergence, promising for real-time AO applications in which the aberration is time-varying.

It was previously mentioned that, when a dedicated WFS was included in the AO system, the control problem can be seen as two separate steps. First, the wavefront is reconstructed from the sensor signal and second, this wavefront is projected onto the actuator space. This two-step approach can also be extended to the WFSless case. The second step remains the same as in the WFS-based control case, but the wavefront reconstruction step becomes significantly more complicated as it involves solving the phase retrieval problem. Section 1.2 discussed that from a single PSF image only, it is often impossible to retrieve the wavefront without certain prior knowledge.

Advantages of focal-plane sensing methods are that they require no, or little, extra optical components, making the system simple and inexpensive. Moreover, the absence of a beam splitter avoids non-common path aberrations (NCPAs), which occur when using a pupil-plane WFS due to different optical paths to the WFS and focal-plane camera. The main drawback of using focal-plane sensors, however, is the non-linear relation between the image in the focal plane and the wavefront, which creates a challenge for AO systems with respect to finding an accurate reconstruction in real time [18]. The non-linear relation between the wavefront and the image causes an increased computational burden. Approximations of the non-linear relation using a first- or second-order Taylor expansion can be used to speed up the reconstruction. It was shown that when the phase is small, a first-order approximation of the relation can be used to obtain a closed-form solution to the phase retrieval problem [67].

A number of iterative methods have been proposed that use a first- or second-order Taylor approximation to represent the non-linear relation between the wavefront and PSF [68–70]. By adopting an iterative framework in which the Taylor expansion is redefined at each iteration around the current estimate, the limited range of the small-phase approximation can be extended. Moreover, when considering a closed-loop situation with a high sample frequency such that $\boldsymbol{\phi}(k+1) \approx \boldsymbol{\phi}(k)$, and with a controller that is able to fully regulate the residual wavefront, i.e. H in (1.34) is full-rank, the control signal can be chosen such that $\hat{\boldsymbol{\epsilon}}(k+1) = \hat{\boldsymbol{\epsilon}}(k) = 0$. This realization implies that in such scenarios, the Taylor approximation only has to be computed around zero phase, which can be done offline and can be used to speed up the wavefront reconstruction significantly. Another advantage of such an iterative approach is that the phase diversity images can also be collected sequentially [71]. Since the deformable mirror applies a different correction at each iteration, the correction change can be seen as a source of phase diversity between two consecutive measurements.

The combination of the larger computational burden compared to pupil-plane sensing algorithms and the use of the assumption $\boldsymbol{\phi}(k+1) \approx \boldsymbol{\phi}(k)$, implies that focal-plane sensors are mainly suited for the estimation of quasi-static aberrations and calibration procedures. Therefore, the need for an accurate one-step-ahead predictor is even greater for these algorithms than for WFS-based control when aiming to reconstruct and control

faster evolving aberrations.

1.3.4. TEMPORAL DYNAMICS IN ATMOSPHERIC TURBULENCE

The temporal dynamics of aberrations caused by atmospheric turbulence was briefly discussed in Section 1.1.2. It was mentioned how by using *Taylor's frozen flow hypothesis*, the turbulence can be modelled as finite set of layers, each of them moving in a constant direction with a constant speed. This subsection will discuss the effect of aberration dynamics on the performance of an AO system.

Taylor's frozen flow hypothesis can be used to relate the spatial and temporal statistics, sometimes referred to as *spatio-temporal correlations*. Defining the wavefront of a single turbulence layer at time instance t as $\phi(\boldsymbol{\zeta}, t)$, where $\boldsymbol{\zeta} \in \mathbb{R}^2$ denotes the spatial coordinates, this relation is as follows:

$$\phi(\boldsymbol{\zeta}, t + \Delta t) = \phi(\boldsymbol{\zeta} - \boldsymbol{v}\Delta t, t), \tag{1.51}$$

where $\boldsymbol{v} \in \mathbb{R}^2$ is represents the direction and speed of translation of the phase screen. The importance of this equation is that it can be used to transform the temporal change into a spatial distance, opening up the possibility to apply Kolmogorov's theory not only to represent the spatial, but also the temporal statistics.

It was previously mentioned that there is an inevitable delay between the WFS capturing an image and the DM actually applying its correction. This was modelled by assuming a delay in the DM model (1.34). During this time delay, the wavefront aberrations will have evolved. The error caused by this time delay is called the *temporal error* and can be computed via

$$\sigma^2_{temp} = c_t \left(\frac{f_G}{f_s}\right)^{5/3}, \tag{1.52}$$

where f_G is known as the *Greenwood frequency*: $f_G = 0.427\bar{v}/r_0$ [72, 73], c_t is a scaling factor which depends on the type of controller, and f_s is the control loop's sampling frequency.

Since the temporal error increases proportional to $\left(f_G/f_s\right)^{5/3}$, the Greenwood frequency, or its related *Greenwood time delay*: $\tau_0 = 0.314 r_0/\bar{v}$, is often used as a measure to determine the distorting effect of the dynamics on the image quality. For large Greenwood frequencies, i.e. large $\bar{v}$ or small r_0, the temporal error can become the limiting factor of the control system. This leaves two options to improve the performance of the AO system. The first being to increase the sampling frequency f_s, which is limited by the hardware (cameras, DM) and the computation of the control action. The second option, which is a central part of this thesis, is to predict the wavefront aberration.

1.4. PREDICTION FOR ADAPTIVE OPTICS SYSTEMS

In order to decrease the temporal error, it is necessary to predict the wavefront aberrations. This section will discuss prediction methods for adaptive optics system and modelling the turbulence dynamics and the measurement noise.

1

1.4.1. MODELLING THE WAVEFRONT DYNAMICS

When modelling the dynamic wavefront aberrations caused by atmospheric turbulence, *vector auto-regressive* (VAR) models are a popular choice to capture the dynamic evolution. These VAR models are of the form:

$$\boldsymbol{\phi}(k+1) = \sum_{i=0}^{r-1} A_i \boldsymbol{\phi}(k-i) + \boldsymbol{w}(k), \tag{1.53}$$

where the matrices $A_i \in \mathbb{R}^{n \times n}$ are the VAR coefficients and $\boldsymbol{w}(k) \sim \mathcal{N}(0, Q)$ is a Gaussian zero-mean white noise signal with covariance matrix Q. When considering a single turbulence layer, a VAR model of order $r = 1$ is often sufficient to accurately capture the model dynamics. For multiple layers, higher order models can improve the accuracy. This thesis, however, mainly focuses on VAR models of order $r = 1$, as they often result in a prediction that is accurate enough, while having a limited number of parameters, making them suitable for large-scale AO applications. This computational advantage is further explained in Section 1.5.

A more general representation of the turbulence dynamics would be to model it by a *state-space* model:

$$\boldsymbol{x}(k+1) = A_x \boldsymbol{x}(k) + \boldsymbol{w}_x(k), \tag{1.54}$$

$$\boldsymbol{\phi}(k) = C_x \boldsymbol{x}(k) + \boldsymbol{v}_x(k), \tag{1.55}$$

where $\boldsymbol{x}(k) \in \mathbb{R}^{n_x}$ is known as the *state* and $\boldsymbol{w}_x(k)$ and $\boldsymbol{v}_x(k)$ are zero-mean Gaussian white noise signals with covariance matrices Q_x and R_x respectively. Although this model is more general and, therefore, theoretically more precise in capturing the turbulence dynamics, it also has its drawbacks. The main drawback is that the state $\boldsymbol{x}(k)$ does not necessarily represent a physical quantity, making it difficult to interpret in practice. This leads to problems in large-scale applications, when one would like to formulate computationally efficient structured models.

There are many available methods for deriving a turbulence dynamics model. In general, these methods can be split in two categories: *data-driven* methods and methods using *first-principles*. Methods that obtain the model from first principles often assume a simple model structure, such as a first order VAR (VAR-1) model, i.e., taking $r = 1$ in (1.53):

$$\boldsymbol{\phi}(k+1) = A\boldsymbol{\phi}(k) + \boldsymbol{w}(k), \tag{1.56}$$

where the matrices A and Q are unknown and have to be determined. These methods require prior knowledge of certain characteristics of the turbulence, including the wavefront's covariance matrix C_ϕ and average wind speed $\bar{v}$. Combined with the spatio-temporal correlations of (1.51), given by the frozen-flow hypothesis, having such prior knowledge allows for the computation of the covariance of the current and delayed wavefront: $C_{\phi,1} = E[\boldsymbol{\phi}(k)\boldsymbol{\phi}^T(k-1)]$. Using this knowledge, the matrix A can be derived via

$$A = C_{\phi,1} C_\phi^{-1}. \tag{1.57}$$

With A known, the relation in (1.56) can be used to compute Q as

$$Q = C_\phi - A C_\phi A^T. \tag{1.58}$$

When there is no accurate prior information available, the model can be computed from data. Continuing the example of a VAR model of order 1, a possible data-driven approach to identify the matrices A and Q will be presented next.

The first step of such a data-driven approach is to obtain a time-series of open-loop sensor data: $\{\hat{\boldsymbol{s}}(k), k = 1,2,\ldots,K\}$, which can be transformed in wavefront data: $\{\hat{\boldsymbol{\phi}}(k), k = 1,2,\ldots,K\}$, for example using one of the wavefront reconstruction techniques discussed in Section 1.3.2. Next, sample covariance approximations of the matrices C_ϕ and $C_{\phi,1}$ can be determined:

$$C_\phi = \frac{1}{K}\sum_{i=1}^{K} \boldsymbol{\phi}(i)\boldsymbol{\phi}^T(i), \quad C_{\phi,1} = \frac{1}{K-1}\sum_{i=1}^{K-1} \boldsymbol{\phi}(i+1)\boldsymbol{\phi}^T(i), \tag{1.59}$$

after which A and Q can be computed via (1.57) and (1.58). Of course, this example is a very simple and straightforward approach to data-driven system identification. Different approaches and methods to fit VAR or state-space models to data are discussed in textbooks such as [50, 74]. Using the VAR-1 model to represent the turbulence, the following vector auto-regressive model with exogenous inputs (VARX) represents the residual wavefront in closed-loop:

$$\boldsymbol{\epsilon}(k+1) = \boldsymbol{\epsilon}(k) - H\boldsymbol{u}(k) + AH\boldsymbol{u}(k-1) + \boldsymbol{w}(k). \tag{1.60}$$

A number of AO specific data-driven methods have been presented in the literature that use a dynamic model to predict the wavefront aberrations, e.g. [75, 76]. However, many system identification methods are mainly suitable for small- to medium-scale AO systems. Large-scale AO systems typically assume a dimensionality $n > 10^4$, which creates problems regarding the large number of unknowns to be estimated, e.g. a full matrix A has 10^8 unknowns. Therefore, without special techniques to reduce the number of model parameters, these methods would require an immense amount of data and available storage, which is not realistic. Typically, the system matrices are modelled using structured representations, as will be discussed in Section 1.5.

1.4.2. OPTIMAL PREDICTION FROM WFS MEASUREMENTS

Combining the SH sensor model of (1.42) and the model of (1.60) to represent the residual wavefront, the following linear state-space system can be derived for an AO system:

$$\boldsymbol{\epsilon}(k+1) = A\boldsymbol{\epsilon}(k) - H\boldsymbol{u}(k) + AH\boldsymbol{u}(k-1) + \boldsymbol{w}(k) \tag{1.61}$$

$$\boldsymbol{s}(k) = G\boldsymbol{\epsilon}(k) + \boldsymbol{v}_s(k), \tag{1.62}$$

where $\boldsymbol{w}(k) \sim \mathcal{N}(0,Q)$ and $\boldsymbol{v}_s(k) \sim \mathcal{N}(0,R_s)$ are known as the process noise and measurement noise respectively. The Gaussian distribution of the noise signals allows for the use of a *Kalman filter* to filter and predict the residual wavefront $\boldsymbol{\epsilon}(k)$.

Kalman filters are widely used as state observers and have been studied extensively since their first presentation by Kalman [77]. Nowadays, they are standard tools for filtering and prediction of linear state-space systems and can be found in many textbooks, e.g. [50]. At each time step k, the Kalman filter performs two steps. First, the *measurement update* is performed, which optimally combines a new measurement with a previous state estimate $\hat{\boldsymbol{\epsilon}}(k|k-1)$ into a new state estimate, $\hat{\boldsymbol{\epsilon}}(k|k)$. The second step, the *time update*, uses this new state estimate and computes a prediction of the state, $\hat{\boldsymbol{\epsilon}}(k+1|k)$.

Measures of the accuracy of the estimates $\hat{\boldsymbol{\epsilon}}(k|k)$ and $\hat{\boldsymbol{\epsilon}}(k+1|k)$ are expressed by the *state error-covariance matrices* $P(k|k)$ and $P(k+1|k)$ respectively, defined as

$$P(k|k) = E\left[(\boldsymbol{\epsilon}(k) - \hat{\boldsymbol{\epsilon}}(k|k))(\boldsymbol{\epsilon}(k) - \hat{\boldsymbol{\epsilon}}(k|k))^T\right], \tag{1.63}$$

$$P(k+1|k) = E\left[(\boldsymbol{\epsilon}(k+1) - \hat{\boldsymbol{\epsilon}}(k+1|k))(\boldsymbol{\epsilon}(k+1) - \hat{\boldsymbol{\epsilon}}(k+1|k))^T\right]. \tag{1.64}$$

The Kalman filter computes the time and measurement update such that their corresponding error covariance matrices are minimal. For a proof of the minimal variance property of Kalman filters, the reader is referred to [50].

The measurement update can be formulated as the solution to a stochastic least-squares problem:

$$\hat{\boldsymbol{\epsilon}}(k|k) = \arg\min_{\boldsymbol{\epsilon}(k)} \|\hat{\boldsymbol{\epsilon}}(k|k-1) - \boldsymbol{\epsilon}(k)\|^2_{P^{-1}(k|k-1)} + \|\boldsymbol{s}(k) - G\boldsymbol{\epsilon}(k)\|^2_{R_s^{-1}}, \tag{1.65}$$

$$= \hat{\boldsymbol{\epsilon}}(k|k-1) + K'(k)\left(\boldsymbol{s}(k) - G\hat{\boldsymbol{\epsilon}}(k|k-1)\right), \tag{1.66}$$

where

$$K'(k) = P(k|k-1)G^T\left(R_s + GP(k|k-1)G^T\right)^{-1}. \tag{1.67}$$

This optimization problem clearly has similarities with the wavefront reconstruction problem in (1.47). The most notable differences being that, instead of a certain assumed prior knowledge on the distribution of the random variable $\boldsymbol{\epsilon}(k)$, it uses the statistical information from the time update of the previous time step, $\boldsymbol{\epsilon}(k) \sim \mathcal{N}(\hat{\boldsymbol{\epsilon}}(k|k-1), P(k|k-1))$. The time update follows from propagating the measurement update estimate one time-step ahead using the state update equation of (1.61):

$$\hat{\boldsymbol{\epsilon}}(k+1|k) = A\hat{\boldsymbol{\epsilon}}(k|k) - H\boldsymbol{u}(k) + AH\boldsymbol{u}(k-1) \tag{1.68}$$

$$= (A - K(k)G)\,\hat{\boldsymbol{\epsilon}}(k|k-1) + K(k)\boldsymbol{s}(k) - H\boldsymbol{u}(k) + AH\boldsymbol{u}(k-1), \tag{1.69}$$

where $K(k) = AK'(k)$ is usually referred to as the *Kalman gain*. The input signals to control the shape of the DM, $\boldsymbol{u}(k)$ and $\boldsymbol{u}(k-1)$, can be chosen freely and depend on the control algorithm.

In order to perform the measurement update, the error-covariance matrices have to be updated. Given the previous time update, $P(k|k-1)$, the next combined time and measurement update is given by the *Riccati difference equation*. Using the assumption that $E[\boldsymbol{w}(k)\boldsymbol{v}_s(k)^T] = 0$, this update becomes:

$$\begin{aligned} P(k+1|k) =& AP(k|k-1)A^T + Q \ldots \\ &- AP(k|k-1)G^T\left(R_s + GP(k|k-1)G^T\right)^{-1} GP^T(k|k-1)A^T. \end{aligned} \tag{1.70}$$

When the state-space model is time-invariant, as is the case for the model given by (1.61 - 1.62), the recursions for $P(k|k-1)$ and $K(k)$ converge to constant matrices. These constant matrices are computed by solving the *discrete algebraic Riccati equation* (DARE):

$$P = APA^T + Q - APG^T\left(R_s + GPG^T\right)^{-1} GP^T A^T, \tag{1.71}$$

such that the Kalman gain K becomes

$$K = APG^T \left(R_s + GPG^T\right)^{-1}. \tag{1.72}$$

The optimal one-step-ahead prediction, $\hat{\boldsymbol{\epsilon}}(k+1|k)$, can be mapped onto the actuator space in order to compute the control action. Optimal controllers of this form, such as the linear quadratic regulator, have been previously presented for AO systems and can significantly improve the performance over classical methods, see [78–81] amongst others. Besides the VAR-1 model representation of the spatio-temporal correlations of the wavefront, the general state-space formulation can also be used to optimally predict the wavefront. This has been done in [76], which proposes an $\mathscr{H}_2$-optimal controller where the turbulence dynamics were identified from data using a subspace algorithm.

1.4.3. PREDICTION AND FOCAL-PLANE SENSING

When a focal-plane sensor is considered instead of a pupil-plane wavefront sensor, the state-space system describing the measurements in a dynamic situation becomes:

$$\boldsymbol{\epsilon}(k+1) = A\boldsymbol{\epsilon}(k) - H\boldsymbol{u}(k) + AH\boldsymbol{u}(k-1) + \boldsymbol{w}(k) \tag{1.73}$$

$$\boldsymbol{y}(k) = \left|\mathscr{F}\left(\boldsymbol{a} \odot \exp(j\boldsymbol{\epsilon}(k))\right)\right|^2 + \boldsymbol{v}_{\boldsymbol{y}}(k), \tag{1.74}$$

using the Gaussian noise approximation of (1.40), such that $\boldsymbol{v}_y(k) \sim \mathcal{N}(0, R_y(k))$. Two important differences with the state-space model in (1.61 - 1.62) are visible. First, the output equation (1.62) is non-linear. Second, the measurement noise covariance matrix is time-varying. Moreover, it should be noted that the measurement noise is a combination of Poissonian and Gaussian noise as explained in Section 1.3.1 and that modelling it by a Gaussian noise is merely an approximation.

The Kalman filter theory as described in the previous subsection cannot be applied to this non-linear model directly. However, a vast body of literature has formed over the past decades presenting methods that propose different approaches and approximations to overcome problems caused by the non-linearity, see [82–93]. Some notable non-linear filters include the extended Kalman filter (EKF) [82], iterated extended Kalman filter (IKF) [90], unscented Kalman filter (UKF) [83], ensemble Kalman filter (EnKF) [93], cubature filter [87] and the particle filter [92]. Extending the theory of the previous subsection therefore implies the use of any of these non-linear filters. Although in principle any of these methods is a valid candidate to be used for dynamic focal-plane wavefront sensing, this thesis will only consider the EKF and IKF.

The theory of the focal-plane wavefront sensing method in [68] has been extended to a dynamic framework by using the EKF [94–96]. The results of these methods show that for small aberrations, this application of the EKF is able to accurately track the wavefront dynamics. One major drawback of this approach is the large computational burden, making these methods only suitable for small-scale AO systems dealing with slow-moving aberrations or for post-processing purposes. Moreover, these methods were shown to work when considering two images with phase diversity, which can lead to problems regarding non-common path aberrations. In the field of WFSless AO, most methods still neglect the aberration dynamics. A fast implementation of a second moment-based WFSless AO method was proposed in [97], which aimed to improve the performance of this class of model-based WFSless AO algorithms for time-varying aberrations.

However, this method still does not predict the evolution of the aberration over time, thereby still assuming that the wavefront remains approximately unchanged between taking two consecutive images.

Currently, no alternatives have been proposed that present a rigorous approach to obtain, in a computationally efficient manner, an accurate prediction of the wavefront based on PSF images only. This missing area in literature has been one of the main motivations for this thesis. Chapters 3 and 4 propose methods that present methods that use Kalman filter theory in a computationally efficient framework.

1.5. STRUCTURED MODELLING FOR LARGE-SCALE ADAPTIVE OPTICS SYSTEMS

A problem with many predictive methods for AO systems is that they are very computationally demanding, which makes them challenging to use in an AO system running at a sampling frequency of typically 100-2000 Hz. This section will discuss the bottlenecks in the existing methods and will also discuss a number of algorithms that have been proposed to lift (part of) this computational burden. In particular, it will focus on a number computationally efficient structured models that have been shown to accurately model the complete AO system.

The computational bottlenecks when considering large-scale AO systems can be split in two categories: *online* and *offline*. *Offline* computations represent the computations that are not constrained by the sampling frequency of the control loop, whereas *online* computations have to be performed within one sampling time. For classical Kalman filter-based predictive algorithms, the offline bottleneck is the computation of the Kalman gain K by solving the DARE, which has a computational complexity that scales with $\mathcal{O}(n^3)$. The online computations of the one-step-ahead prediction involve dense matrix-vector multiplications that scale with $\mathcal{O}(n^2)$, which can be problematic for large-scale AO systems (which can reach dimensions of $n > 10^4$).

A common approach to overcome these bottlenecks is to represent the system dynamics using *structured* models. A number of important matrix structures will be shortly introduced in this section. First, the appearance of sparse system matrices is discussed. Afterwards, it is shown how the system matrices can be approximated as a sum of Kronecker products, which can also be seen as a tensor-train representation. Finally, the specific usefulness of the FFT algorithm to efficiently compute the DFT is mentioned.

1.5.1. SPARSITY STRUCTURES IN AO SYSTEMS

The appearance of sparsity structures in AO systems has been mentioned in several works in literature. For example, a common assumption for methods aiming for a scalable solution of the DARE is to take $A = aI$, with $0 < a < 1$, due to the fact that turbulence is a spatially homogeneous process [98], which is a very special case of a sparse matrix. Moreover, the fact that the inverse of the covariance matrix of the wavefront, C_ϕ^{-1}, can be represented by a sparse and *banded* matrix was previously shown [53]. Also the matrices G and H are sparse and banded due to the local nature of the measurements and assuming local actuator influence on the wavefront.

This realisation of sparsity structures in AO systems has been used in a number of

methods to efficiently solve the DARE [98–101]. Although this simple dynamic model $A = aI$ makes it possible to compute the Kalman gain in a scalable manner, it has severe shortcomings in terms of the accuracy of the predicted wavefront for larger wind speeds and lower sampling frequencies. Furthermore, these methods rely on first principles to compute the covariance matrix Q, which implies knowledge of parameters such as the wind speed and Fried parameter beforehand.

This thesis will consider more accurate dynamic models, where A is banded and sparse rather than diagonal, and where the computation of the system matrices does not rely on first principles. One systematic approach to arrive at a more general and accurate sparsity structure is to use that the wavefront is reconstructed on a two-dimensional regular grid of sampling points, and that the turbulence can be accurately modelled using Taylor's frozen flow hypothesis. Considering, for the sake of simplicity, a single turbulence layer, it becomes clear that the temporal evolution of the wavefront, seen from each sampling point, has a local nature, that is, the wavefront at time instance k is merely a slightly shifted version of $k-1$. The reason this can be seen as "local" dynamics is that, in order to predict the value of the wavefront at a single sampling point, past data of other sampling points in its neighbourhood will suffice.

This intuitive formulation of the temporal evolution of the wavefront can be formalized using *graphical modelling*. Graphical models are widely used in many different scientific fields, as they can offer a useful insight into matrix structures to describe statistical distributions and various types of dynamic models. More information on graphical models can be found in many textbooks written on this topic, such as [102]. Two mathematical concepts in graph theory that are central to showing the sparsity structures appearing in VAR(X) models are *causality* [103] and *conditional independence* [102]. Using these two notions, the sparsity of the system matrices can be determined [104]. By assuming Taylor's frozen turbulence hypothesis of (1.51) to define the causality relations, and using insights from Kolmogorov's turbulence model to define the conditional independence relations, it was shown that this theory can be extended to AO systems [105]. This work showed that the following one-step-ahead predictor could accurately predict the evolution of the SH signal:

$$\hat{\boldsymbol{s}}(k+1|k) = \sum_{i=0}^{r-1} A_i \boldsymbol{s}(k-i), \tag{1.75}$$

where all matrices A_i are sparse and banded. Moreover, the sparsity of C_ϕ^{-1}, which was previously mentioned in AO literature [53], also follows from the graphical model representation due to conditional independence relations between sampling points. An advantage of the method presented in [105] is that it is fully data-driven, such that it is not necessary to have accurate knowledge on physical quantities such as the wind speed and Fried parameter.

An important side note to the presence of sparsity in the system matrices is that it only holds if there is a certain locality between the two variables it relates. The matrix A in (1.56) is only sparse the evolution of $\boldsymbol{\phi}(k)$ happens on a local scale. Similarly, the actuator influence matrix H is only sparse if each influence function of the DM only has a local influence on the wavefront. This form of locality holds, for example, when assuming Taylor's frozen turbulence hypothesis. It was shown that the sparsity pattern of

the matrix A in (1.56) depends on the direction and absolute displacement of the phase screen per sampling time [105].

The presence of this sparsity is an important reason for choosing the VAR model to represent the aberration dynamics over the state-space model. Since the state $\boldsymbol{x}(k)$ in (1.54) generally does not represent a physical quantity with such local features, the sparsity structure will be destroyed in the matrix A_x.

1.5.2. SYSTEM MATRICES AS A SUM OF KRONECKER PRODUCT

Recently, it was presented that the two-dimensional grid on which the sensor and wavefront is represented in AO systems does not only cause the appearance of sparsity structures in AO systems, but also that many matrices could be approximated as a sum of Kronecker products of sparse (banded) matrices [106]. This realisation can be shown again by using Taylor's frozen flow hypothesis. According to this assumption, the dynamics of each phase screen can be considered to be a translation on a two-dimensional plane. By decoupling the translations in each dimensions, such a movement can be modelled as follows [106]:

$$A_{0,l}\Phi(k+1)A_{0,r} = A_{1,l}\Phi(k)A_{1,r} + W_\Phi(k), \tag{1.76}$$

where $\Phi(k) \in \mathbb{R}^{\bar{n}\times\bar{n}}$ represents the wavefront on its original two-dimensional grid. When vectorizing this formulation, the following model is obtained:

$$A_0\boldsymbol{\phi}(k+1) = A_1\boldsymbol{\phi}(k) + \boldsymbol{w}_\phi(k), \tag{1.77}$$

where $A_0 = A_{0,r}^T \otimes A_{0,l}$ and $A_1 = A_{1,r}^T \otimes A_{1,l}$.

A matrix that can be decomposed as a single Kronecker product is often referred to as having a *Kronecker rank* equal to 1. It was further shown that by increasing the Kronecker rank, the accuracy can be improved [107, 108]. In these works, a higher order VAR model was used to directly estimate a one-step-ahead prediction of the SH signal $\boldsymbol{s}(k)$:

$$\hat{\boldsymbol{s}}(k+1|k) = \sum_{i=0}^{r-1}\sum_{j=1}^{r_K}\left(A_{r,i,j}^T \otimes A_{l,i,j}\right)\boldsymbol{s}(k-i), \tag{1.78}$$

such that r represents the temporal order of the VAR model and r_K is the Kronecker rank. By keeping the wavefront in its original matrix form, this model can be seen as a *tensor* model. This simple tensor model was further extended into a higher-order tensor representation to formulate a tensor-based predictive controller for large-scale AO in [109], which used the following predictor:

$$\hat{\boldsymbol{s}}(k+1|k) = \sum_{i=0}^{t-1}\sum_{j=1}^{r_K}\left(A_{1,i,j}^T \otimes A_{2,i,j} \otimes \ldots \otimes A_{d,i,j}\right)\boldsymbol{s}(k-i), \tag{1.79}$$

such that d is the dimensionality of the tensor. An advantage of this method, besides the computationally efficient scheme, is that the control law is fully data-driven and does not require any prior information.

Besides the turbulence dynamics, Kronecker structures also appear in other matrices. For example, the SH geometry matrix G can, when assuming a square aperture, be

formulated using Kronecker products as $G = [(G_1 \otimes G_2)^T \ (G_2 \otimes G_1)^T]^T$, where the two blocks represents the slopes in x- and y-direction, respectively. Moreover, the DM influence matrix H can often be approximated as $H = H_1 \otimes H_2$ when assuming a square aperture. This relation holds only when the influence functions H_i in (1.33) are separable functions, i.e. H_i are all rank-1 matrices. One of such two-dimensional separable functions is the two-dimensional Gaussian function, which often accurately capture the influence function of the DM actuators. Also the Gaussian radial basis function discussed in Section 1.2.4 are separable.

1.5.3. THE IMPORTANCE OF THE FFT ALGORITHM

The equation defining the relation between the PSF and wavefront, given by (1.16), contains another special structure that can be used in efficient computations. It was stated in (1.16) that, in a matrix formulation, the DFT can be seen as a matrix vector product of the form:

$$\mathscr{F}_{vec}(\boldsymbol{x}) = (D \otimes D)\boldsymbol{x}, \tag{1.80}$$

and, using the relation $\text{vec}(AXB) = (B^H \otimes A)\text{vec}(X)$, this also means that

$$\mathscr{F}(\boldsymbol{x}) = DXD^T. \tag{1.81}$$

This shows that the DFT has clear similarities with the Kronecker structures presented in the previous subsection. This is expected, as the two-dimensional DFT is a separable function. However, the DFT has more properties, as the matrix D itself is symmetric, unitary and highly structured. FFT algorithms exploit the structures in the DFT matrix, decreasing the computational complexity of computing the DFT of an n-dimensional signal to $\mathscr{O}(n \log n)$.

Many methods that rely on computations of the PSF from a known GPF and vice versa, exploit the speed of FFT algorithms to formulate fast algorithms. A well-known example is the Gerchberg-Saxton phase retrieval algorithm. Modal decompositions as discussed in Section 1.2.4 are less likely to speed up this class of algorithms, the main reason being that AP methods are fast due to their efficient exploitation of the underlying matrix structures by the using the FFT. Decomposing the wavefront or GPF in modal basis functions can destroy those structures, which will increase the computational complexity of the algorithm.

1.5.4. OTHER MATRIX STRUCTURES

Although the existing literature mainly seems to focus on sparsity and Kronecker/tensor structures in AO, there are other structures that could be of interest. With the recent increase in popularity of the Ensemble Kalman filters (EnKF), its usefulness for AO was shown in [110]. The EnKF is based on the propagation of a small ensemble of states, which, in a way, means that the EnKF relies on a low-rank approximation of the error-covariance matrix P. Especially when P is banded, a technique called localization can be used to improve the performance of the filter. Since P is not necessarily banded for AO systems, these implicit low-rank approximations are not based on an underlying physical structure, such that the approximation might introduce more significant model errors than other structured models.

Finally, a structure that often appears in the modelling of interconnected systems is the sequantially semi-separable (SSS) matrix structure. This structure has been used to predict the wavefront in [111]. This method, however, relies heavily on the frozen flow assumption and decomposes the wavefront into columns that are being shifted over time. By doing so, when the direction of the wind is known, the problem is reduced to being only one-dimensional.

1.6. MOTIVATION AND OUTLINE OF THE THESIS

The presented algorithms for large-scale AO systems in Section 1.5 have in common that they consider an AO system that includes a Shack-Hartmann wavefront sensor. From an optimization perspective, the main advantage of using a WFS is that in this case wavefront estimation involves solving a convex optimization problem. Due to the non-linear relation between the wavefront and PSF, focal-plane sensing will involve non-convex optimization, which is notoriously harder to solve and has limited theoretical guarantees in terms of uniqueness of the solution and convergence to a global (or even local) optimum. Therefore, estimating the wavefront from PSF images only is usually not considered a suitable candidate for large-scale AO.

Nonetheless, this thesis will focus the reconstruction (and/or compensation of) wavefront aberrations based on PSF images. The wavefront aberrations are assumed to have a certain temporal dynamics and the wavefront reconstructions should ideally be performed in real-time, making accurate predictions and computationally efficient algorithms important aspects of this thesis.

Very briefly summarized, this thesis can be seen as an analysis of the challenges arising for focal-plane reconstruction methods and it presents several algorithms that, each in their own way, deal with these challenges. The remainder of this section will further discuss the main motivations of this thesis and presents the outline of the chapters.

1.6.1. MOTIVATION OF THE THESIS

In order to accentuate the connections between the separate chapters, two main motivations, some of which have already been mentioned in earlier sections, are discussed. Although each chapter focuses on a different setting with their own distinct motivation and main contributions, they can be grouped into two main research directions. The first is to consider the temporal dynamics of the wavefront aberrations as a source of useful information which can be used to improve focal-plane wavefront reconstruction methods. The second is to develop algorithms that keep in mind the immense number of inputs, outputs and variables present in large-scale AO systems. Although both of these topics are by now well-established in WFS-based wavefront estimation algorithms, similar research into large-scale dynamic aberrations for focal-plane methods is new, to the best knowledge of the author.

USING TEMPORAL DYNAMICS AS A SOURCE OF USEFUL INFORMATION

As explained in Section 1.1.2, the cause of the wavefront aberrations in ground-based telescopes is the presence of turbulence within the Earth's atmosphere. Since turbulence is a physical process with a certain temporal evolution, the wavefront aberrations will be changing over time. Estimating the wavefront while neglecting these temporal

dynamics results in an additional estimation error, known as the temporal error given by 1.52. Minimizing this temporal error forms an additional challenge on top of the large-scale and non-linear optimization challenge that is already being faced, as the developed techniques need to model the wavefront dynamics and predict its evolution over time. Although most of the theory presented in this thesis is developed with the application of AO for astronomy in mind, the theory can be extended to other applications that face similar challenges regarding temporally dynamic aberrations.

The view that the temporal evolution of the wavefront dynamics mainly forms an additional source of errors on top of an already difficult problem, however, might not be complete. One of the most important realizations of this thesis is that wavefront aberrations also give an extra insight when estimating a time-series of wavefront aberrations. In some cases, the temporal evolution can even be seen as a source of information rather than a source of errors. This reasoning has been a central concept in filtering and estimation techniques. State-observers, such as the Kalman filter, have been developed to use the temporal dynamics of a model to their advantage in reconstructing and predicting hidden states in the system. Similarly, the wavefront dynamics can be used to overcome certain issues regarding non-uniqueness of the phase retrieval problem by reformulating the problem as a filtering problem, as the the notion of *uniqueness* of the (static) phase retrieval has become the notion of *observability* in a filtering context.

A number of different classes of algorithms for the phase retrieval problem were discussed in Section 1.2.3. Each algorithm typically has one or several important limitations that decrease their applicability in AO systems. For example, some algorithms have a large sensitivity to measurement noise, a heavy dependence on an accurate initial estimate, or the need for many phase diversity images to be taken simultaneously. Kalman filters are known to optimally deal with measurement noise and their prediction naturally forms a good initial estimate to the phase retrieval problem. Furthermore, the additional information given by a dynamic model has the potential to be used in order to overcome problems regarding uniqueness and convergence.

Of course, it has to be assumed that an accurate model of the aberration dynamics, e.g. the model given by (1.73)-(1.74), is known or can be computed. Section 1.4 discussed several approaches to obtain a model of the temporal evolution of the wavefronts from first principles and from data. As the required information necessary to model the dynamics from first principles is not available, this thesis uses data-driven methods to identify the model dynamics. In particular, it will apply structured modelling and system identification techniques that exploit the sparsity of the system matrices as discussed in Section 1.5.1.

This vision of the wavefront dynamics as a source of prior information and the link between focal-plane wavefront estimation and non-linear Kalman filtering forms one of the research directions in this thesis. In chapters 3 and 4, it will be analyzed whether modelling the temporal evolution of wavefront aberrations and applying Kalman filter theory can help focal-plane sensing and WFSless AO methods not only to obtain a more accurate prediction, but also to overcome problems regarding uniqueness, convergence and robustness to noise.

DEALING WITH LARGE-SCALE AO SYSTEMS

Another challenge for the development of AO algorithms in general is the large number of inputs, outputs and variables that have to be modelled and estimated. Dealing with large amounts of data and variables causes issues with large computer storage requirements and computational complexity. Especially for the non-linear optimization problem underlying focal-plane sensing, conventional solvers are unsuitable for large-scale and real-time application. For example, the classical extended Kalman filter mentioned in Section 1.4.3 requires a number of elementary computations per time step that scales with $\mathcal{O}(n^3)$, n being the total number of pixels of the wavefront reconstruction. Performing the wavefront reconstruction in as little time as possible is thus an important criteria for suitable methods and the development of new computationally efficient algorithms is necessary in order to make focal-plane wavefront sensing suitable for large-scale AO systems.

The most straightforward way of lifting this curse of dimensionality is to decrease the number of variables in the optimization problem. Since decreasing the size of the optical system itself is not an option, one could decrease the number of variables by using a modal description of the GPF or wavefront. As discussed in Section 1.2.4, Zernike polynomials have been used for many decades as a modal representation of the wavefront in AO and this representation was extended to the complex-valued GPF with the introduction of extended Nijboer-Zernike polynomials. Other basis functions have not gained such wide-spread popularity and their behaviour and advantages for modelling aberrated optical fields have not been widely studied. This has left an opportunity to investigate different modal basis functions to represent the wavefront or GPF. Chapter 1 analyzes the advantages of Gaussian radial basis functions over ENZ polynomials for solving high-resolution phase retrieval problems.

Adopting a lower-dimensional modal representation is not the only way to decrease the number of variables. Some iterative WFSless AO methods have been proposed that only partially update the aberration correction per time step, which can significantly reduce the number of variables. However, this does not solve the problem as it just shifts the majority of the computation to a future time. When it is not necessary for all modes to be updated from the measurements, for example because they can be accurately predicted based on an available model, this approach becomes relevant. Such a method will be discussed in Chapter 4, which uses the knowledge of the wavefront's temporal evolution to predict the majority of the wavefront, only updating the uncertain areas based on new measurements. This shows that the two main motivations of this thesis are related, as one of the uses of having and knowing the temporal dynamics can be to reduce the complexity of WFSless AO algorithms.

1.6.2. OUTLINE OF THE THESIS

The organization of the remaining chapters is summarized below. Each chapter can be read independently, as the necessary background, literature and notations are reintroduced within each chapter separately. The contents of Chapters 2, 3 and 4 have been published elsewhere. The publications on which these chapters are based are listed.

Chapter 2: Modal-based phase retrieval using Gaussian radial basis functions

This chapter uses Gaussian radial basis functions to represent the generalized pupil function for solving the phase retrieval problem. The contents of this chapter have been published in:

Piscaer, P., Gupta, A., Soloviev, O., Verhaegen, M., *Modal-based phase retrieval using Gaussian radial basis functions*, JOSA A, 35, 1233 (2018)

Chapter 3: Phase retrieval of large-scale time-varying aberrations using a non-linear Kalman filtering framework
A computationally efficient framework in which a single focal-plane image is used to obtain a high-resolution reconstruction of a dynamic aberration is presented in this chapter. A non-linear Kalman filter implementation is developed whose computational complexity scales almost linearly with the number of pixels of the focal-plane camera. This chapter has been published in:

Piscaer, P., Soloviev, O., Verhaegen, M. *Phase retrieval of large-scale time-varying aberrations using a non-linear Kalman filtering framework*, JOSA A 38, 25 (2021)

Chapter 4: Predictive wavefront sensorless adaptive optics for time-varying aberrations
In this chapter, a new wavefront sensorless adaptive optics method is presented that is based on the linear relation between the mean square of the aberration gradient and the change in second moment of the image. The new algorithm applies Kalman filter theory to formulate an optimal controller that updates the actuators sequentially, by using the information of the Kalman filter to select and update the actuators. This chapter has been published in:

Piscaer, P., Soloviev, O., Verhaegen, M. *Predictive wavefront sensorless adaptive optics for time-varying aberrations*, JOSA A, 36, 1810 (2019)

Chapter 5: Conclusions and recommendations
In the final chapter of this thesis, the main findings are summarized and a number suggestions for future research are presented.

Matlab code
Finally, MATLAB code has been developed during this thesis that aims to develop a realistic simulation test-bench for advanced control and prediction methods for AO based on the OOMAO toolbox [112]. The code is available on the following Bitbucket repository:

`https://bitbucket.org/csi-dcsc/aotestbench`.

Besides it being a general framework that needs to be extended, it contains the implementation of a number of methods including modal-based phase retrieval using Gaussian radial basis functions and the efficient non-linear Kalman filter presented in Chap-

ter 3. This code has furthermore been discussed in:

Piscaer, P., Soloviev, O., Verhaegen, M. *Challenges in simulating advanced control methods for AO*, Proc. SPIE 11448, Adaptive Optics Systems VII (2020)

REFERENCES

[1] D. R. Luke, J. V. Burke, and R. G. Lyon, *Optical wavefront reconstruction: Theory and numerical methods,* SIAM review **44**, 169 (2002).

[2] J. W. Goodman, *Introduction to Fourier optics* (Roberts and Company Publishers, 2005).

[3] J. Schmidt, *Numerical simulation of optical wave propagation with examples in matlab,* (Society of Photo-Optical Instrumentation Engineers, 2010).

[4] J. W. Hardy, *Adaptive optics for astronomical telescopes*, Vol. 16 (Oxford University Press on Demand, 1998).

[5] J. Herrmann, *Phase variance and strehl ratio in adaptive optics,* Journal of the Optical Society of America A **9**, 2257 (1992).

[6] A. N. Kolmogorov, *The local structure of turbulence in incompressible viscous fluid for very large reynolds numbers,* Proceedings of the Royal Society of London. Series A: Mathematical and Physical Sciences **434**, 9 (1991).

[7] D. L. Fried, *Statistics of a geometric representation of wavefront distortion,* Journal of the Optical Society of America **55**, 1427 (1965).

[8] R. J. Noll, *Zernike polynomials and atmospheric turbulence,* Journal of the Optical Society of America **66**, 207 (1976).

[9] L. C. Andrews and R. L. Phillips, *Laser beam propagation through random media,* (SPIE, 2005).

[10] R. Conan, *Mean-square residual error of a wavefront after propagation through atmospheric turbulence and after correction with zernike polynomials,* Journal of the Optical Society of America A **25**, 526 (2008).

[11] G. I. Taylor, *The spectrum of turbulence,* Proceedings of the Royal Society of London. Series A-Mathematical and Physical Sciences **164**, 476 (1938).

[12] R. K. Tyson, *Principles of adaptive optics* (CRC press, 2015).

[13] F. Roddier, *Adaptive optics in astronomy* (Cambridge university press, 1999).

[14] Y. Shechtman, Y. C. Eldar, O. Cohen, H. N. Chapman, J. Miao, and M. Segev, *Phase retrieval with application to optical imaging: a contemporary overview,* IEEE signal processing magazine **32**, 87 (2015).

[15] K. Jaganathan, Y. C. Eldar, and B. Hassibi, *Phase retrieval: An overview of recent developments,* arXiv:1510.07713 (2015).

[16] R. A. Gonsalves, *Phase retrieval and diversity in adaptive optics,* Optical Engineering **21**, 215829 (1982).

[17] R. G. Paxman, T. J. Schulz, and J. R. Fienup, *Joint estimation of object and aberrations by using phase diversity,* Journal of the Optical Society of America A **9**, 1072 (1992).

[18] L. M. Mugnier, A. Blanc, and J. Idier, *Phase diversity: a technique for wave-front sensing and for diffraction-limited imaging,* Advances in Imaging and Electron Physics **141**, 1 (2006).

[19] R. W. Gerchberg, *A practical algorithm for the determination of the phase from image and diffraction plane pictures,* Optik **35**, 237 (1972).

[20] J. R. Fienup, *Reconstruction of an object from the modulus of its fourier transform,* Optics Letters **3**, 27 (1978).

[21] J. R. Fienup, *Phase retrieval algorithms: a comparison,* Applied Optics **21**, 2758 (1982).

[22] H. H. Bauschke, P. L. Combettes, and D. R. Luke, *Hybrid projection–reflection method for phase retrieval,* Journal of the Optical Society of America A **20**, 1025 (2003).

[23] V. Elser, *Solution of the crystallographic phase problem by iterated projections,* Acta Crystallographica Section A: Foundations of Crystallography **59**, 201 (2003).

[24] D. R. Luke, *Relaxed averaged alternating reflections for diffraction imaging,* Inverse problems **21**, 37 (2004).

[25] C.-C. Chen, J. Miao, C. Wang, and T. Lee, *Application of optimization technique to noncrystalline x-ray diffraction microscopy: Guided hybrid input-output method,* Physical Review B **76**, 064113 (2007).

[26] N. Hieu Thao, O. Soloviev, and M. Verhaegen, *Convex combination of alternating projection and douglas-rachford operators for phase retrieval,* arXiv:2002.01678 .

[27] H. H. Bauschke, P. L. Combettes, and D. R. Luke, *Phase retrieval, error reduction algorithm, and fienup variants: a view from convex optimization,* Journal of the Optical Society of America A **19**, 1334 (2002).

[28] D. R. Luke, N. H. Thao, and M. K. Tam, *Quantitative convergence analysis of iterated expansive, set-valued mappings,* Mathematics of Operations Research **43**, 1143 (2018).

[29] E. J. Candes, T. Strohmer, and V. Voroninski, *Phaselift: Exact and stable signal recovery from magnitude measurements via convex programming,* Communications on Pure and Applied Mathematics **66**, 1241 (2013).

[30] E. J. Candes, Y. C. Eldar, T. Strohmer, and V. Voroninski, *Phase retrieval via matrix completion,* SIAM review **57**, 225 (2015).

[31] I. Waldspurger, A. d'Aspremont, and S. Mallat, *Phase recovery, maxcut and complex semidefinite programming,* Mathematical Programming **149**, 47 (2015).

[32] T. Goldstein and C. Studer, *Phasemax: Convex phase retrieval via basis pursuit,* IEEE Transactions on Information Theory **64**, 2675 (2018).

[33] R. Doelman, N. H. Thao, and M. Verhaegen, *Solving large-scale general phase retrieval problems via a sequence of convex relaxations,* Journal of the Optical Society of America A **35**, 1410 (2018).

[34] E. J. Candès and X. Li, *Solving quadratic equations via phaselift when there are about as many equations as unknowns,* Foundations of Computational Mathematics **14**, 1017 (2014).

[35] I. Waldspurger, *Phase retrieval with random gaussian sensing vectors by alternating projections,* IEEE Transactions on Information Theory **64**, 3301 (2018).

[36] E. J. Candes, X. Li, and M. Soltanolkotabi, *Phase retrieval via wirtinger flow: Theory and algorithms,* IEEE Transactions on Information Theory **61**, 1985 (2015).

[37] Y. Chen and E. Candes, *Solving random quadratic systems of equations is nearly as easy as solving linear systems,* in *Advances in Neural Information Processing Systems* (2015) pp. 739–747.

[38] P. Netrapalli, P. Jain, and S. Sanghavi, *Phase retrieval using alternating minimization,* in *Advances in Neural Information Processing Systems* (2013) pp. 2796–2804.

[39] J. Sun, Q. Qu, and J. Wright, *A geometric analysis of phase retrieval,* Foundations of Computational Mathematics **18**, 1131 (2018).

[40] C. Ma, X. Liu, and Z. Wen, *Globally convergent levenberg-marquardt method for phase retrieval,* IEEE Transactions on Information Theory **65**, 2343 (2018).

[41] G. Wang, G. B. Giannakis, and Y. C. Eldar, *Solving systems of random quadratic equations via truncated amplitude flow,* IEEE Transactions on Information Theory **64**, 773 (2017).

[42] J. Antonello and M. Verhaegen, *Modal-based phase retrieval for adaptive optics,* Journal of the Optical Society of America A **32**, 1160 (2015).

[43] J. Braat, P. Dirksen, and A. J. Janssen, *Assessment of an extended nijboer–zernike approach for the computation of optical point-spread functions,* Journal of the Optical Society of America A **19**, 858 (2002).

[44] A. J. Janssen, *Extended nijboer–zernike approach for the computation of optical point-spread functions,* Journal of the Optical Society of America A **19**, 849 (2002).

[45] A. Martinez-Finkelshtein, D. Ramos-Lopez, and D. Iskander, *Computation of 2d fourier transforms and diffraction integrals using gaussian radial basis functions,* Applied and Computational Harmonic Analysis **43**, 424 (2017).

[46] B. Fornberg, E. Larsson, and N. Flyer, *Stable computations with gaussian radial basis functions,* SIAM Journal on Scientific Computing **33**, 869 (2011).

[47] D. L. Fried, *Least-square fitting a wave-front distortion estimate to an array of phase-difference measurements,* Journal of the Optical Society of America **67**, 370 (1977).

[48] J. Herrmann, *Least-squares wave front errors of minimum norm,* Journal of the Optical Society of America **70**, 28 (1980).

[49] R. H. Hudgin, *Wave-front reconstruction for compensated imaging,* Journal of the Optical Society of America **67**, 375 (1977).

[50] M. Verhaegen and V. Verdult, *Filtering and system identification: a least squares approach* (Cambridge university press, 2007).

[51] E. P. Wallner, *Optimal wave-front correction using slope measurements,* Journal of the Optical Society of America **73**, 1771 (1983).

[52] B. Ellerbroek and T. Rhoadarmer, *Adaptive wavefront control algorithms for closed loop adaptive optics,* Mathematical and Computer modelling **33**, 145 (2001).

[53] B. L. Ellerbroek, *Efficient computation of minimum-variance wave-front reconstructors with sparse matrix techniques,* Journal of the Optical Society of America A **19**, 1803 (2002).

[54] M. A. Vorontsov, G. W. Carhart, M. Cohen, and G. Cauwenberghs, *Adaptive optics based on analog parallel stochastic optimization: analysis and experimental demonstration,* Journal of the Optical Society of America A **17**, 1440 (2000).

[55] S. Zommer, E. Ribak, S. Lipson, and J. Adler, *Simulated annealing in ocular adaptive optics,* Optics Letters **31**, 939 (2006).

[56] P. Yang, M. Ao, Y. Liu, B. Xu, and W. Jiang, *Intracavity transverse modes controlled by a genetic algorithm based on zernike mode coefficients,* Optics Express **15**, 17051 (2007).

[57] Q. Yang, J. Zhao, M. Wang, and J. Jia, *Wavefront sensorless adaptive optics based on the trust region method,* Optics Letters **40**, 1235 (2015).

[58] P. Marsh, D. Burns, and J. Girkin, *Practical implementation of adaptive optics in multiphoton microscopy,* Optics express **11**, 1123 (2003).

[59] J. Antonello, T. van Werkhoven, M. Verhaegen, H. H. Truong, C. U. Keller, and H. C. Gerritsen, *Optimization-based wavefront sensorless adaptive optics for multiphoton microscopy,* Journal of the Optical Society of America A **31**, 1337 (2014).

[60] H. Linhai and C. Rao, *Wavefront sensorless adaptive optics: a general model-based approach,* Optics express **19**, 371 (2011).

[61] H. Yang, O. Soloviev, and M. Verhaegen, *Model-based wavefront sensorless adaptive optics system for large aberrations and extended objects,* Optics express **23**, 24587 (2015).

[62] M. J. Booth, *Wavefront sensorless adaptive optics for large aberrations,* Optics Letters **32**, 5 (2007).

[63] M. A. Neil, M. J. Booth, and T. Wilson, *New modal wave-front sensor: a theoretical analysis,* Journal of the Optical Society of America A **17**, 1098 (2000).

[64] D. Débarre, M. J. Booth, and T. Wilson, *Image based adaptive optics through optimisation of low spatial frequencies,* Optics Express **15**, 8176 (2007).

[65] H. Song, R. Fraanje, G. Schitter, H. Kroese, G. Vdovin, and M. Verhaegen, *Model-based aberration correction in a closed-loop wavefront-sensor-less adaptive optics system,* Optics express **18**, 24070 (2010).

[66] D. Débarre, E. J. Botcherby, T. Watanabe, S. Srinivas, M. J. Booth, and T. Wilson, *Image-based adaptive optics for two-photon microscopy,* Optics Letters **34**, 2495 (2009).

[67] R. A. Gonsalves, *Small-phase solution to the phase-retrieval problem,* Optics Letters **26**, 684 (2001).

[68] C. Smith, R. Marinică, A. Den Dekker, M. Verhaegen, V. Korkiakoski, C. Keller, and N. Doelman, *Iterative linear focal-plane wavefront correction,* Journal of the Optical Society of America A **30**, 2002 (2013).

[69] S. Meimon, T. Fusco, and L. M. Mugnier, *Lift: a focal-plane wavefront sensor for real-time low-order sensing on faint sources,* Optics Letters **35**, 3036 (2010).

[70] V. Korkiakoski, C. U. Keller, N. Doelman, M. Kenworthy, G. Otten, and M. Verhaegen, *Fast & furious focal-plane wavefront sensing,* Applied Optics **53**, 4565 (2014).

[71] R. A. Gonsalves, *Sequential diversity imaging: Phase diversity with ao changes as the diversities,* (Optical Society of America, 2010).

[72] D. P. Greenwood, *Bandwidth specification for adaptive optics systems,* Journal of the Optical Society of America **67**, 390 (1977).

[73] D. L. Fried, *Time-delay-induced mean-square error in adaptive optics,* Journal of the Optical Society of America A **7**, 1224 (1990).

[74] L. Ljung, *System identification,* Wiley encyclopedia of electrical and electronics engineering (1999).

[75] A. Beghi, A. Cenedese, and A. Masiero, *Stochastic realization approach to the efficient simulation of phase screens,* Journal of the Optical Society of America A **25**, 515 (2008).

[76] K. Hinnen, M. Verhaegen, and N. Doelman, *A data-driven $\mathscr{H}_2$-optimal control approach for adaptive optics,* IEEE Transactions on Control Systems Technology **16**, 381 (2008).

[77] R. E. Kalman, *A new approach to linear filtering and prediction problems,* (1960).

[78] R. Paschall, M. Von Bokern, and B. Welsh, *Design of a linear quadratic gaussian controller for an adaptive optics system,* in *Proceedings of the 30th IEEE Conference on Decision and Control* (IEEE, 1991) pp. 1761–1769.

[79] B. Le Roux, J.-M. Conan, C. Kulcsár, H.-F. Raynaud, L. M. Mugnier, and T. Fusco, *Optimal control law for classical and multiconjugate adaptive optics,* Journal of the Optical Society of America A **21**, 1261 (2004).

[80] C. Kulcsár, H.-F. Raynaud, C. Petit, J.-M. Conan, and P. V. De Lesegno, *Optimal control, observers and integrators in adaptive optics,* Optics express **14**, 7464 (2006).

[81] C. Kulcsár, H.-F. Raynaud, C. Petit, and J.-M. Conan, *Minimum variance prediction and control for adaptive optics,* Automatica **48**, 1939 (2012).

[82] B. D. Anderson and J. B. Moore, *Optimal filtering* (Courier Corporation, 2012).

[83] S. Julier, J. Uhlmann, and H. F. Durrant-Whyte, *A new method for the nonlinear transformation of means and covariances in filters and estimators,* IEEE Transactions on automatic control **45**, 477 (2000).

[84] S. J. Julier and J. K. Uhlmann, *Unscented filtering and nonlinear estimation,* Proceedings of the IEEE **92**, 401 (2004).

[85] K. Ito and K. Xiong, *Gaussian filters for nonlinear filtering problems,* IEEE transactions on automatic control **45**, 910 (2000).

[86] G. Evensen, *Sequential data assimilation with a nonlinear quasi-geostrophic model using monte carlo methods to forecast error statistics,* Journal of Geophysical Research: Oceans **99**, 10143 (1994).

[87] I. Arasaratnam and S. Haykin, *Cubature kalman filters,* IEEE Transactions on automatic control **54**, 1254 (2009).

[88] M. NøRgaard, N. K. Poulsen, and O. Ravn, *New developments in state estimation for nonlinear systems,* Automatica **36**, 1627 (2000).

[89] I. Arasaratnam, S. Haykin, and R. J. Elliott, *Discrete-time nonlinear filtering algorithms using gauss–hermite quadrature,* Proceedings of the IEEE **95**, 953 (2007).

[90] B. M. Bell and F. W. Cathey, *The iterated kalman filter update as a gauss-newton method,* IEEE Transactions on Automatic Control **38**, 294 (1993).

[91] M. Roth, G. Hendeby, and F. Gustafsson, *Nonlinear kalman filters explained: A tutorial on moment computations and sigma point methods,* Journal of Advances in Information Fusion **11**, 47 (2016).

[92] F. Gustafsson, *Particle filter theory and practice with positioning applications,* IEEE Aerospace and Electronic Systems Magazine **25**, 53 (2010).

[93] M. Roth, G. Hendeby, C. Fritsche, and F. Gustafsson, *The ensemble kalman filter: a signal processing perspective,* EURASIP Journal on Advances in Signal Processing **2017**, 56 (2017).

[94] C. Smith, R. Marinica, and M. Verhaegen, *Real-time wavefront reconstruction from intensity measurements,* in *Proceedings of the 3rd AO4ELT Conference* (Arcetri Astrophysical Observatory, 2013).

[95] C. S. Smith, R. Marinică, J. Antonello, J. Arnold, and M. Verhaegen, *Focal-plane wavefront estimation and control using the extended kalman filter,* in *2012 International Symposium on Optomechatronic Technologies* (IEEE, 2012) pp. 1–6.

[96] R. Marinică, C. S. Smith, and M. Verhaegen, *State feedback control with quadratic output for wavefront correction in adaptive optics,* in *52nd IEEE Conference on Decision and Control* (IEEE, 2013) pp. 3475–3480.

[97] W. Lianghua, P. Yang, W. Shuai, L. Wenjing, C. Shanqiu, and B. Xu, *A high speed model-based approach for wavefront sensorless adaptive optics systems,* Optics & Laser Technology **99**, 124 (2018).

[98] P. Massioni, C. Kulcsár, H.-F. Raynaud, and J.-M. Conan, *Fast computation of an optimal controller for large-scale adaptive optics,* Journal of the Optical Society of America A **28**, 2298 (2011).

[99] C. Correia, J.-M. Conan, C. Kulcsár, H.-F. Raynaud, and C. Petit, *Adapting optimal lqg methods to elt-sized ao systems,* in *1st AO4ELT conference-Adaptive Optics for Extremely Large Telescopes* (EDP Sciences, 2010).

[100] P. Massioni, H.-F. Raynaud, C. Kulcsár, and J.-M. Conan, *An approximation of the riccati equation in large-scale systems with application to adaptive optics,* IEEE transactions on control systems technology **23**, 479 (2014).

[101] A. Beghi, A. Cenedese, and A. Masiero, *On the computation of kalman gain in large adaptive optics systems,* in *21st Mediterranean Conference on Control and Automation* (IEEE, 2013) pp. 1374–1379.

[102] S. L. Lauritzen, *Graphical models*, Vol. 17 (Clarendon Press, 1996).

[103] C. W. Granger, *Investigating causal relations by econometric models and cross-spectral methods,* Econometrica: journal of the Econometric Society , 424 (1969).

[104] J. Songsiri, J. Dahl, and L. Vandenberghe, *Graphical models of autoregressive processes.* Convex Optimization in Signal Processing and Communications (2009).

[105] P. Piscaer, *Sparse VARX Model Identification for Large-Scale Adaptive Optics*, Master's thesis, TU Delft (2016), retrieved from http://resolver.tudelft.nl/uuid:9677ebd9-cf4c-484c-97f8-1f553cd0e873.

[106] C. Yu and M. Verhaegen, *Structured modeling and control of adaptive optics systems,* IEEE Transactions on Control Systems Technology **26**, 664 (2018).

[107] G. Monchen, B. Sinquin, and M. Verhaegen, *Recursive kronecker-based vector autoregressive identification for large-scale adaptive optics,* IEEE Transactions on Control Systems Technology **27**, 1677 (2018).

[108] B. Sinquin and M. Verhaegen, *Quarks: identification of large-scale kronecker vector-autoregressive models,* IEEE Transactions on Automatic Control **64**, 448 (2018).

[109] B. Sinquin and M. Verhaegen, *Tensor-based predictive control for extremely large-scale single conjugate adaptive optics,* Journal of the Optical Society of America A **35**, 1612 (2018).

[110] M. Gray, C. Petit, S. Rodionov, M. Bocquet, L. Bertino, M. Ferrari, and T. Fusco, *Local ensemble transform kalman filter, a fast non-stationary control law for adaptive optics on elts: theoretical aspects and first simulation results,* Optics express **22**, 20894 (2014).

[111] R. Fraanje, J. Rice, M. Verhaegen, and N. Doelman, *Fast reconstruction and prediction of frozen flow turbulence based on structured kalman filtering,* Journal of the Optical Society of America A **27**, A235 (2010).

[112] R. Conan and C. Correia, *Object-oriented matlab adaptive optics toolbox,* in *Adaptive Optics Systems IV*, Vol. 9148, edited by E. Marchetti, L. M. Close, and J.-P. Véran, International Society for Optics and Photonics (SPIE) pp. 2066 – 2082.

2

MODAL-BASED PHASE RETRIEVAL USING GAUSSIAN RADIAL BASIS FUNCTIONS

In this chapter, we propose the use of Gaussian radial basis functions (GRBF) to model the generalized pupil function for phase retrieval. The selection of the GRBF hyper-parameters are analyzed to achieve an increased accuracy of approximation. The performance of the GRBF-based method is compared in a simulation study with another modal-based approach considering extended Nijboer-Zernike (ENZ) polynomials. The almost local character of the GRBF makes them a much more flexible basis with respect to the pupil geometry. It has been shown that for aberrations containing higher spatial frequencies, the GRBF outperform ENZ polynomials significantly even on a circular pupil. Moreover, the flexibility has been demonstrated by considering the phase retrieval problem on an annular pupil.

The contents of this chapter have been published in Piscaer, P., et al. *Modal-based phase retrieval using Gaussian radial basis functions*, JOSA A 35, 1233 (2018).

2.1. INTRODUCTION

In the phase retrieval (PR) problem, the phase of a complex-valued function is recovered from measurements of the magnitude of its Fourier transform. This inverse problem has many different applications in optical imaging; see [1] for a contemporary overview. Algorithmic phase retrieval based optical wavefront reconstruction offers an attractive means of estimating the complex generalized pupil function (GPF) from a set of measurements of the point-spread functions (PSF) in adaptive optics due to its experimental simplicity [1, 2]. Moreover, other additional optical components, such as beam splitters and wavefront sensors, are not necessary, avoiding problems related to non-common path errors and a loss in observed light intensity.

Phase retrieval algorithms can be divided into two subcategories. The classical and still most commonly implemented class of algorithms are the alternating projection (AP) methods, pioneered by Gerchberg and Saxton [3] and Fienup [4]. Recently, optimization-based algorithms representing the PR as a matrix completion problem have been developed [5–7]. The solution requires solving a matrix rank minimization problem, which is NP-hard. A convex relaxation was proposed using the trace norm as a convex surrogate to the rank operator, approximating the problem with a semidefinite program. More recently, another optimization-based approach to solve the phase retrieval problem was presented in [8]. This algorithm is shown to be superior in terms of computational complexity, making it more suitable for larger-scale phase retrieval problems. Both classes of algorithms use multiple images at different defocus planes, in order to resolve non-uniqueness issues. This technique improves the stability by incorporating extra information in the intensity measurements [2] and is one possible implementation of the more general concept of structured illumination (see [5]). A superiority in terms of convergence towards a unique solution and stability for noisy measurements makes the convex optimization-based approaches an interesting alternative to the AP methods [5, 9]. Moreover, these algorithms solve the PR problem by explicitly minimizing a cost function, making it easier to introduce structures such as sparsity.

The standard approach in both classes of algorithms is to aim for the recovery of the complete GPF in a pixel-basis, such that the measured PSF is the magnitude of the 2-dimensional Fourier transform of the signal to be recovered. Exploiting the computational efficiency of the fast Fourier transform, AP methods can be implemented very efficiently. However, the large number of variables corresponding to the pixel-wise representation are problematic for the optimization-based algorithms, making them suitable for small-scale applications only. In this chapter, we reduce the number of variables by modelling the GPF as a linear combination of modes as an alternative to the zonal pixel-by-pixel model. This approach was shown to be promising for the adaptive optics application [10], allowing the use of optimization-based phase retrieval on a conventional computer. A trade-off between approximation accuracy of the modal basis and computational effort defines the required number of modes to be used.

The complex-valued Zernike polynomials introduced as a consequence of the Extended Nijboer-Zernike (ENZ) theory [11, 12] formed the chosen basis in [10]. The major limitation of the global ENZ polynomial representation is that each term extends its influence over a circular pupil, making it inflexible with respect to the pupil geometry. The Zernike theory can be adapted to other pupil geometries. However, this requires a

complex reformulation of the basis for every different pupil. Moreover, they are subject to Runge's phenomenon, leading to oscillations on the edges of the domain. Recently, GPF approximation based on Gaussian radial basis functions (GRBF) was used for semi-analytic evaluation of the diffraction integral as an alternative to ENZ polynomials. An improvement in terms of complexity, accuracy and execution time was achieved [13]. An important feature of the GRBF is the almost local character of each function. Since the width and location of the GRBF are free to choose for each basis function, it offers a more intuitive basis to represent the GPF that is easier to implement for any arbitrary aperture geometry. This creates an increased flexibility to the geometry of the pupil function and the possibility to model local details and sharp features compared to ENZ polynomials.

This chapter is concerned with the application of GRBF as a modal decomposition of the GPF as an alternative for ENZ polynomials. The choice of several hyper-parameters that define the shape and placement of the GRBF are investigated. The relation between the numerical conditioning and the accuracy of the solution to PR problems is important in practical implementations [2, 14]. When the standard representation is ill-conditioned, algorithms such as RBF-QR [15] have been proposed to transform the GRBF into a well-conditioned basis. Therefore, this aspect of conditioning is not evaluated in this chapter. To test the performance of the new method, phase retrieval simulations are performed. Two types of aberrations are considered. First, aberration data is generated from a Zernike polynomial basis with its coefficients sampled from an assumed distribution based on empirically determined correction capabilities of a deformable mirror (DM) [10]. Secondly, aberrations corresponding to the correction capabilities of a higher-order DM are derived experimentally to create a phase disturbance with higher spatial frequencies. The PSF is simulated at multiple planes along the optical axis, introducing phase diversity in terms of defocus. The two different classes of basis functions, GRBF and ENZ polynomials, are compared in terms of their theoretical fitting accuracy and performance in modal-based phase retrieval algorithms.

The structure of the chapter is as follows. The formulation of the modal-based PR problem as an optimization problem is presented in Section 2.2. An overview of the different basis functions used to approximate the GPF is also contained in this section. The aberration data generation and simulation experiment design are discussed in Section 2.3. The theoretical GPF fitting accuracy for the GRBF, including the tuning of the hyper-parameters, is explained in Section 2.4. The simulation results for aberration retrieval for a number of different cases are presented in Section 2.5. Finally, the conclusions are drawn in Section 2.6.

2.2. MODAL BASED PHASE RETRIEVAL

A mathematical formulation of the phase retrieval problem is briefly presented in this section. The effects of aberrations on an optical system can be modelled using the generalized pupil function (GPF). The GPF is a complex function [2]

$$\mathscr{P}(\rho,\theta) = A(\rho,\theta)\exp(i\Phi(\rho,\theta)), \tag{2.1}$$

where $A(\cdot)$ and $\Phi(\cdot)$ are real-valued functions that denote the amplitude apodization function and phase aberration respectively and (ρ,θ) are the normalized polar coordinates on the exit pupil plane. Under the assumption of purely phase aberrated systems

with circular exit pupils, $A(\rho,\theta)$ is modelled as a characteristic function with unity values inside the pupil and zero outside. The field in the focal plane is related to that in the exit pupil by the following integral:

$$U(r,\phi,f) = \frac{1}{\pi}\int_0^1\int_0^{2\pi} \exp(if\rho^2)\mathscr{P}(\rho,\theta) \times \exp(i2\pi r\rho cos(\theta-\phi))\rho d\rho d\theta, \tag{2.2}$$

where (r,ϕ) are the polar coordinates in the focal region normalized with respect to the axial diffraction unit (λ/NA), NA being the image-side numerical aperture of the optical system. The defocus parameter f is used to deliberately introduce a defocus aberration to the GPF and is necessary for the convergence of optimization based phase retrieval algorithms [5]. $U(r,\phi,f)$ is the complex-valued point-spread function corresponding to the GPF. Only the intensity image of $U(r,\phi,f)$, called the point-spread function (PSF), is observed by the camera:

$$y(r,\phi,f) = |U(r,\phi,f)|^2. \tag{2.3}$$

In this chapter, we will define the phase retrieval (PR) problem as recovering the phase aberration $\Phi(\rho,\theta)$ from multiple focal-plane intensity measurements $y(r,\phi,f)$ with different introduced defocus f. Often, we will adopt a sampled representation in which both the GPF and (complex) PSF are sampled on an equally spaced square grid, denoted by $P \in \mathbb{C}^{N_p\times N_p}$ and $U_i \in \mathbb{C}^{N_u\times N_u}$ respectively, where the subscript i indicates the image at focal position $f = f_i$. The intensity measurements of U_i are vectorized into $\mathbf{y}_i \in \mathbb{R}^{N_u^2}$. The number of diversity images will be denoted by N_f.

A more concrete formulation of the phase retrieval problem requires a convenient and systematic parametrization of the GPF. The most flexible parametrization is a pixellation of the pupil, as it can be used with any pupil geometry. However, the pixel-basis requires a large number of parameters to be identified using PR. The large number of variables is problematic for the optimization based algorithms, since they cannot exploit the computational efficiency of the FFT as is done by alternating projection algorithms. Parametrizations based on approximating the GPF as a linear superposition of a small number of basis functions reduces the size of the problem dramatically, since it requires estimation of just a complex scalar coefficient for each of the basis functions. The introduction of this modal-decomposition allows the use of the computationally demanding optimization-based algorithms on a conventional computer [10]. Next, two different modal representations are presented.

2.2.1. EXTENDED NIJBOER-ZERNIKE POLYNOMIALS

The phase aberration Φ can be analyzed by the orthogonal set of basis functions formed by the circle polynomials, $\mathscr{Z}_n^m$, introduced by Zernike,

$$\Phi(\rho,\theta) = \sum_{n,m} \zeta_n^m \mathscr{Z}_n^m(\rho,\theta), \tag{2.4}$$

where indices $n \in \mathbb{N}_0$ and $m \in \mathbb{Z}$ respectively denote the radial order and the azimuthal frequency of the Zernike polynomial $\mathscr{Z}_n^m$ such that $n-|m| > 0$ and even. The polynomials are given by the product of a radial polynomial $R_n^{|m|}(\rho)$ and a trigonometric function

$\Theta_n^m(\theta)$ with suitable normalization c_n^m,

$$\mathcal{Z}_n^m(\rho,\theta) = c_n^m R_n^{|m|}\Theta_n^m(\theta). \tag{2.5}$$

where,

$$\begin{gathered} c_n^m = \begin{cases} \sqrt{n+1} & m=0 \\ \sqrt{2(n+1)} & m\neq 0 \end{cases}, \quad \Theta_n^m(\theta) = \begin{cases} cos(m\theta) & m\geq 0 \\ -sin(m\theta) & m<0 \end{cases}, \\ R_n^m(\rho) = \sum_{s=0}^{(n-m)/2} \frac{(-1)^s(n-s)!}{s!\left(\frac{n+m}{2}-s\right)!\left(\frac{n-m}{2}-s\right)!}\rho^{n-2s}. \end{gathered} \tag{2.6}$$

The representation of phase aberration Φ in terms of Zernike polynomials was generalized to represent the GPF under the Extended Nijboer-Zernike (ENZ) theory [11]. The GPF is approximated as a truncated series of ENZ polynomials [12],

$$\hat{\mathscr{P}}_E(\rho,\theta) = \sum_{n,m} \beta_n^m \mathcal{N}_n^m(\rho,\theta). \tag{2.7}$$

Here, n and m denote, respectively, the radial order and azimuthal frequency of the ENZ polynomial $\mathcal{N}_n^m(\rho,\theta)$:

$$\mathcal{N}_n^m(\rho,\theta) = \sqrt{n+1}R_n^{|m|}(\rho)\exp(im\theta). \tag{2.8}$$

The polynomials are ordered according to their radial order, such that the coefficients can be collected into a single vector $\boldsymbol{\beta} \in \mathbb{C}^{N_\beta}$ where $N_\beta = (n_M+1)(n_M+2)/2$, n_M being the maximum radial order considered. The normalization used here is as given in [10].

2.2.2. GAUSSIAN RADIAL BASIS FUNCTIONS

Alternatively, the pupil function can be approximated by a linear combination of Gaussian radial basis functions (GRBFs) [13]. The complex GPF is approximated by a real-valued, radially-symmetric GRBF,

$$\hat{\mathscr{P}}_R(\rho,\theta) = A(\rho,\theta)\sum_{k=1}^{N_\gamma} \gamma_k \Psi_k(\rho,\theta), \tag{2.9}$$

$$\Psi_k(\rho,\theta) = e^{-\lambda_k(\rho^2+\varrho_k^2-2\rho\varrho_k\cos(\theta-\vartheta_k))}, \tag{2.10}$$

where $\gamma_k \in \mathbb{C}$, (ϱ_k,ϑ_k) are the polar coordinates of the GRBF nodes on a polar grid and $A(\rho,\theta)$ is the same as in (2.1). Also, $\lambda_k > 0$ is the shape parameter inversely proportional to the width of the GRBF. Numerical conditioning of the basis is an important issue in RBF approximation. It should be noted that, in contrast to ENZ polynomials, the GRBFs are not orthogonal. Severe ill-conditioning can occur in the flat basis function limit ($\lambda_k \to 0$). In the literature, methods have been proposed that yield a well-conditioned basis, in which the basis functions are different, but together span the same space as the original GRBF set (see e.g. [15]). However, for the applications in this chapter, λ_k was chosen large enough such that no problems occurred due to ill-conditioning. To illustrate its shape, an example of a single GRBF is shown in Figure 2.1.

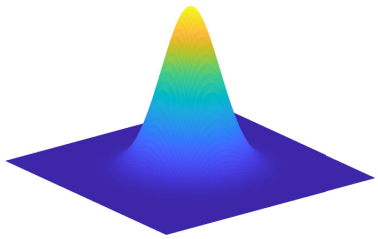

Figure 2.1: An example of a Gaussian radial basis function as defined in (2.10). The exact center location and width of the GRBF are defined by the parameters (ϱ_k, ϑ_k) and λ_k respectively.

2.2.3. PHASE RETRIEVAL AS AN OPTIMIZATION PROBLEM

Both modal representations in (2.7) and (2.9) can be expressed in the following form:

$$\hat{\mathscr{P}}(\rho,\theta) = \sum_{k=1}^{N_\alpha} \alpha_k \mathscr{B}_k(\rho,\theta) \tag{2.11}$$

with coefficients $\alpha_k \in \mathbb{C}$ and the basis functions $\mathscr{B}_k(\rho,\theta)$ represent either the ENZ polynomials or GRBFs. By sampling the the GPF on a regular $N_p \times N_p$ grid, such that each pixel corresponds to a location (ρ_i,θ_i), $i = 1,\ldots,N_p^2$, the basis functions and the estimated GPF can both be represented as a matrices:

$$\hat{P} = \sum_{k=1}^{N_\alpha} \alpha_k B_k \tag{2.12}$$

with $B_k \in \mathbb{C}^{N_p \times N_p}$ and $\hat{P} \in \mathbb{C}^{N_p \times N_p}$. After vectorizing this representation, the modal decomposition becomes a single matrix-vector multiplication:

$$\hat{\mathbf{p}} = B\boldsymbol{\alpha}, \tag{2.13}$$

such $\hat{\mathbf{p}} \in \mathbb{C}^{N_p^2}$, $\boldsymbol{\alpha} \in \mathbb{C}^{N_\alpha}$ and the k-th column of $B \in \mathbb{C}^{N_p^2 \times N_\alpha}$ is a vectorized representation of B_k.

Due to the linearity property of the diffraction integral in (2.2), the predicted PSF is a linear combination of transformed basis functions weighted by the same coefficients as the GPF. This transformation is performed using the two-dimensional discrete Fourier transform (DFT) denoted by $\mathscr{F}\{\cdot\}$. A sampled representation of U is represented on an $N_u \times N_u$ grid, where $N_u = DN_p$, $D \geq 1$ being a constant related to the diffraction limit of the optical system. The increase in dimensions $N_u - N_p$ is computationally realized by zero-padding of the GPF before taking the 2D-DFT. For an image at a position along the optical axis corresponding to a defocus parameter of f_d, the estimated complex image $\hat{U}_d$ can be written as:

$$\hat{U}_d = \sum_{k=1}^{N_\alpha} \alpha_k C_{d,k}, \tag{2.14}$$

where $C_{d,k} = \mathscr{F}\{B_k \odot P_d\} \in \mathbb{C}^{N_u \times N_u}$, $\odot$ represents the element-wise product and P_d is the defocus function $\exp(i f_d \rho^2)$ sampled on the same $N_p \times N_p$ grid as the basis functions extended with the correct zero-padding. Also, the modal decomposition of the complex image U_d can be represented as a matrix-vector multiplication, i.e. we define the vectorization of $\hat{U}_d$ as $\hat{\mathbf{u}}_d \in \mathbb{C}^{N_u^2}$ such that

$$\hat{\mathbf{u}}_d = C_d \boldsymbol{\alpha}, \tag{2.15}$$

with the k-th column of $C_d \in \mathbb{C}^{N_u^2 \times N_\alpha}$ containing the vectorized representation of $C_{d,k}$. Finally, the estimated intensity measurement (i.e. the PSF) is given by

$$\hat{\mathbf{y}}_d = |C_d \boldsymbol{\alpha}|^2. \tag{2.16}$$

The PR problem is formulated as the minimisation of the error between the measurements $\mathbf{y}_d$ and the estimated PSF $\hat{\mathbf{y}}_d$, leading to the following optimization problem:

$$\min_{\boldsymbol{\alpha} \in \mathbb{C}^{N_\alpha}} \sum_{d=1}^{N_f} \left\| \mathbf{y}_d - |C_d \boldsymbol{\alpha}|^2 \right\|, \tag{2.17}$$

where $\|\cdot\|$ denotes a vector norm of interest. This problem will be solved using an efficient optimization-based phase retrieval algorithm called COPR [8]. In principle, other optimization-based algorithms such as PhaseLift can be used. However, they are too computationally demanding for even medium sized problems. Since the goal of this method is to show the advantage of GRBFs for high-order aberrations, which require a larger number of basis functions, COPR is chosen because of its superior speed.

2.3. SIMULATION DESIGN

This section discusses the simulations that will be performed to analyze the advantage of using GRBF over ENZ polynomials. By considering their advantages and disadvantages as outlined in the introduction, we expect to show an improvement of GRBFs over ENZ polynomials for several cases. First of all, GRBFs are by definition more flexible to different pupil geometries, since ENZ polynomials are defined over the unit disk only. Moreover, it is expected that the GRBF representation is more suitable to fit higher spatial frequencies in the GPF. To validate this, we will test the PR problem on both low-order and high-order aberrations. The generation of both phase types are discussed below. Finally, the implementation details for the performed simulation experiments are presented.

2.3.1. GENERATION OF LOW-ORDER ABERRATIONS

For the generation of aberrations containing only lower spatial frequencies, the phase is represented in terms of Zernike polynomials:

$$\Phi(\rho,\theta) = \sum_{n,m} \zeta_n^m \mathcal{Z}_n^m(\rho,\theta), \tag{2.18}$$

where $\mathcal{Z}_n^m$ are the Zernike polynomials and the coefficients ζ_n^m are drawn from an assumed distribution. The distribution is based on the experimentally derived correction

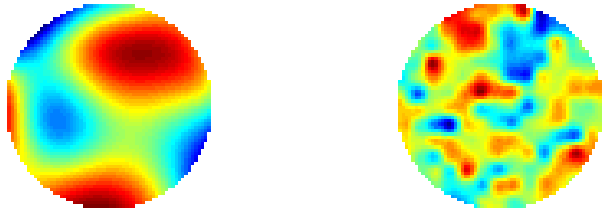

(a) Low-order aberration (b) High-order aberration

Figure 2.2: Example of a low-order and high-order aberration generated as described in Section 2.3.1 and 2.3.2 respectively. The amplitude of the phase can be scaled to any desired value.

capabilities of a low-order membrane DM [10], which followed approximately an exponential decrease in the values for ζ_n^m for increasing radial orders. The total number of Zernike terms considered is denoted by $N_z = (n_z+1)(n_z+2)/2$, where n_z is the maximum radial order considered. In the following, $N_z = 66$, i.e. we consider Zernike polynomials up to the tenth radial order. Moreover, $\zeta_0^0, \zeta_1^{-1}, \zeta_1^1 = 0$, i.e. the piston and tip-tilt modes are not included. The remaining 63 coefficients are vectorized after ordering them by increasing radial order (Noll's sequential index) into $\boldsymbol{\zeta}$. The standard deviation of the normal distribution generating the k-th index ζ_k is computed as $c_l \exp(k)$, where c_l is a scaling factor to control the amplitude of the aberration. An example of such a generated wavefront is shown in Figure 2.2a.

2.3.2. GENERATION OF HIGH-ORDER ABERRATIONS

For the generation of aberrations with higher spatial frequencies, a similar experiment as in [10] is repeated for a high-order DM, having $N_m = 952$ actuators (Boston Micromachines KiloDM [16]). The control signal to each of the actuators u_i is collected into the vector $\mathbf{u} \in \mathbb{R}^{N_m}$. Because of the large number of actuators, an accurate Zernike representation of the wavefront would require too many parameters. Therefore, the DM infulence matrix $H \in \mathbb{R}^{N_s \times N_m}$ is identified such that it satisfies the relation $\mathbf{s} = H\mathbf{u}$, where $\mathbf{s} \in \mathbb{R}^{N_s}$ contains all the local slopes in the wavefront measured with a high-resolution Shack-Hartmann wavefront sensor ($N_s = 42632$). For the identification of the matrix H, a set of 2000 random vectors $\tilde{\mathbf{u}}_1, \ldots, \tilde{\mathbf{u}}_{2000}$ are drawn from a normal distribution, and corresponding measurements $\tilde{\mathbf{s}}_1, \ldots, \tilde{\mathbf{s}}_{2000}$ are collected. The matrix H is identified enforcing a sparsity pattern in the matrix, such that the number of non-zero elements is 14.01% of the total number of elements. The accuracy of the identification is very sensitive to the measurement noise of the sensor and optical misalignments in the experimental setup. After a careful calibration, the identification of H resulted into an average variance accounted for (VAF) [17], defined as

$$VAF = \left(1 - \frac{\sum_{i=1}^{2000} \|\tilde{\mathbf{s}}_i - H\tilde{\mathbf{u}}_i\|_2^2}{\sum_{i=1}^{2000} \|\tilde{\mathbf{s}}_i\|_2^2}\right) \cdot 100\% \tag{2.19}$$

of 84.31%. A set of sensor measurements $\mathbf{s}_i$ is simulated using random input vectors $\mathbf{u}_i$ drawn from a normal distribution, such that $\mathbf{s}_i = c_h H\mathbf{u}_i$, c_h being a scaling parameter

to control the phase amplitude. The corresponding wavefront Φ_i, sampled on a regular $N_p \times N_p$ grid, is reconstructed from $\mathbf{s}_i$ using the method described in [18]. The resolution N_p is limited by the resolution of the Shack-Hartmann sensor at $N_p \leq 146$. $N_p = 64$ is used to simulate the aberration unless mentioned otherwise. A square of $N_p \times N_p$ is cut from the centre of the original 146×146 image. An example of a high-order wavefront aberration is shown in Figure 2.2b.

2.3.3. APPROXIMATING THE GENERALIZED PUPIL FUNCTION

To quantify the theoretical accuracy for each basis to fit the GPF, the least-squares error approximating a given GPF is considered. The aberration Φ is generated as discussed in Sections 2.3.1 or 2.3.2 on an $N_p \times N_p$ grid. Similar to (2.13), a sampled representation of the true GPF can be defined as a vector $\mathbf{p} \in \mathbb{C}^{N_p^2}$. By solving the following complex least-squares problem

$$\hat{\boldsymbol{\alpha}}_{LS} = \arg\min_{\boldsymbol{\alpha} \in \mathbb{C}^{N_\alpha}} \|\mathbf{p} - B\boldsymbol{\alpha}\|_2^2, \tag{2.20}$$

a theoretical best estimate of the GPF using the defined basis can be computed as $\hat{\mathbf{p}}_{LS} = B\hat{\boldsymbol{\alpha}}_{LS}$. The normalized real-valued root mean square (RMS) of the complex-valued approximation error $\mathbf{p} - \hat{\mathbf{p}}_{LS}$, denoted by $\varepsilon_{p,LS}$, defines the measure of its ability to fit the GPF, i.e.

$$\varepsilon_{p,LS} = \frac{\|\mathbf{p} - \hat{\mathbf{p}}_{LS}\|_2}{\|\mathbf{p}\|_2}. \tag{2.21}$$

Since we are mainly interested in finding the correct phase Φ, we define the vectorized phase as $\boldsymbol{\phi} \in \mathbb{R}^{N_p^2}$ and the phase corresponding to the estimated GPF as $\hat{\boldsymbol{\phi}}_{LS} \in \mathbb{R}^{N_p^2}$, such that the normalized RMS phase error is:

$$\varepsilon_{\phi,LS} = \frac{\|\boldsymbol{\phi} - \hat{\boldsymbol{\phi}}_{LS}\|_2}{\|\boldsymbol{\phi}\|_2}. \tag{2.22}$$

Because of the dependence on the number of GRBF N_α and the stochastic nature of the aberration, a Monte Carlo experiment is performed for various values of N_α by using 100 draws of the simulated GPF.

Besides using this experiment to show the theoretical accuracy to fit the GPF, the method in this paragraph is used to tune the GRBF hyper parameters in the next section. In principle, the RMS error of the PSF fit obtained by solving the phase retrieval problem can also be used. However, since this is much more computationally demanding than computing the least-squares fit of the GPF directly, it would be too time consuming and is therefore not considered.

2.3.4. PHASE RETRIEVAL EXPERIMENT

The phase retrieval problem defined in (2.17) is solved using the COPR algorithm [8]. First, the PSF data is simulated by taking the 2D-FFT of the GPF corresponding to the simulated aberration Φ as discussed in Section 2.2 for $D = 2$. Four diversity images, at $f_1 = 0$, $f_2 = -1$, $f_3 = 2$ and $f_4 = -3$ rad, are computed and vectorized into $\mathbf{y}_i$, $i = 1, 2, 3, 4$. A Monte Carlo experiment solving the PR problem for 25 different aberration realizations is performed for a certain combination of N_α and aberration type (low-/high-order).

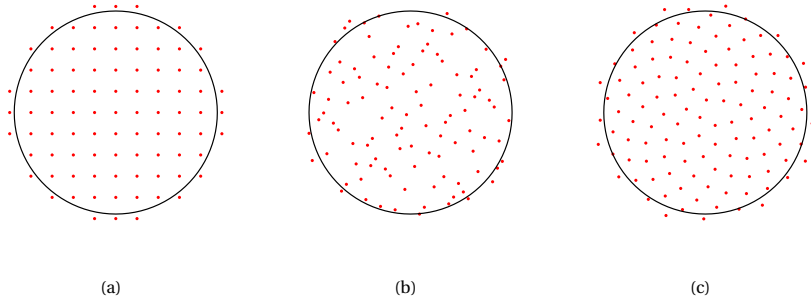

(a) (b) (c)

Figure 2.3: Examples of node distributions on a 2D grid for a unit disk pupil aperture: (a) Rectangular, (b) Halton and (c) Fibonacci.

From the solution of the phase retrieval problem, we obtain a solution $\hat{\boldsymbol{\alpha}}$. An estimate of the PSF and GPF is obtained via $\hat{\mathbf{y}}_i = C_i\hat{\boldsymbol{\alpha}}$ and $\hat{\mathbf{p}} = B\hat{\boldsymbol{\alpha}}$ respectively. The normalized RMSE of the PSF and phase will be used as a scalar quantity to express the accuracy. One major difficulty in comparing the phase is caused by the fact that the phase retrieval solution provides an estimate up to a constant offset (piston) and each pixel is wrapped on the range $[-\pi,\pi]$. This is solved by extracting the phase of the estimated GPF, unwrapping it using a two-dimensional phase unwrapping algorithm [19], and removing the piston. Similar to (2.22), the real-valued normalized RMSE of the phase is defined as:

$$\varepsilon_\phi = \frac{\|\boldsymbol{\phi} - \hat{\boldsymbol{\phi}}\|_2}{\|\boldsymbol{\phi}\|_2}. \tag{2.23}$$

The cost function in (2.17) minimizes the PSF fitting error rather than the GPF. A measure representing the fit of the PSF is defined in a similar way:

$$\varepsilon_y = \frac{\sum_{i=1}^{N_f} \|\mathbf{y}_i - \hat{\mathbf{y}}_i\|_2}{\sum_{i=1}^{N_f} \|\mathbf{y}_i\|_2}. \tag{2.24}$$

The results of this experiment are discussed in Section 2.5.

2.4. FITTING ACCURACY OF GRBF

The increased flexibility of the GRBF follows directly from the introduced freedom in terms of its hyper-parameters. Each single GRBF has two parameters: its centre location pair (ρ_k,θ_k) and shape parameter λ_k. Together they define the shape and location of the GRBF in the pupil plane. If they were to be chosen independent from each other, they would introduce $2N_\alpha$ hyper-parameters to the phase retrieval problem. Estimating them is a highly non-linear problem usually solved by cross-validation [13]. In this section, by using their physical interpretation in the imaging application, we propose to reduce the number of parameters to one single shape parameter λ and a predefined node distribution.

2.4.1. NODE DISTRIBUTION

Instead of choosing the centre (ϱ_k, ϑ_k) of each basis function separately, a number of fixed configurations are considered. In this way, the centres are no longer a hyper-parameter to be determined. Since we assume to have no specific *a priori* knowledge of the GPF, we are looking for a general distribution that is able to fit any generic GPF realization. There are many regular and quasi-random grids that can work as a suitable node distribution. Examples are a rectangular grid with equally spaced points, a Halton-points-based grid generated from quasi-random number sequence [20] and a planar Fibonacci grid defined using a spiral represented in polar coordinates, i.e. for the k^{th} point [14]:

$$\varrho_k = \varrho_0 \sqrt{k - 1/2}, \quad \vartheta_k = 2\pi k/\varphi, \tag{2.25}$$

where ϱ_0 is an arbitrary scale factor and $\varphi = (1+\sqrt{5})/2$ is the Golden ratio. These distributions are visualized in Fig 2.3. All grids are defined over an area slightly larger than the unit disk (a disk with radius 1.05) to deal with the Gibbs phenomenon [13].

The Fibonacci grid has proven to be a competitive and robust choice when the shape parameter is optimally chosen [14]. For completeness, the simulations in this chapter have been implemented for all three grids in Figure 2.3. This showed a performance that is similar for all grids, but slightly in favor of the Fibonacci configuration. Therefore, only the Fibonacci configuration is included in the results.

2.4.2. SHAPE PARAMETER

The choice of shape parameter is significant, as it affects numerical stability, accuracy of fit and speed of convergence. The practical design of the shape parameter is data dependent, in that it depends on the variance of the wavefront aberration and its spatial frequency content. As the data of the GPF is not available beforehand, it is desirable to find a systematic empirical approach of shape parameter selection. To reduce the number of hyper-parameters, a single constant λ is assumed for each GRBF. Moreover, especially for the regular grids (rectangular and Fibonacci), a constant λ is a reasonable assumption when there is no prior knowledge of the GPF.

To determine the value of the parameter λ, we compare the RMS of the approximation error with the GRBF basis for different values of λ with the method discussed in Section 2.3.3. First of all, since the selection of the hyper-parameter depends on the chosen node distribution and the total number of nodes, the influence of λ is shown for different values of N_α. Moreover, as it is shown to depend on the type of aberration, the test is repeated for both the low-order and high-order aberrations discussed in Sections 2.3.1 and 2.3.2. Figure 2.4 shows $\varepsilon_{p,LS}$, as defined in (2.21), for various combinations of λ and N_α on the Fibonacci grid. It is clear that both for the low-order and high-order aberration, the trend is very similar. Both start with a steep increase in performance by increasing λ up to a value that is depending on N_α. At a certain point, which is denoted by λ^*, the steep slope turns into a more constant and smoother curve. This point, indicated by the asterisks in Figure 2.4, is the same for both the low-order and high-order aberrations and seems to be dependent on N_α only. However, where for the low-order aberration $\varepsilon_{p,LS}$ starts to increase immediately, it still slightly decreases for the high-order aberration. As can be seen in Figure 2.4, the optimal value of λ, λ_{opt}, is in the range of 1 to 10 for the low-order and between 10 and 40 for the high-order aberrations.

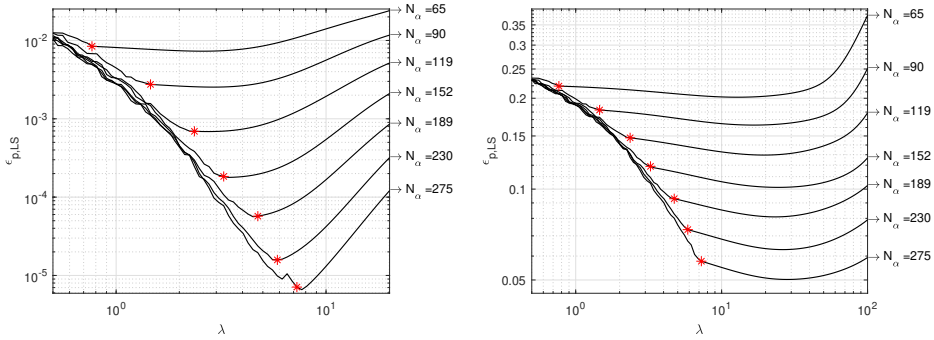

(a) Low-order aberration

(b) High-order aberration

Figure 2.4: Influence of λ on the mean value of $\varepsilon_{p,LS}$ in a Monte Carlo simulation. The same simulation is performed on both low- and high-order aberration data discussed in Sections 2.3.1 and 2.3.2 for $N_p = 64$ on a circular aperture with a radius of 1.

N_α	GRBF-LO	ENZ-LO	GRBF-HO	ENZ-HO
65	$6.56 \cdot 10^{-3}$	$9.46 \cdot 10^{-3}$	$5.16 \cdot 10^{-1}$	$5.74 \cdot 10^{-1}$
90	$2.23 \cdot 10^{-3}$	$3.60 \cdot 10^{-3}$	$4.09 \cdot 10^{-1}$	$4.83 \cdot 10^{-1}$
119	$5.82 \cdot 10^{-4}$	$8.94 \cdot 10^{-4}$	$3.18 \cdot 10^{-1}$	$3.98 \cdot 10^{-1}$
152	$1.48 \cdot 10^{-4}$	$2.90 \cdot 10^{-4}$	$2.42 \cdot 10^{-1}$	$3.21 \cdot 10^{-1}$
189	$5.04 \cdot 10^{-5}$	$1.01 \cdot 10^{-4}$	$1.89 \cdot 10^{-1}$	$2.58 \cdot 10^{-1}$
230	$1.42 \cdot 10^{-5}$	$2.98 \cdot 10^{-5}$	$1.42 \cdot 10^{-1}$	$2.07 \cdot 10^{-1}$
275	$5.84 \cdot 10^{-6}$	$7.06 \cdot 10^{-6}$	$1.10 \cdot 10^{-1}$	$1.65 \cdot 10^{-1}$

Table 2.1: Mean values of $\varepsilon_{\phi,LS}$ using GRBFs and ENZ polynomials in the Monte Carlo simulation. For the GRBFs, $\lambda = \lambda_{opt}$ found using a grid search minimizing the GPF error $\varepsilon_{p,LS}$.

In practice, the nature of the GPF is unknown and one does not have a set of GPFs with the same statistical properties as the one to be estimated. This makes the optimal value of λ more difficult to find. However, λ^* can be used as a lower-bound to the selection of λ and it can be derived from knowing the GRBF centre locations only. It is shown that $\epsilon_{p,LS}$ is not very sensitive for choosing λ larger than λ^*. Therefore, it is a safe choice to select $\lambda > \lambda^*$, depending on the desired smoothness of the reconstruction of the wavefront.

As pointed out in Section 2.2, the basis can become severely ill-conditioned when $\lambda \to 0$. This should be kept in mind when selecting the value of λ when the number of basis function is small. In this case, it is advised to choose $\lambda \gg \lambda^*$ to avoid problems while solving the phase retrieval problem. One can use the RBF-QR algorithm [15] to improve the conditioning and transform the obtained coefficients back into the original basis. As the focus of this chapter is on capturing high-order aberrations with a relatively large amount of basis functions, this has not been implemented. The value of λ during the phase retrieval simulations was increased manually when the found λ_{opt} caused problems regarding ill-conditioning.

2.4.3. COMPARISON TO ENZ

After λ_{opt} is selected for the chosen node distribution, the fitting accuracy can be compared to that of ENZ polynomials. The mean phase approximation errors $\varepsilon_{\phi,LS}$ for both the low-order and high-order aberrations are summarized in Table 2.1. From Table 2.1, we can conclude that the mean values of $\varepsilon_{\phi,LS}$ indicate a higher fitting accuracy of GRBFs over ENZ polynomials on average. It should be mentioned that the variance over the Monte Carlo draws was found to be approximately within 10% of the mean values for high-order aberrations, but was much more significant for low-order aberrations with values of the same order of magnitude as its mean. A more comprehensive analysis discussing the importance of this large variance is included in Section 2.5. Moreover, the final value of $\varepsilon_{\phi,LS}$ for the high-order aberration is still significant with a minimum of 0.11 for $N_\alpha = 275$. This should be kept in mind when performing the phase retrieval simulations. The performance shown here gives a theoretical minimum of the error for each specific set of basis functions. Because the phase retrieval simulation will use the RMS of the phase error (ε_ϕ in (2.23)) as a measure, we have only presented the theoretical minimal phase errors $\varepsilon_{\phi,LS}$ is this section. The obtained errors from the phase retrieval simulation will be compared to the values in this table to validate if the algorithm has converged to the optimal solution. A similar table can be made for $\varepsilon_{p,LS}$ but is not included here since it shows an equivalent trend.

2.5. PHASE RETRIEVAL SIMULATION RESULTS

As discussed in Section 2.3, a simulation is performed to analyze the performance of the different basis functions to the phase retrieval problem. In this section, a number of cases will be considered that demonstrate the advantages of using GRBFs in modal-based phase retrieval. For each combination of N_α and aberration type, an experiment as described in Section 2.3.4 is performed to find the value of λ that gives the best fit in the least-squares sense. The scaling constants c_l and c_h introduced in Section 2.3.1 and 2.3.2 are chosen such that the average RMS-value of Φ in the Monte Carlo simulation $RMS(\Phi) \approx 0.75$ for both low- and high-order aberrations. The performance of the method for higher values of $RMS(\Phi)$ will be shortly discussed in the following paragraph.

2.5.1. LOW- AND HIGH-ORDER ABERRATIONS

To show the performance of the GRBF for aberrations containing different spatial frequencies, the phase retrieval problem is solved for both the low- and high-order aberrations. The simulation results when considering only low-order aberrations are visualized in Figure 2.5a and 2.5c. A clear decrease of the normalized RMSE is visible for both the PSF and phase as the number of used basis functions increase. Both the ENZ polynomials and GRBFs obtain a very accurate fit, approaching the theoretical optimum of Table 2.1. The variance over the multiple draws in the Monte Carlo simulation is relatively large, such that both methods lead to a roughly equivalent performance.

The phase retrieval simulation results for the high-order aberrations are shown in Figure 2.5b and 2.5d. The GRBFs still approximate the theoretical value of Table 2.1 quite closely. On the other hand, the ENZ polynomials fit starts to deviate more from the theoretical minimum when more basis functions are considered. This phenomenon together

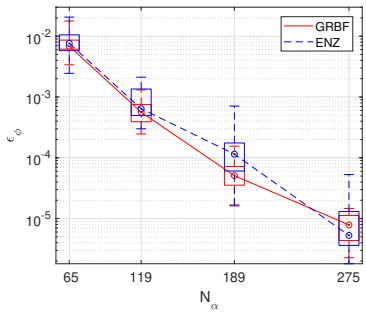

(a) ε_ϕ for low-order aberrations

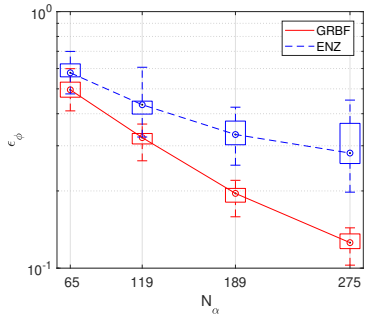

(b) ε_ϕ for high-order aberrations

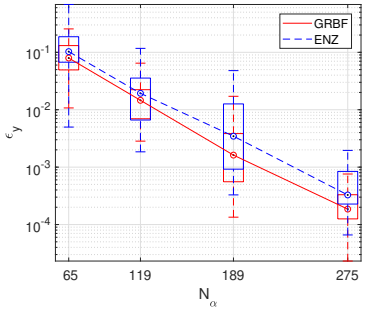

(c) ε_y for low-order aberrations

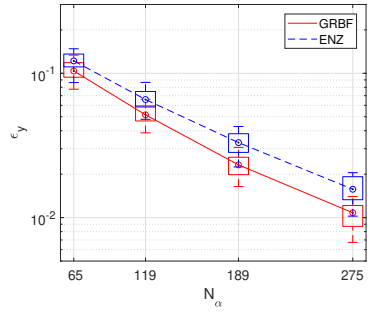

(d) ε_y for high-order aberrations

Figure 2.5: Comparison of the results of the phase retrieval simulation between low- and high-order aberrations for varying number of basis functions N_α. The boxplots show the normalized RMSE ε_y and ε_ϕ (see (2.23) and (2.24)) for a circular pupil with $N_p = 64$ and $RMS(\Phi) \approx 0.75$ rad. The boxes indicate the 25th and 75th percentile of the results in the Monte Carlo simulation. Lines are drawn through the medians of the data. Data outliers due to remaining phase ambiguities are discarded.

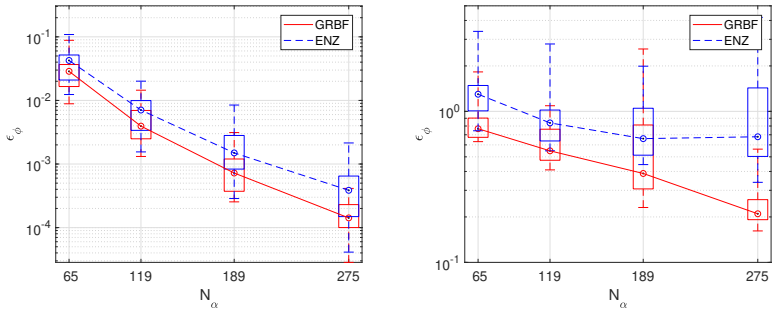

(a) ε_ϕ for low-order aberrations

(b) ε_ϕ for high-order aberrations

Figure 2.6: Phase retrieval results for low-order and high-order aberrations for for $RMS(\Phi) \approx 1.5$ rad. The presentation of the results is similar to Fig. 2.5.

with the much less significant variance than in the low-order aberration case make the differences appear much clearer. The decrease in performance from the theoretical minimum indicates that the phase retrieval algorithm is less able to converge to the optimal solution when ENZ polynomials are used.

To investigate the performance of the method for higher phase amplitudes, the phase retrieval simulations for both the low-order and high-order aberrations are repeated for a higher value of $RMS(\Phi)$. Figure 2.6 shows the normalized RMS phase error ε_ϕ for $RMS(\Phi) \approx 1.5$ rad. All other conditions are kept the same as in the experiment above such that they can be compared to Figure 2.5a and 2.5b, where $RMS(\Phi) \approx 0.75$. Both errors increase when $RMS(\Phi)$ increases. The same improving trend in the performance is visible when using more basis functions.

From this analysis, the GRBFs appear most beneficial when approximating aberrations containing high spatial frequencies with a relatively large amount of basis functions. An example of such an approximation is shown in Figure 2.7 for $N_p = 128$ and $N_\alpha = 377$. One thing that stands out when comparing the estimations with GRBFs and ENZ polynomials are the ringing artifacts that appear when using ENZ. Since these rings are a consequence of the phase retrieval solution and do not appear in the least-squares approximation, they cause a gap between the theoretical value of Table 2.1 and the obtained phase retrieval solution when using ENZ polynomials.

2.5.2. NON-CIRCULAR APERTURE

An important property of the GRBFs is its independence on the pupil geometry. Since each basis function can be centered around an arbitrary location on the pupil, it is possible to concentrate the information on any specific shape. In contrast, ENZ polynomials are defined on the unit circle only. Although the Zernike theory can be adapted for other pupil geometries, it requires complex theoretical reformulation (see, e.g. [12]). The GRBFs provide a much simpler implementation, in which the user can locate the basis functions. As a result, the basis can be easily adapted to any arbitrary shape without needing any complex theory.

To demonstrate the advantage of this locality, an extreme case is considered in which

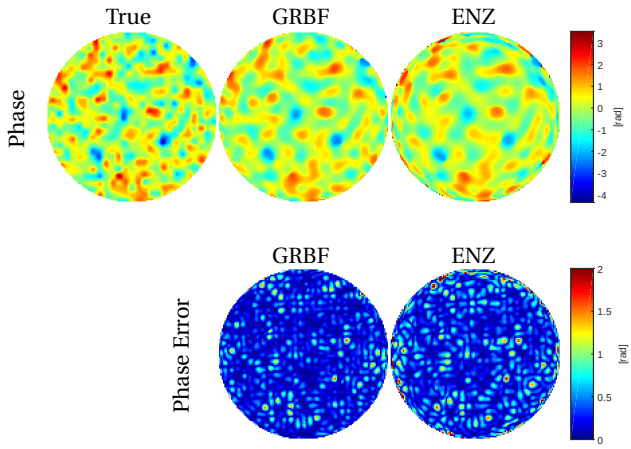

Figure 2.7: An example of the retrieved phase for a high-order aberration, $N_p = 128$ and $N_\alpha = 377$. From left to right, the first row shows the true phase aberration, the retrieved phase estimate using GRBFs and the retrieved estimate using ENZ polynomials. The second row shows the errors for GRBFs ($\varepsilon_\phi = 0.42$) and ENZ polynomials ($\varepsilon_\phi = 0.57$) respectively. The figures are truncated to the color scale shown.

an annular pupil is defined with unity outer radius and an inner radius of 0.7. The centers of the GRBFs are located on a ring with inner radius 0.65 and outer radius 1.05 following the Fibonacci node distribution. Compared to the circular aperture, the number of non-zero pixels in the GPF has decreased. Therefore, it would be expected that when the same number of basis functions are considered, the normalized error should decrease. The phase retrieval results for this annular aperture are summarized in Fig. 2.8, showing that the difference in performance between GRBF and ENZ is more significant than in the same situation with the circular aperture (recall Fig. 2.5). The normalized error for the GRBFs has indeed decreased compared to the circular aperture. Because the ENZ polynomials have not been redefined on the new pupil, the error for the ENZ basis has increased significantly. This demonstrates the advantage that GRBFs have on non-circular apertures. An explanation for this decrease in performance when using ENZ polynomials becomes apparent when looking at an example of the retrieved phase in Fig. 2.9. Note how the estimate using GRBF is more detailed, but the estimate corresponding to the ENZ polynomial basis shows that the oscillations around the edges have become more significant due to the thin aperture shape.

2.5.3. GAUSSIAN MEASUREMENT NOISE

Finally, zero-mean white Gaussian noise is added to the simulation measurements $\mathbf{y}_i$ to consider the robustness of the estimation with respect to noise. Since the intensity measurements are by definition positive, negative values in the simulated measurement are truncated to zero. For the conciseness of this chapter, a single case regarding a low-order aberration is considered on a circular aperture, and $N_\alpha = 65$ basis functions are used. The results are shown in Fig. 2.10. The noise is sampled from a single zero-mean

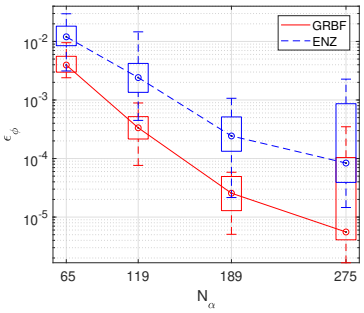

(a) ε_ϕ for low-order aberrations

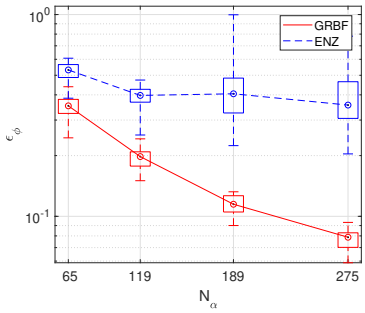

(b) ε_ϕ for high-order aberrations

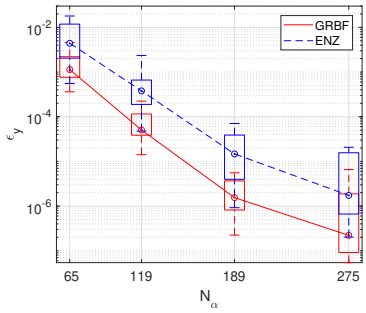

(c) ε_y for low-order aberrations

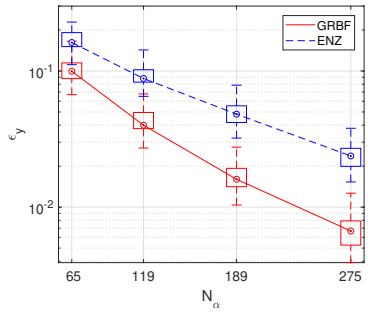

(d) ε_y for high-order aberrations

Figure 2.8: Comparison of the results of the phase retrieval simulation between low- and high-order aberrations for varying number of basis functions N_α. The boxplots show the normalized RMSE ε_y and ε_ϕ (see (2.23) and (2.24)) for an annular pupil with $N_p = 64$ and $RMS(\Phi) \approx 0.75$ rad. The boxes indicate the 25th and 75th percentile of the results in the Monte Carlo simulation. Lines are drawn through the medians of the data. Data outliers due to remaining phase ambiguities are discarded.

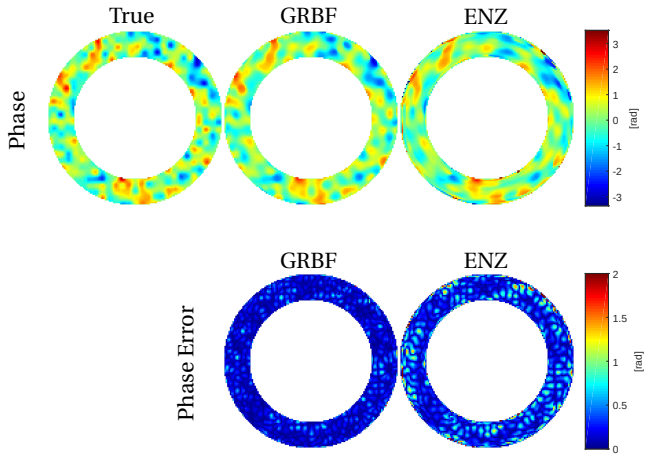

Figure 2.9: An example of the retrieved phase for a high-order aberration, $N_p = 128$ and $N_\alpha = 377$. From left to right, the first row shows the true phase aberration, the retrieved phase estimate using GRBFs and the retrieved estimate using ENZ polynomials. The second row shows the errors for GRBFs ($\varepsilon_\phi = 0.27$) and ENZ polynomials ($\varepsilon_\phi = 0.68$) respectively. The figures are truncated to the color scale shown

Gaussian distribution and the SNR is defined with respect to the average power of the image $\mathbf{y}_i$. The noise affects the estimate for both the ENZ and GRBF basis similarly for higher SNR. For an SNR of $5-10$ dB, the ENZ polynomials give a normalized error higher than 1, implying a completely inaccurate estimate.

2.6. CONCLUSION

The problem of reconstructing phase aberrations using a modal approach for optimization-based phase retrieval algorithms has been considered in this chapter. The otherwise too computationally demanding optimization-based algorithms [5, 8] can be implemented on a standard desktop computer in this modal-based framework [10]. In this chapter, the application of GRBFs to model the GPF has been explored as an alternative to the existing ENZ polynomials [10, 11]. Because of its computational efficiency, the COPR algorithm [8] is used to solve the PR problem. One important advantage of GRBFs is the increased flexibility introduced by user-defined hyper-parameters determining the location and shape of each basis function. The number of hyper-parameters are reduced to a single parameter describing the size of a single GRBF by assuming a predefined distribution of the centres. Guidelines have been proposed to find the hyper-parameter that leads to the best fit. It was shown that the obtained basis using GRBFs is better able to approximate the GPF than ENZ polynomials. Moreover, the solution to the PR problem has been considered for both the GRBF and ENZ polynomial basis. Simulations have shown that GRBFs are significantly better to approximate aberrations that contain higher spatial frequencies. The increased flexibility of GRBFs has been demonstrated by solving the phase retrieval problem for an annular pupil. Finally, also the robustness to

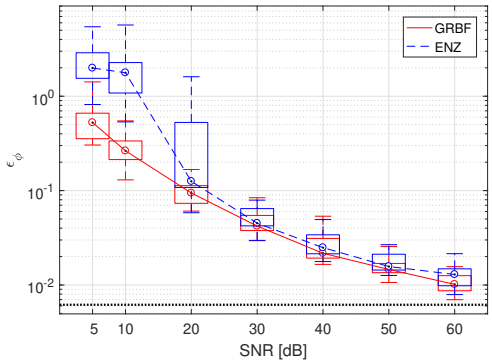

Figure 2.10: Normalized RMS phase error ε_ϕ (defined in (2.23)) as a function of the SNR for low-order aberrations with an average $RMS(\Phi) \approx 0.75$, using $N_\alpha = 65$ basis functions. The black dotted line shows the error without noise.

Gaussian measurement noise was in favor of GRBFs, showing a lower noise sensitivity.

REFERENCES

[1] Y. Shechtman, Y. C. Eldar, O. Cohen, H. N. Chapman, J. Miao, and M. Segev, *Phase retrieval with application to optical imaging: a contemporary overview,* IEEE signal processing magazine **32**, 87 (2015).

[2] D. R. Luke, J. V. Burke, and R. G. Lyon, *Optical wavefront reconstruction: Theory and numerical methods,* SIAM review **44**, 169 (2002).

[3] R. W. Gerchberg, *A practical algorithm for the determination of the phase from image and diffraction plane pictures,* Optik **35**, 237 (1972).

[4] J. R. Fienup, *Reconstruction of an object from the modulus of its Fourier transform,* Optics Letters **3**, 27 (1978).

[5] E. J. Candes, Y. C. Eldar, T. Strohmer, and V. Voroninski, *Phase retrieval via matrix completion,* SIAM review **57**, 225 (2015).

[6] Y. Chen and E. Candes, *Solving random quadratic systems of equations is nearly as easy as solving linear systems,* in *Advances in Neural Information Processing Systems* (2015) pp. 739–747.

[7] I. Waldspurger, A. d'Aspremont, and S. Mallat, *Phase recovery, MaxCut and complex semidefinite programming,* Mathematical Programming **149**, 47 (2015).

[8] R. Doelman, H. T. Nguyen, and M. Verhaegen, *Solving large-scale general phase retrieval problems via a sequence of convex relaxations,* arXiv:1803.02652 (2018).

[9] H. H. Bauschke, P. L. Combettes, and D. R. Luke, *Phase retrieval, error reduction algorithm, and Fienup variants: a view from convex optimization,* Journal of the Optical Society of America A **19**, 1334 (2002).

[10] J. Antonello and M. Verhaegen, *Modal-based phase retrieval for adaptive optics,* Journal of the Optical Society of America A **32**, 1160 (2015).

[11] A. J. Janssen, *Extended Nijboer–Zernike approach for the computation of optical point-spread functions,* Journal of the Optical Society of America A **19**, 849 (2002).

[12] S. Van Haver, *The extended Nijboer-Zernike diffraction theory and its applications,* Ph.D. thesis, Delft University of Technology (2010).

[13] A. Martinez-Finkelshtein, D. Ramos-Lopez, and D. Iskander, *Computation of 2D Fourier transforms and diffraction integrals using Gaussian radial basis functions,* Applied and Computational Harmonic Analysis **43**, 424 (2017).

[14] M. Maksimovic, *Optical design and tolerancing of freeform surfaces using anisotropic radial basis functions,* Optical Engineering **55**, 071203 (2016).

[15] B. Fornberg, E. Larsson, and N. Flyer, *Stable computations with gaussian radial basis functions,* SIAM Journal on Scientific Computing **33**, 869 (2011).

[16] Boston Micromachines Corporation, http://www.bmc.bostonmicromachines.com/pdf/Kilo-DM.pdf, accessed: 2018-03-05.

[17] M. Verhaegen and V. Verdult, *Filtering and system identification: a least squares approach* (Cambridge university press, 2007).

[18] F. Roddier and C. Roddier, *Wavefront reconstruction using iterative Fourier transforms,* Applied Optics **30**, 1325 (1991).

[19] M. A. Herráez, D. R. Burton, M. J. Lalor, and M. A. Gdeisat, *Fast two-dimensional phase-unwrapping algorithm based on sorting by reliability following a noncontinuous path,* Applied Optics **41**, 7437 (2002).

[20] L. Kocis and W. J. Whiten, *Computational investigations of low-discrepancy sequences,* ACM Transactions on Mathematical Software (TOMS) **23**, 266 (1997).

3

PHASE RETRIEVAL OF LARGE-SCALE TIME-VARYING ABERRATIONS USING A NON-LINEAR KALMAN FILTERING FRAMEWORK

This chapter presents a computationally efficient framework in which a single focal-plane image is used to obtain a high-resolution reconstruction of dynamic aberrations. Assuming small phase aberrations, a non-linear Kalman filter implementation is developed whose computational complexity scales close to linearly with the number of pixels of the focal-plane camera. The performance of the method is tested in a simulation of an adaptive optics system, where the small-phase assumption is enforced by considering a closed-loop system that uses a low-resolution wavefront sensor to control a deformable mirror. The results confirm the computational efficiency of the algorithm and show a large robustness against noise and model uncertainties.

The contents of this chapter have been published in Piscaer, P., Soloviev, O., Verhaegen, M. *Phase retrieval of large-scale time-varying aberrations using a non-linear Kalman filtering framework*, JOSA A 38, 25 (2021).

3.1. INTRODUCTION

Adaptive optics (AO) systems correct in real-time for phase aberrations in optical systems. A deformable mirror (DM) is used to correct for the phase aberrations and counter their effects on the image quality. Often, the light is split between a wavefront sensor (WFS), which measures the phase aberration, and a focal-plane camera, which captures the image of interest. The reason for including a dedicated WFS is that retrieving the aberrations from focal-plane images alone is very challenging, as most methods are based on iterative algorithms, which are difficult to apply in real time for temporally dynamic wavefronts. Despite the challenges, focal-plane wavefront sensing is still an active field, as it simplifies the optical setup and eliminates errors due to non-common path aberrations (NCPAs). Assuming a point source, the focal-plane camera captures the point spread function (PSF). The problem of retrieving the static phase aberrations from the PSF is known as the phase retrieval (PR) problem.

Many PR algorithms have been developed, these can be split into three main classes. The first and still the most commonly used class is based on the alternating projections (AP). The most well-known AP methods include [1, 2], but many more have been developed. See [3] for an overview and [4] for a recent state of the art method. A second class of methods reformulates the PR problem as a convex optimization problem [5, 6]. Despite promising convergence results, these methods are very computationally demanding for larger AO systems. More recently, a third class, which solves the PR problem in its original non-convex framework, has gained attention [7–10]. A problem of this class of methods is the need of an accurate initial guess of the wavefront, usually computed via techniques that require a restrictive measurement setup and many more measurements than unknowns [7, 8].

Another approach to focal-plane wavefront sensing is to assume that the phase to be estimated is small [11] and to apply a linear or quadratic approximation of the PSF. This approach includes methods such as ILPD [12], LIFT [13] and Fast & Furious [14]. These method are restricted to small wavefronts (RMS-value below 0.5 rad [12]). In addition, in [15], the approach was used to estimate dynamic aberrations using a non-linear Kalman filtering (KF) framework.

Where the KF implementation proposed in [15] is unpractical for large-scale applications due to its large computational complexity, this chapter presents a computationally efficient framework in which a single focal-plane image is used to obtain a high-resolution reconstruction of dynamic aberrations. By exploiting special matrix structures and efficient linear algebra operations specific to AO systems, the number of elementary computations scale just more than linearly ($n\log(n)$) with the total number of pixels n of the reconstruction. This computational complexity is of the same order as computationally efficient small-phase methods [14] and much faster than the existing KF-based method [15] (which scales with n^3). The low computational complexity opens up the possibility for real-time large-scale applications.

An additional goal of this chapter is to address the advantages of reformulating the PR problem for dynamic aberrations into a Kalman filtering framework. Due to the similarities between the KF measurement update and the PR problem, the issue of uniqueness of the PR problem becomes issue of observability within the KF framework. Consequently, even when there is no unique solution to the PR problem when using a single image, the

full dynamic system considered by the KF can become observable. In addition, it will be discussed how the KF measurement update can be interpreted as an optimally weighted regularization to the static PR problem.

The KF framework makes the method applicable to cases where the phase aberrations change over time, i.e. dynamic phase aberrations. Moreover, by including the temporal and statistical models of the turbulence and sensors, the KF is known to be robust against modelling errors and measurement noise, making it particularly suitable for dealing with dynamic aberrations and noisy measurements. Small-phase aberrations have also been assumed in other algorithms that aim to estimate temporal dynamic aberrations [15, 16]. Possible applications include estimating NCPAs (which occur in various fields such as astronomy [17, 18] and ophthalmology [19, 20]), wind induced dynamic non-common path vibrations [21] or the low-wind effect [18]. This method could also be used to estimate spatial (rather than temporal) dynamics due to anisoplanatic conditions in astronomy [22], ophthalmology [23] and microscopy [24]. Small-phase aberrations are the typical situation considering a closed-loop AO system [12], making the algorithm well-suited to estimate AO-corrected atmospheric residuals.

The proposed algorithm establishes a generic framework which can be applied provided its requirements are satisfied (small-phase aberrations with continuous dynamic evolution). As an illustration, a simulation of a closed-loop AO system for astronomy using the open-source Matlab software OOMAO [25] is performed, giving a detailed analysis of the robustness of the method against modelling inaccuracies and noise. A simple WFS-based controller compensates for the dominant low-order modes in the wavefront in order to keep the wavefront sufficiently small. It should be stressed that this case study is merely an example and should be considered as an illustration of the performance of the method under varying temporal dynamics, noise conditions, and RMS-values of the aberration.

This chapter is structured as follows. Section 3.2 gives an introduction to modelling AO systems and dynamic aberrations. A computationally efficient representation of the model and its identification procedure is described in Section 3.3. The advantage of using KFs in WFSless AO systems is discussed in Section 3.4. The main contribution of this chapter, an efficient implementation of the KF, is introduced in Section 3.5. Section 3.6 discusses the simulation environment and the results are presented in Section 3.7. Finally, the main conclusions are summarized in Section 3.8. Frequently used symbols are listed in Table 3.1.

3.2. MODELLING THE AO SYSTEM

To provide an illustration of the algorithm's performance, a typical closed-loop AO system for astronomy depicted in Figure 3.1 will be used. This section introduces the components, aberration dynamics and measurement noise models.

3.2.1. OVERVIEW OF THE AO SYSTEM

The effect of the phase aberration on the optical system will be represented in terms of the generalized pupil function (GPF):

$$\mathscr{X}(\rho,\theta) = \mathscr{A}(\rho,\theta)\exp\left(i\Phi(\rho,\theta)\right), \tag{3.1}$$

Table 3.1: A list of frequently used notations and symbols.

c_X	Average number of non-zero elements per row/column of any sparse banded matrix X
m	Number of actuators inside the aperture
$\bar{n},\ n$	Size of grid in pupil plane ($\bar{n}\times\bar{n}$) and number of pixels inside aperture respectively
$\bar{p},\ p$	Size of grid in the image plane ($\bar{p}\times\bar{p}$) and $p=\bar{p}^2$
$\bar{q}$	Size of lenslet grid of the WFS ($\bar{q}\times\bar{q}$)
$\boldsymbol{\phi}(k)$	Aberrated residual wavefront
$\boldsymbol{a}$	Pupil plane amplitude
$\boldsymbol{u}(k)$	DM control signal
$\boldsymbol{v}(k),\ R(k)$	Measurement noise and its covariance matrix
$\boldsymbol{y}(k)$	Point spread function (PSF)
A, Q	Turbulence dynamics model (see (3.10))
$J_\phi,\ \boldsymbol{c}_\phi$	Taylor expansion of $\boldsymbol{y}(k)$ (see (3.20))
$\mathscr{F},\ \mathscr{F}_{vec}$	Zero-padded 2D DFT and $\mathscr{F}_{vec}\{\cdot\} := vec(\mathscr{F}\{\cdot\})$
$\mathscr{J}_\phi, \mathscr{M}, \mathscr{B}$	Efficient operators (see Eqs. (3.21,3.35,3.36))
$\mathscr{N}(\mu, P)$	Gaussian random process (mean μ, covariance P)
$\mathscr{S}_X$	Set of all matrices that satisfy a chosen sparsity pattern for matrix X.

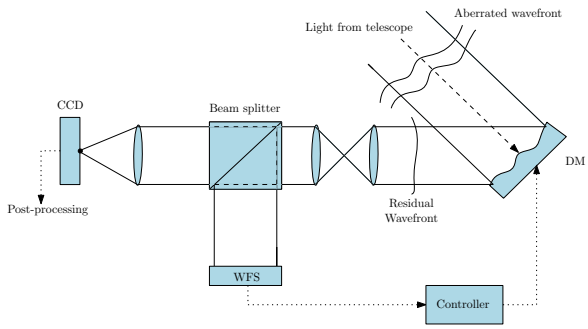

Figure 3.1: Schematic of the classic AO system for astronomy.

where $\rho,\ \theta$ represent the normalized polar coordinates in the pupil plane, and $\mathscr{A}(\rho,\theta)$ and $\Phi(\rho,\theta)$ represent the amplitude apodization function and phase aberration, respectively. Assuming uniform illumination, $\mathscr{A}(\rho,\theta)$ will correspond to the characteristic function with a constant value inside the pupil and zero outside. The image along the optical axis around the focal plane can be expressed in terms of the GPF via the following integral:

$$\mathscr{I}(\zeta,\omega,\delta) = \frac{1}{\pi}\int_0^1\int_0^{2\pi} \exp\left(i\delta\zeta^2\right)\mathscr{X}(\rho,\theta)\exp(2\pi i\zeta\rho\cos(\theta-\omega))\rho d\rho d\theta, \tag{3.2}$$

where $\zeta,\ \omega$ are the normalized polar coordinates in the focal plane and δ represents the position along the optical axis with respect to the focal plane. The PSF corresponding to

the GPF is defined as the intensity of $\mathscr{I}(\zeta,\omega,\delta)$:

$$\mathscr{Y}(\zeta,\omega,\delta) = |\mathscr{I}(\zeta,\omega,\delta)|^2. \tag{3.3}$$

The pupil plane coordinates will be sampled on a regular $\bar{n}\times\bar{n}$ grid of pixels. The discretized GPF, its amplitude and its phase (the wavefront) will be denoted by $X\in\mathbb{C}^{\bar{n}\times\bar{n}}$, $\mathscr{A}\in\mathbb{R}^{\bar{n}\times\bar{n}}$ and $\Phi\in\mathbb{R}^{\bar{n}\times\bar{n}}$ respectively, related via

$$X = \mathscr{A}\odot\exp i\Phi, \tag{3.4}$$

where $\odot$ represents an element-wise product of two vectors or matrices. Often, a vectorized representation will be used in which only the pixels inside the aperture, i.e. the non-zero elements in $\mathscr{A}$, will be considered:

$$\boldsymbol{x} = \boldsymbol{a}\odot\exp i\boldsymbol{\phi}, \tag{3.5}$$

so that $\boldsymbol{a}\in\mathbb{R}^n$, $\boldsymbol{x}\in\mathbb{C}^n$ and $\boldsymbol{\phi}\in\mathbb{R}^n$. Moreover, due to the circular aperture, it can be concluded that $n<\bar{n}^2$.

Similarly, the image plane coordinates are sampled on a $\bar{p}\times\bar{p}$ grid and the PSF will be denoted by $Y\in\mathbb{R}^{\bar{p}\times\bar{p}}$. A discrete adaptation of (3.2) becomes the two-dimensional discrete Fourier transform (DFT) denoted by $\mathscr{F}\{\cdot\}$:

$$Y = |\mathscr{F}\{X\}|^2. \tag{3.6}$$

To obtain a Nyquist sampled measurement, it is necessary for simulation purposes that the matrix $X\in\mathbb{C}^{\bar{n}\times\bar{n}}$ is padded with zeros to the dimension of $\bar{p}\times\bar{p}$, where $\bar{p}=2\bar{n}$. A vectorized representation of (3.6) is defined by

$$\boldsymbol{y} = |\mathscr{F}_{vec}\{\boldsymbol{x}\}|^2, \tag{3.7}$$

where $\mathscr{F}_{vec}\{\cdot\} := \mathrm{vec}(\mathscr{F}\{\cdot\})$ and $\boldsymbol{y}\in\mathbb{R}^p$: $\boldsymbol{y} := \mathrm{vec}(Y)$ such that $p=\bar{p}^2$, with $\mathrm{vec}(\cdot)$ representing a vectorization of a matrix.

The WFS is assumed to have a square grid of $\bar{q}\times\bar{q}$ lenslets. Measurements from lenslets that do not collect enough light due to their position outside the aperture will be discarded. The effect of the DM on the wavefront is modelled by its influence functions. The actuators are placed such that their centers lie on a $(\bar{q}+1)\times(\bar{q}+1)$ grid located at the corners of the WFS lenslet subapertures (known as Fried geometry). Actuators outside of the aperture will be discarded, hence the number of active actuators $m<(\bar{q}+1)^2$. The wavefront correction by the DM will be denoted by $\Phi_{dm}\in\mathbb{R}^{\bar{n}\times\bar{n}}$, and it is defined as

$$\Phi_{dm} = \sum_{\ell=1}^{m} B_\ell u_\ell, \tag{3.8}$$

where $B_\ell\in\mathbb{R}^{\bar{n}\times\bar{n}}$ represents the DM influence functions. The control commands $u_\ell\in\mathbb{R}$, $\ell=1,\ldots,m$ are stored in a vector $\boldsymbol{u}\in\mathbb{R}^m$. A vectorized formulation of Φ_{dm} is represented by $\boldsymbol{\phi}_{dm}\in\mathbb{R}^n$: $\boldsymbol{\phi}_{dm} := vec(\Phi_{dm})$, and

$$\boldsymbol{\phi}_{dm} = B\boldsymbol{u}, \tag{3.9}$$

such that each column ℓ of $B\in\mathbb{R}^{n\times m}$ is equal to $vec(B_\ell)$.

3.2.2. DYNAMIC ABERRATION MODEL

In astronomy, the phase aberrations are caused by turbulence in the Earth's atmosphere. Since atmospheric turbulence is a well-studied source of dynamic aberrations, it is one of the main reasons for choosing the astronomy example to illustrate the algorithm's performance. The temporal dynamics are usually modelled by assuming Taylor's frozen turbulence assumption, where the atmosphere is modelled by multiple layers each moving in a constant direction and speed. The layer's combined influence on the wavefront is denoted by $\boldsymbol{\phi}_t \in \mathbb{R}^n$. The temporal dynamics of $\boldsymbol{\phi}_t$ is estimated by a Vector Auto-Regressive (VAR) model of order one, i.e.,

$$\boldsymbol{\phi}_t(k+1) = A\boldsymbol{\phi}_t(k) + \boldsymbol{w}(k), \tag{3.10}$$

with k specifying the time index, $A \in \mathbb{R}^{n\times n}$, and where $\boldsymbol{w}(k) \in \mathbb{R}^n$ is a Gaussian random process with zero mean and covariance matrix $Q \in \mathbb{R}^{n\times n}$, which will be denoted in this chapter as $\boldsymbol{w}(k) \sim \mathcal{N}(0, Q)$, where the symbol $\sim$ declares the statistical distribution of the variable on its left. VAR models have been a popular choice to model aberration dynamics and have been particularly used to model turbulence dynamics [26]. During the simulations, the turbulence will be simulated using OOMAO, so the model (3.10) is not the true model driving the turbulence dynamics. More detailed information in how to obtain the VAR model from data is discussed in Section 3.3.

Closing the loop using the DM model of (3.9), the residual wavefront $\boldsymbol{\phi}(k) \in \mathbb{R}^n$, defined as $\boldsymbol{\phi}(k) = \boldsymbol{\phi}_t(k) - \boldsymbol{\phi}_{dm}(k)$, which combined with (3.10), becomes

$$\boldsymbol{\phi}(k+1) = A\boldsymbol{\phi}(k) - B\boldsymbol{u}(k) + AB\boldsymbol{u}(k-1) + \boldsymbol{w}(k). \tag{3.11}$$

Finally, using $\boldsymbol{\phi}$ as the state and (3.11) as the state update equation, a state-space model [27] can be formulated by including the measured PSF as an output equation:

$$\boldsymbol{y}(k) = |\mathscr{F}_{vec}\left\{\boldsymbol{a} \odot \exp\left(i\boldsymbol{\phi}(k)\right)\right\}|^2 + \boldsymbol{v}(k). \tag{3.12}$$

The measurement noise $\boldsymbol{v}(k)$ is in reality a combination of Guassian read-out noise and Poissonian shot-noise, but will be modelled as a Gaussian process: $\boldsymbol{v}(k) \sim \mathcal{N}(0, R(k))$, this will be motivated in the next subsection.

3.2.3. MEASUREMENT NOISE MODEL

The true measurement noise can be seen as combination of Gaussian read-out noise and Poissonian shot noise, i.e.,

$$\boldsymbol{y} = \boldsymbol{y}_{true} + \boldsymbol{v}_{shot} + \boldsymbol{v}_{read}, \tag{3.13}$$

where $\boldsymbol{y}_{true}$ is the number of photons that would have arrived at each pixel of the camera in the noiseless case. The read-out noise is a zero-mean white Gaussian noise $\boldsymbol{v}_{read} \sim \mathcal{N}(0, \sigma_r^2 I)$. The shot noise is known to be corresponding to a Poisson distribution: $(\boldsymbol{y}_{true} + \boldsymbol{v}_{shot}) \sim Pois(\boldsymbol{y}_{true})$.

By approximating the Poisson distribution by a Gaussian distribution, the use of Kalman filter theory is allowed. An important reason this approximation is adopted is

that the Poisson distribution is known to converge to a Gaussian distribution when y_{true} is large, i.e.,

$$\lim_{y_{true}\to\infty} Pois(y_{true}) = \mathcal{N}(y_{true}, y_{true}), \tag{3.14}$$

where in this case y_{true} represents a single pixel. Consequently, if y_{true} is large,

$$y \approx y_{true} + \tilde{v}_{shot} + v_{read}, \tag{3.15}$$

with $\tilde{v}_{shot} \sim \mathcal{N}(0, y_{true})$ and $v_{read} \sim \mathcal{N}(0, \sigma_r^2)$. Since the read-out and shot noise can be considered to be uncorrelated, the total noise is $v := \tilde{v}_{shot} + v_{read}$, $v \sim \mathcal{N}(0, y_{true} + \sigma_r^2)$. Of course, this remains an approximation, so the robustness of the method against this modelling inaccuracy will be discussed in Section 3.7.

When the approximation of (3.15) is extended to the multivariate case of (3.13), the approximation of the shot noise becomes: $\tilde{\boldsymbol{v}}_{shot}(k) \sim \mathcal{N}(0, \text{diag}(\boldsymbol{y}(k)))$, with diag($\boldsymbol{y}$) a diagonal matrix with the entries of $\boldsymbol{y}$ on its diagonal. The total measurement noise, given by $\boldsymbol{v}(k)$ in (3.12), will be modelled by

$$\boldsymbol{v}(k) \sim \mathcal{N}(0, R(k)), \quad \text{with } R(k) = \sigma_r^2 I + \text{diag}(\boldsymbol{y}(k)). \tag{3.16}$$

In the simulations, the shot noise and read-out noise will be simulated according to their true distributions, and the approximation (3.16) is not used to simulate the noise.

Furthermore, since the number of arriving photons (y_{true}) influences the severity of the noise, the brightness of the point source becomes an important parameter. A commonly used unit for the flux of photons arriving at the telescope is the (Vega) magnitude, β_m. The relation β_m and the photon flux β_f in photons/m^2/s depends on the photometric system:

$$\beta_f = c_\beta 10^{-\frac{2}{5}\beta_m}, \tag{3.17}$$

with constant $c_\beta \approx 8.97 \cdot 10^9$ for the simulations in Section 3.7.

3.3. STRUCTURES AND EFFICIENT COMPUTATIONS IN AO SYSTEMS

This section discusses a number of structures of matrices that appear in the state-space model defined by (3.11) and (3.12). The model structures and efficient operators presented in this section will be used to develop an efficient non-linear Kalman filter implementation discussed in Section 3.5.

3.3.1. IDENTIFICATION OF STRUCTURED MATRICES IN DYNAMIC ABERRATION MODELS

The key realization for efficiently modelling the aberration dynamics is that the VARX model of (3.11) can be accurately represented by highly sparse matrices A, Q^{-1} and B. When a type of DM is considered for which its actuators only have a local influence on the total wavefront, B will be a sparse matrix. The remainder of this subsection will focus on the sparsity of the matrices A and Q^{-1}.

To support this assumption, a graphical model representation of the VARX model can be considered [28]. An intuitive interpretation of the theory in [28] to atmospheric turbulence implies that the matrices A and Q^{-1} are sparse banded matrices. This banded sparsity corresponds to the ability of predicting a single pixel only using those in its close neighbourhood. Such an assumption holds, for example, in situations where the turbulence can indeed be approximated by Taylor's frozen flow hypothesis, as is done in this work. The sparsity structure of the matrices A and Q^{-1} is defined by the sets $\mathscr{S}_A$ and $\mathscr{S}_{Q^{-1}}$ respectively, each denoting the location of the non-zero entries in their corresponding matrix. A more detailed analysis of sparsity structures in dynamic AO systems can be found in [29, 30]. Sparsity structures in AO systems are not unique to the dynamic aberration model. For example, [31] shows that sparsity structure can also be exploited for static wavefront reconstruction.

To compute A and Q^{-1}, different approaches are possible, depending on the available information, such as computing them from first principles, choosing them by manual tuning, or via system identification techniques [27]. The remainder of this subsection will show how A and Q^{-1} can be computed via system identification; however, if the covariance matrix $C_\phi = E\left[\boldsymbol{\phi}(k)\boldsymbol{\phi}^T(k)\right]$ is known, A and Q are related via $Q = C_\phi - AC_\phi A^T$.

To identify A and Q^{-1} from data, a time series with N_{id} time samples of open-loop wavefront data is retrieved using either a dedicated WFS or any WFSless wavefront reconstruction method. This batch will be denoted by $\{\boldsymbol{\phi}_{id}(i)|i = 1,2,\ldots,N_{id}\}$. The matrix A can be identified by solving the following constrained least squares problem [27]:

$$\begin{aligned} \min_{A} \quad & \|A\Phi_1 - \Phi_2\|_F^2 \\ \text{s.t.} \quad & A \in \mathscr{S}_A, \end{aligned} \tag{3.18}$$

where $\Phi_1 = [\boldsymbol{\phi}_{id}(1)\cdots\boldsymbol{\phi}_{id}(N_{id}-1)]$ and $\Phi_2 = [\boldsymbol{\phi}_{id}(2)\cdots\boldsymbol{\phi}_{id}(N_{id})]$. The set $\mathscr{S}_A$ describes the set of all matrices A that have a desired sparsity pattern. Since the exact optimal sparsity pattern is usually unknown, but rather an over-approximation is used, 1-norm regularization on A can be added to further increase the sparsity [30].

Having computed an estimate of A, an estimate of $\boldsymbol{w}(k)$ can be found by computing $\hat{\boldsymbol{w}}(k) = \boldsymbol{\phi}_{id}(k+1) - A\boldsymbol{\phi}_{id}(k)$ for $k = 1,\ldots,N_{id}-1$. Afterwards, a sample covariance matrix,

$$Q_s = \frac{1}{N_{id}-1}\sum_{i=1}^{N_{id}-1} \hat{\boldsymbol{w}}(k)\hat{\boldsymbol{w}}^T(k), \tag{3.19}$$

can be computed such that a sparse approximation of Q_s^{-1} could serve as an estimate of Q^{-1}. Alternatively, Q_s^{-1} can be estimated directly from $\hat{\boldsymbol{w}}(k)$ by creating a matrix W, where each k-th column of W corresponds to $\frac{1}{\sqrt{N_{id}-1}}\hat{\boldsymbol{w}}(k)$. Next, a matrix Ξ is computed such that $\Xi W = O$, $O \in \mathbb{R}^{n\times n}$ being an orthonormal matrix. This matrix Ξ can be found using the Gramm-Schmidt method and Q_s^{-1} can then be computed via $Q_s^{-1} = \Xi^T\Xi$, since $Q_s = WW^T = \Xi^{-1}OO^T\Xi^{-T} = \Xi^{-1}\Xi^{-T}$. Hence, Ξ can be seen as the inverse square root of Q_s. Since Q^{-1} is expected to be banded and sparse, its square root Ξ is expected to have an accurate sparse approximation. During the Gramm-Schmidt procedure, the desired sparsity pattern of Ξ can easily be enforced, both speeding up the process and finding a sparse approximation.

Since the model of (3.10) is not capable of exactly representing the true turbulence dynamics, manually fine-tuning $\hat{Q}$ could improve the performance. Also, when n is very large and the dataset N_{id} is limited, problems could occur regarding ill-conditioning of the matrix Q_s. One simple way of tuning $\hat{Q}$ is to take it equal to $Q_s+\gamma I$. As a rule of thumb throughout this chapter, γ is tuned such that mean(diag($\Xi^T\Xi$)) = 1/mean(diag($\hat{Q}$)).

Furthermore, for applications where the sparsity of Q^{-1} would be unknown, finding a sparse inverse of an sample covariance Q_s has been studied well in graphical modelling literature. Several algorithms have been presented that solve this problem, which can be used to increase the sparsity of the estimate Q^{-1} further when desired, see for example [32].

3.3.2. EFFICIENT COMPUTATIONS OF THE OUTPUT EQUATION

Since the output equation is non-linear, a first-order Taylor approximation with respect to $\boldsymbol{\phi}$ can be used to linearlize (3.12). The first-order Taylor approximation around the initial estimate $\hat{\boldsymbol{\phi}}$ will be denoted by

$$\boldsymbol{y}(k) \approx J_{\hat{\phi}}(\boldsymbol{\phi}(k) - \hat{\boldsymbol{\phi}}) + \boldsymbol{c}_{\hat{\phi}} + \boldsymbol{v}(k), \tag{3.20}$$

where, if we define $f(\boldsymbol{\phi}) = |\mathscr{F}_{vec}\{\boldsymbol{a} \odot \exp(i\boldsymbol{\phi})\}|^2$, $\boldsymbol{c}_{\hat{\phi}} = f(\hat{\boldsymbol{\phi}})$ and $J_{\hat{\boldsymbol{\phi}}} = f'(\hat{\boldsymbol{\phi}})$, i.e., the Jacobian matrix corresponding $f(\boldsymbol{\phi})$ evaluated at $\hat{\boldsymbol{\phi}}$.

Although there are no sparse matrices in the output equation (3.12), the efficient FFT algorithm can be used to compute the 2D DFT. For the first-order Taylor approximation of (3.20), an efficient computation of the matrix-vector multiplication $J_{\hat{\phi}}\boldsymbol{\phi}$ can be formulated using the FFT algorithm, thereby avoiding the explicit computation of the complete Jacobian. When introducing $\hat{\boldsymbol{x}} = \boldsymbol{a} \odot \exp(i\hat{\boldsymbol{\phi}})$ and $\hat{\boldsymbol{y}} = \mathscr{F}_{vec}\{\hat{\boldsymbol{x}}\}$, the following operators can be introduced:

$$J_{\hat{\phi}}\boldsymbol{\phi} \rightarrow \mathscr{J}_{\hat{\boldsymbol{\phi}}}(\boldsymbol{\phi}) \triangleq \Re\left(2i\hat{\boldsymbol{y}} \odot \mathscr{F}_{vec}\{\hat{\boldsymbol{x}} \odot \boldsymbol{\phi}\}\right), \tag{3.21}$$

$$J^T_{\hat{\phi}}\boldsymbol{\psi} \rightarrow \mathscr{J}^T_{\hat{\boldsymbol{\phi}}}(\boldsymbol{\psi}) \triangleq \Re\left(-2i\hat{\boldsymbol{y}}^* \odot \mathscr{F}^{-1}_{vec}\{\hat{\boldsymbol{x}}^* \odot \boldsymbol{\psi}\}\right), \tag{3.22}$$

where $\mathscr{F}^{-1}_{vec}\{\cdot\}$ represents the vectorized 2D inverse DFT, and $\hat{\boldsymbol{y}}^*$ and $\hat{\boldsymbol{x}}^*$ represent the element-wise complex conjugates of $\hat{\boldsymbol{y}}$ and $\hat{\boldsymbol{x}}$, respectively. In Section 3.5, both the sparsity structures of A and Q^{-1}, and the operators in Eqs. (3.21-3.22) will be used to develop an efficient non-linear Kalman filter implementation.

3.4. KALMAN FILTERS FOR WFSLESS AO

Kalman filters are widely used as a state observer for many applications and they are treated in many textbooks [27]. At each time step k, the Kalman filter involves two steps: a *measurement update* and a *time update*. The goal of the measurement update is to optimally combine a new measurement $\boldsymbol{y}(k)$ with a previous state estimate $\hat{\boldsymbol{\phi}}(k|k-1)$ into an improved update $\hat{\boldsymbol{\phi}}(k|k)$. The time update uses the dynamical model to predict the state for the next time step, which will be denoted by $\hat{\boldsymbol{\phi}}(k+1|k)$.

The accuracy of the estimates is expressed in terms of the error-covariance matrices

$P(k+1|k)$ and $P(k|k)$ for the time update and measurement update, respectively:

$$P(k+1|k) := E[(\boldsymbol{\phi}(k) - \hat{\boldsymbol{\phi}}(k+1|k))(\boldsymbol{\phi}(k) - \hat{\boldsymbol{\phi}}(k+1|k))^T], \tag{3.23}$$

$$P(k|k) := E[(\boldsymbol{\phi}(k) - \hat{\boldsymbol{\phi}}(k|k))(\boldsymbol{\phi}(k) - \hat{\boldsymbol{\phi}}(k|k))^T]. \tag{3.24}$$

The Kalman filter computes the estimates $\hat{\boldsymbol{\phi}}(k+1|k)$ and $\hat{\boldsymbol{\phi}}(k|k)$, such that their error-covariance matrices are minimal [27]. Since the state equation (3.11) is linear, the time update will be equivalent to the classical Kalman filter. The measurement update can be formulated as a regularized non-linear least squares problem:

$$\begin{aligned}\hat{\boldsymbol{\phi}}(k|k) = \arg\min_{\boldsymbol{\phi}\in\mathbb{R}^n} &\left\|\hat{\boldsymbol{\phi}}(k|k-1) - \boldsymbol{\phi}\right\|^2_{P^{-1}(k|k-1)} + \dots \\ &\left\|\boldsymbol{y}(k) - \left|\mathscr{F}_{vec}\left\{\boldsymbol{a}\odot\exp(i\boldsymbol{\phi})\right\}\right|^2\right\|^2_{R^{-1}(k)},\end{aligned} \tag{3.25}$$

where the weight matrix $P(k|k-1)$ is the error-covariance matrix corresponding to $\boldsymbol{\phi}(k) - \hat{\boldsymbol{\phi}}(k|k-1)$. Because of the non-linearity of the output equation of the state-space model, a non-linear adaptation of the measurement update has to be used.

3.4.1. KALMAN FILTERING AND THE PHASE RETRIEVAL PROBLEM

If the Kalman filter measurement update is compared to the phase retrieval problem, many similarities appear, see for example [33] for an overview of different phase estimation methods. Many algorithms have been proposed that aim to solve the PR problem in its original non-convex optimization framework [7, 10]. In general, the optimization framework could be formulated as

$$\min_{\boldsymbol{x}\in\mathbb{C}^n} \|\boldsymbol{y} - |\mathscr{F}_{vec}(\boldsymbol{x})|^2\|^2_{W_y} + \|\hat{\boldsymbol{x}} - \boldsymbol{x}\|^2_{W_x}, \tag{3.26}$$

where W_x, W_y are weight matrices and for any vector $\boldsymbol{\alpha}$ and matrix M: $\|\boldsymbol{\alpha}\|^2_M := \boldsymbol{\alpha}^H M\boldsymbol{\alpha}$. Most methods do not use the second term as there generally is no prior information $(\hat{\boldsymbol{x}},\ W_x)$ considered to be available. Due to the non-convexity of the first term, a very accurate initial condition is computed first before attempting to solve the problem using either a gradient descent or second-order optimization algorithm. Obtaining this initial estimate when considering Fourier measurements is not trivial. This is where a Kalman filter and knowledge of the aberration dynamics can be used to its advantage.

When the amplitude in the pupil plane $\boldsymbol{a}$ is known, the problem can be rewritten to solve for $\boldsymbol{\phi}$ directly:

$$\min_{\boldsymbol{\phi}\in\mathbb{R}^n} \|\boldsymbol{y} - |\mathscr{F}_{vec}\{\boldsymbol{a}\odot\exp(i\boldsymbol{\phi})\}|^2\|^2_{W_y} + \|\hat{\boldsymbol{\phi}} - \boldsymbol{\phi}\|^2_{W_\phi}, \tag{3.27}$$

with W_ϕ another weighting matrix. Although this formulation of the PR problem is not often used in existing literature due to the required extra information $\boldsymbol{a}$ and the extra non-linearity caused by the exponential $\exp(i\boldsymbol{\phi})$, it is more convenient for the dynamic case due to the convenient linear state update equation (3.11) in terms of $\boldsymbol{\phi}$. Moreover, when aiming to reconstruct the wavefront from a single image, knowledge of $\boldsymbol{a}$ is a significant advantage for obtaining a good performance. Considering the formulation of the phase retrieval problem as in (3.27) and comparing it to the Kalman filter measurement

update of (3.25), the similarities are obvious. The Kalman filter provides a framework to define optimal weight matrices W_ϕ and W_y, and uses the model dynamics to find the initial estimate $\hat{\boldsymbol{\phi}}$.

3.4.2. SOLVING THE PHASE RETRIEVAL PROBLEM USING A KALMAN FILTER

The next step is to solve the non-linear measurement update (3.25). The most well-known method is to use a linear Taylor approximation to solve the non-linear measurement update, which is known in Kalman filter theory as the Extended Kalman filter (EKF). In this chapter, the Gauss-Newton algorithm is applied to the non-linear optimization problem. Solving the measurement update (3.25) using the Gauss-Newton algorithm leads to a filter is known as the iterated extended Kalman filter (IKF) [34]. The IKF, as the name suggests, is an iterative version of the EKF. It is interesting to draw similarities here with other existing PR algorithms in literature that aim to solve the related formulation of (3.26) via a gradient descend or Gauss-Newton optimization schemes [7, 10].

When a straightforward implementation of the IKF is used, the iterations of the measurement update become as follows: initializing $\boldsymbol{\phi}_0 = \hat{\boldsymbol{\phi}}(k|k-1)$ and $P_0 = P(k|k-1)$, for $\ell = 0, 1, \ldots, L$:

$$\boldsymbol{\phi}_{\ell+1} = (I - K_\ell J_{\phi_\ell})\hat{\boldsymbol{\phi}}(k|k-1) + K_\ell \left(\boldsymbol{y}(k) - \boldsymbol{c}_{\phi_\ell} + J_{\phi_\ell}\boldsymbol{\phi}_\ell\right), \tag{3.28}$$

$$P_{\ell+1} = \left(I - K_\ell J_{\phi_\ell}\right) P(k|k-1), \tag{3.29}$$

with J_{ϕ_ℓ} and $\boldsymbol{c}_{\phi_\ell}$ as defined in (3.20), where

$$K_\ell = P(k|k-1) J_{\phi_\ell}^T \left(J_{\phi_\ell} P(k|k-1) J_{\phi_\ell}^T + R(k)\right)^{-1}, \tag{3.30}$$

and, after the last iteration, $\hat{\boldsymbol{\phi}}(k|k) = \boldsymbol{\phi}_L$ and $P(k|k) = P_L$. The time update becomes equal to the standard KF update:

$$\hat{\boldsymbol{\phi}}(k+1|k) = A\hat{\boldsymbol{\phi}}(k|k) - B\boldsymbol{u}(k) + AB\boldsymbol{u}(k-1), \tag{3.31}$$

$$P(k+1|k) = AP(k|k)A^T + Q. \tag{3.32}$$

The most important problem with this method is its large computational complexity; therefore, a computationally efficient formulation of the IKF is presented in Section 3.5.

3.4.3. ADVANTAGE DYNAMIC VERSUS STATIC APPROACH

This subsection discusses the advantages of considering the dynamic case with respect to the static case. For both cases, we restrict this discussion to the case in which the pupil plane amplitude is considered to be known, i.e. the optimization problem of (3.27).

In the static case, without any knowledge of the model dynamics, phase retrieval aims to solve (3.27) for $W_y = I$ and $W_\phi = 0$ (i.e., disregarding the second term). This often creates problems regarding the non-uniqueness of the solution when only a single image is used, and, without an accurate initial guess, algorithms usually do not converge to an accurate solution. Usually, the uniqueness problem is overcome by considering multiple images along the optical axis (also known as phase diversity [35]), but this involves splitting the light further and re-introduces the problem with NCPAs.

When considering the dynamic case, the phase retrieval problem is reformulated as the measurement update of the Kalman filter, i.e. (3.25). Compared to the static case, the problem of uniqueness becomes the problem of *observability* [27]. Where the uniqueness in the static case is purely defined by the output equation, observability depends on both the output equation and the state dynamics. Even when the output equation alone does not lead to a unique solution in the static case, adding knowledge of the dynamics can make the system observable. As a consequence, the Kalman filter measurement update in (3.25) is much more likely to result in an accurate estimate compared to the the static case. The prior information $\hat{\boldsymbol{\phi}}(k|k-1)$, $P(k|k-1), R(k)$ obtained from the dynamic model and noise model, acts as an optimally weighted *regularization* to the static phase retrieval problem. Since the regularization term $\left\|\hat{\boldsymbol{\phi}}(k|k-1)-\boldsymbol{\phi}\right\|^2_{P^{-1}(k|k-1)}$ is convex, it significantly helps solvers aiming to solve the non-linear optimization problem in (3.25). The addition of this extra knowledge opens the possibility for considering situations impossible to accurately solve in the static case, such as only considering a single out-of-focus image, or even considering a single in-focus image.

Another advantage of this optimally weighted regularization term is that, due to the extra knowledge of the measurement noise, the algorithm also becomes much less sensitive to noise. A common method to deal with measurement noise in the static case is to hard-threshold the image and discard all measured pixels in $\boldsymbol{y}(k)$ smaller than y_{min} from the measurements. Since the optimal choice of y_{min} depends on the noise level σ_r, the value of y_{min} is difficult to optimally tune. The Kalman filter does not need this truncation parameter as the noise is already taken into account by the application of the weighting matrices $R(k)$ and $P(k|k-1)$, resulting in a more consistent algorithm under noisy circumstances.

3.5. EFFICIENT NON-LINEAR KALMAN FILTER IMPLEMENTATION

In Section 3.3, it was discussed how, due to the underlying nature of the dynamics, the inverse covariance matrices corresponding to $\boldsymbol{\phi}(k)$ and $\boldsymbol{w}(k)$ (i.e. C_ϕ^{-1} and Q^{-1}) are expected to be sparse. As a consequence, the inverse error-covariance matrix of the KF, P^{-1}, is expected to have an accurate sparse approximation as well. Therefore, the *information filter* representation of the KF is used, which only uses the inverse error covariance matrices $P^{-1}(k|k)$ and $P^{-1}(k+1|k)$. To summarise, the new filter consists of 4 main steps: (1) compute the measurement update $\hat{\boldsymbol{\phi}}(k|k)$ via (3.25), (2) compute inverse error-covariance matrix $P^{-1}(k|k)$, (3) compute time update $\hat{\boldsymbol{\phi}}(k+1|k)$ via (3.31) and, (4) compute inverse error-covariance matrix $P^{-1}(k+1|k)$. The computation of the time update $\hat{\boldsymbol{\phi}}(k+1|k)$ (step 3) is straightforward. Since the matrix A and B are sparse, this update can be performed very efficiently. Efficient implementations of the other steps will be discussed in the remainder of this section.

The notation $\mathcal{O}(\cdot)$ will be used to describe how the number of elementary computations $(+,-,\times,\div)$ scale with respect to certain parameters. For example, the notation $\mathcal{O}(n^3)$ represents that if the system dimension n doubles, the number of required elementary computations increase by a factor $2^3 = 8$. A method is considered to scale better with respect to the system dimensions when the exponent is as low as possible. All computational complexities will be summarized in Table 3.2.

Table 3.2: Computational complexities per step of the algorithm. p_c represents the rank of the approximated term in (3.37), L is number of the IKF iterations, L_{CG} is the average number of CG iterations. The other symbols are included in Table 3.1.

Step in algorithm	**Computational complexity**
Compute $\hat{\phi}(k\|k)$ by solving (3.34) via CG method	$\mathcal{O}(n(c_{P^{-1}}+\log n)LL_{CG})$
Explicitly computing p_c rows of the Jacobian	$\mathcal{O}(np_c)$
Sparse low-rank approximation of $P^{-1}(k\|k)$ in (3.37)	$\mathcal{O}(np_c c_{P^{-1}})$
Compute $\hat{\phi}(k+1\|k)$ via (3.31)	$\mathcal{O}(nc_A+mc_B)$
Computing sparse inverse approximation via solving (3.39)	$\mathcal{O}(n(c_\Gamma^3+c_{M_2}c_\Gamma^2))$
Sparse approximation of $P^{-1}(k+1\|k)$ in (3.40)	$\mathcal{O}(nc_{M_1}^2 c_{P^{-1}})$

An important advantage of the implementation presented is that the state measurement update is computed efficiently using the full PSF as input, i.e. no truncation or cropping of the image is performed. The only necessary approximations are in the updates of the matrix P^{-1}. Since P^{-1} acts as just a weight matrix in the measurement update, it is expected that small inaccuracies in P^{-1} affects the performance of the algorithm much less significantly than manually truncating the data $\boldsymbol{y}(k)$.

3.5.1. STATE MEASUREMENT UPDATE

Recall the Kalman filter measurement update formulation given by (3.25). Introducing the increment $\delta\boldsymbol{\phi}_\ell := \boldsymbol{\phi}_{\ell+1}-\boldsymbol{\phi}_\ell$, the ℓ-th iteration of the IKF measurement update can be reformulated into the following optimization problem:

$$\delta\boldsymbol{\phi}_\ell = \arg\min_{\delta\boldsymbol{\phi}\in\mathbb{R}^n} \left\|\hat{\boldsymbol{\phi}}(k|k-1)-\boldsymbol{\phi}_\ell-\delta\boldsymbol{\phi}\right\|^2_{P^{-1}(k|k-1)} + \left\|\boldsymbol{y}(k)-J_{\phi_\ell}\delta\boldsymbol{\phi}-\boldsymbol{c}_{\phi_\ell}\right\|^2_{R^{-1}(k)}, \tag{3.33}$$

where $\boldsymbol{\phi}_{\ell+1}=\delta\boldsymbol{\phi}_\ell+\boldsymbol{\phi}_\ell$ is equal to the results presented in (3.28). Since computing (3.28) by using (3.30) has a computational complexity of $\mathcal{O}(n^3)$, it is too computationally demanding for large values of n. Therefore, the above least-squares problem is solved using an iterative solver that exploits the fast operators (3.21) and (3.22). One possible iterative algorithm is the conjugate gradient (CG) algorithm, which can be found in many textbooks, e.g. [36].

First, the normal equations corresponding to the least squares problem are formulated:

$$\begin{aligned}\left(J_{\phi_\ell}^T R^{-1}(k)J_{\phi_\ell}+P^{-1}(k|k-1)\right)\delta\boldsymbol{\phi} &= \dots \\ J_{\phi_\ell}^T R^{-1}(k)\left(\boldsymbol{y}(k)-\boldsymbol{c}_{\phi_\ell}\right)+P^{-1}(k|k-1)\left(\hat{\boldsymbol{\phi}}(k|k-1)-\boldsymbol{\phi}_\ell\right),\end{aligned} \tag{3.34}$$

such that the matrix on the left hand side is square, symmetric and positive definite. With the insights of Section 3.3, evaluating the vectors on both the left- and right-hand side of this system of equations requires only matrix vector multiplications with sparse matrices P^{-1} and R^{-1} and the operators (3.21) and (3.22). Hence, two new efficient operators are introduced:

$$\mathcal{M}(\delta\boldsymbol{\phi};\ell,k) := \mathcal{J}_{\boldsymbol{\phi}_\ell}^T\left(R^{-1}(k)\mathcal{J}_{\phi_\ell}\left(\delta\boldsymbol{\phi}\right)\right)+P^{-1}(k|k-1)\delta\boldsymbol{\phi}, \tag{3.35}$$

$$\mathcal{B}(\boldsymbol{y};\ell,k) := \mathcal{J}_{\boldsymbol{\phi}_\ell}^T\left(R^{-1}(k)\left(\boldsymbol{y}(k)-\boldsymbol{c}_{\phi_\ell}\right)\right)+P^{-1}(k|k-1)\left(\hat{\boldsymbol{\phi}}(k|k-1)-\boldsymbol{\phi}_\ell\right), \tag{3.36}$$

Algorithm 1 Efficient IKF Meausurement update

procedure IKF-MU($\boldsymbol{y}(k), \delta\boldsymbol{\phi}_0, tol$)
  $\boldsymbol{\phi}_0 \leftarrow \hat{\boldsymbol{\phi}}(k|k-1)$
  for $\ell \leftarrow 1 : L$ **do** ▷ Start IKF iterations
    $\boldsymbol{r}_0 \leftarrow \mathscr{B}(\boldsymbol{y}(k); \ell, k) - \mathscr{M}(\delta\boldsymbol{\phi}_0; \ell, k)$ ▷ (3.35),(3.36)
    $\boldsymbol{p}_0 \leftarrow \boldsymbol{r}_0$
    $i \leftarrow 0$
    while $\boldsymbol{r}^T\boldsymbol{r} > tol$ **do** ▷ Start CG iterations
      $\boldsymbol{z}_i \leftarrow \mathscr{M}(\delta\boldsymbol{\phi}_i; \ell, k)$ ▷ (3.35)
      $\alpha_i \leftarrow \frac{\boldsymbol{r}_i^T\boldsymbol{r}_i}{\boldsymbol{p}_i^T\boldsymbol{z}_i}$
      $\delta\boldsymbol{\phi}_{i+1} \leftarrow \delta\boldsymbol{\phi}_i + \alpha_i\boldsymbol{p}_i$
      $\boldsymbol{r}_{i+1} \leftarrow \boldsymbol{r}_i - \alpha_i\boldsymbol{z}_i$
      $\beta_i \leftarrow \frac{\boldsymbol{r}_{i+1}^T\boldsymbol{r}_{i+1}}{\boldsymbol{r}_i^T\boldsymbol{r}_i}$
      $\boldsymbol{p}_{i+1} = \boldsymbol{r}_{i+1} - \beta_i\boldsymbol{p}_k$
      $i \leftarrow i+1$
    $\boldsymbol{\phi}_{\ell+1} \leftarrow \delta\boldsymbol{\phi}_{i+1} + \boldsymbol{\phi}_\ell$ ▷ End CG iterations
  $\hat{\boldsymbol{\phi}}(k|k) \leftarrow \boldsymbol{\phi}_\ell$ ▷ End IKF iterations
  return

such that $\mathscr{M}(\delta\boldsymbol{\phi}; \ell, k)$ is equal to the vector on the left-hand side of (3.34) and $\mathscr{B}(\boldsymbol{y}(k); \ell, k)$ to the right-hand side. Since R^{-1} is diagonal, both (3.35) and (3.36) have a computational complexity of $\mathscr{O}(n(c_{P^{-1}} + \log n))$, $c_{P^{-1}}$ being the average number of non-zero elements per row/column of P^{-1}. This allows the CG algorithm to find the solution $\hat{\boldsymbol{\phi}}(k|k)$ in a computational efficient manner, presented in Algorithm 1.

3.5.2. ERROR-COVARIANCE MEASUREMENT UPDATE

The next step is to find an update of the matrix $P^{-1}(k|k)$:

$$P^{-1}(k|k) = P^{-1}(k|k-1) + J_{\phi_\ell}^T R^{-1}(k) J_{\phi_\ell}, \tag{3.37}$$

which has two difficulties. First of all, computing term $J_{\phi_\ell}^T R^{-1}(k) J_{\phi_\ell}$ using the operators (3.21) and (3.22) still has a complexity of $\mathscr{O}(n^2\log(n))$. Secondly, the same term is not necessarily sparse, so in order to maintain a sparse matrix $P^{-1}(k|k)$, a sparse approximation has to be made. The approximation that is proposed is to represent the matrix $J_{\phi_\ell}^T R^{-1}(k) J_{\phi_\ell}$ as a low-rank, sparse matrix. By assuming the low-rank property, only a small part of the Jacobian has to be computed. The sparsity property is necessary to obtain a sparse updated matrix that can be efficiently used in the next time step.

The method for computing the low-rank approximation is based on a common procedure in phase retrieval algorithms, which is to discard dark pixels in the PSF that are highly corrupted by noise. Since the proposed method is to be used for small phase aberrations only, it is expected that the PSF will be relatively sharp and its brightest pixels will be concentrated around its center. Hence, most of the information used for the measurement update is contained in the center pixels, and, consequently, the update $P^{-1}(k|k)$ will mainly depend on the part of the Jacobian corresponding to these center

pixels. Explicitly computing the rows of the Jacobian corresponding to the pixels located in the (much smaller) $\bar{p}_c \times \bar{p}_c$ center square, has a computational complexity of $\mathcal{O}(np_c)$, where $p_c := \bar{p}_c^2$.

Finally, it is used that the desired sparsity pattern of $P^{-1}(k|k)$ is known; therefore, only the elements of $J_{\phi_\ell}^T R^{-1}(k) J_{\phi_\ell}$ that correspond to this sparsity pattern have to be computed. When there are an average of $c_{P^{-1}}$ non-zero elements per row of $P^{-1}(k|k)$, the total computational of this step is $\mathcal{O}(np_c c_{P^{-1}})$.

3.5.3. ERROR-COVARIANCE TIME UPDATE

After computing the time update via (3.31), the corresponding inverse error covariance matrix can be computed via

$$P^{-1}(k+1|k) = Q^{-1} - M_1 \left(P^{-1}(k|k) + M_2\right)^{-1} M_1^T, \tag{3.38}$$

where $M_1 := Q^{-1}A$ and $M_2 := A^T Q^{-1} A$ can be pre-computed offline to speed up the computations. Notice that all matrices A, Q^{-1} and $P^{-1}(k|k)$ are sparse banded matrices, but that the inverse $\left(P^{-1}(k|k) + M_2\right)^{-1}$ is not sparse in general. However, it is known that since the matrix $P^{-1}(k|k) + M_2$ is a banded and positive definite matrix, its inverse belongs to the class of off-diagonal decaying matrices and can be approximated by a sparse matrix [37].

The computation of this approximation of $P^{-1}(k+1|k)$ is split in two steps. First, the following approximate sparse inverse matrix is computed via

$$\begin{aligned} \hat{\Gamma} = \arg\min_{\Gamma} \quad & \left\| \left(P^{-1}(k|k) + M_2\right)\Gamma - I \right\|_F^2 \\ \text{s.t.} \quad & \Gamma \in \mathcal{S}_\Gamma \end{aligned} \tag{3.39}$$

such that $\hat{\Gamma}$ is a sparse estimate of $\left(P^{-1}(k|k) + M_2\right)^{-1}$ and $\mathcal{S}_\Gamma$ is the set of all matrices corresponding to the desired (chosen) sparsity pattern for Γ. The second step is to compute

$$P^{-1}(k+1|k) = Q^{-1} - M_1 \Gamma M_1^T. \tag{3.40}$$

The sparsity of $P^{-1}(k+1|k)$ (defined by the set $\mathcal{S}_{P^{-1}}$) is known. Hence, when computing (3.40), only the entries in $P^{-1}(k+1|k)$ corresponding to this desired sparsity pattern $\mathcal{S}_{P^{-1}}$ have to be computed.

To analyze the computational complexity, the average number of non-zeros per row/column of the matrices Γ, M_1 and M_2 are denoted by c_Γ, c_{M_1} and c_{M_2}, respectively, and the sets of matrices corresponding to the chosen sparsity patterns of M_1 and M_2 will be defined as $\mathcal{S}_{M_1}$ and $\mathcal{S}_{M_2}$, respectively. For the sake of simplifying the notations, we restrict this analysis to the typical case where all matrices are banded and where $c_\Gamma \geq c_{M_1}$ is chosen such that $\mathcal{S}_{M_1} \subseteq \mathcal{S}_\Gamma$. By exploiting the sparsity structures and only computing the elements of $P^{-1}(k+1|k)$ that are in the sparsity set $\mathcal{S}_{P^{-1}}$, the computational complexity of (3.40) will be of the order $\mathcal{O}(nc_{M_1}^2 c_{P^{-1}})$ and computing the matrix $\hat{\Gamma}$ in (3.39) will be of the order $\mathcal{O}(n(c_\Gamma^3 + c_{M_2} c_\Gamma^2))$.

Parameter	Standard value
Fried parameter r_0 [m]	0.2
Wind speed v, layer 1 [m/s]	12
Wind speed v, layer 2 [m/s]	16
Source magnitude β_m	8
read-out noise σ_r [photons]	2
Telescope diameter D [m]	1
WFS lenslet grid size $\bar{q}$	6
DM grid size $\bar{q}+1$	7
Wavefront grid size $\bar{n}$	30
Sample frequency f_s [Hz]	500
Outer scale L_0 [m]	15

Table 3.3: Simulation parameters. If not mentioned otherwise, the standard values are used. Turbulence layer 2 is located at an altitude of 5000 m and is moving at an angle of 90° w.r.t. layer 1 located at 0m. The conversion of magnitude β_m to photon flux is given by (3.17). The source is a single natural guide star.

3.6. SIMULATION DESIGN

This section discusses the simulation environment used to provide an illustration of the IKF's performance. For the first-order Taylor approximation in (3.20) to hold, the RMS-value of the wavefront observed by the focal-plane camera, denoted by RMS($\boldsymbol{\phi}$), should be sufficiently small. Unfortunately, for larger telescope diameters and realistic atmospheric conditions, RMS($\boldsymbol{\phi}$) will be too large; therefore, it is chosen to position the IKF within a closed-loop AO system, as small-phase aberrations are the typical situation within a control loop [12]. In this example, a WFS-based minimum variance estimate (WFS-MVE) of the wavefront is used to drive the controller [38]. The goal of this parallel controller is to compensate for dominant low-order aberrations in the wavefront in order to keep RMS($\boldsymbol{\phi}$) sufficiently low. The open source Matlab toolbox OOMAO [25] is used to simulate the turbulence and AO system.

The WFS-MVE will also be used as a baseline during the performance evaluations, as it defines the value of RMS($\boldsymbol{\phi}$) to be estimated by the focal-plane wavefront sensing methods. It is important to note that the WFS-MVE should not be interpreted as the optimal performance of WFS-based methods in general, as the SH sensor only estimates the low-order aberrations due to its limited number of lenslets.

In order to put the performance of the IKF in further perspective, it is compared to an alternating projection (AP) method based on the Gerchberg-Saxton [1] algorithm in a phase diversity framework [35] (referred to as AP-PD). To improve the convergence of the AP-PD algorithm, its estimate at the previous time instance is used as an initial estimate, and all pixels observing less than $y_{min} = 5$ photons are set to zero to decrease the influence of the measurement noise.

It should be emphasized that the AP-PD method assumes to have two phase diversity images taken simultaneously along the optical axis, while the proposed IKF only uses a single focal-plane image. Although the AP-PD method has this unfair advantage over the IKF method, it will provide an estimate of the expected maximum achievable performance of classical PR methods. Due to its access to two diversity images, the performance of AP-PD should not be significantly affected by the aberration dynamics and

therefore serves as a benchmark to see if the IKF can achieve a similar performance under highly dynamic circumstances.

As a measure of performance, the distance $d(k)$ in the pupil plane between the true and estimated GPF will be used in order to avoid issues regarding phase-unwrapping:

$$d(k) = \min_{\phi_p \in [0,2\pi]} \|\boldsymbol{x}(k) - e^{i\phi_p}\hat{\boldsymbol{x}}(k|k)\|_2^2, \tag{3.41}$$

where $\boldsymbol{x}(k) = \boldsymbol{a} \odot e^{i\boldsymbol{\phi}(k)}$ and $\hat{\boldsymbol{x}}(k|k) = \boldsymbol{a} \odot e^{i\hat{\boldsymbol{\phi}}(k|k)}$, for $\hat{\boldsymbol{\phi}}(k|k)$ as given in (3.25). The scalar ϕ_p expresses the piston offset between the real and estimated phase. A normalization of this distance is defined as

$$d_n(k) = \frac{d(k)}{\|\boldsymbol{x}(k)\|_2^2}. \tag{3.42}$$

Once a time sequence of k_{tot} steps has been obtained, a scalar measure of the accuracy over the full time sequence is computed by taking the root mean square: RMS($\boldsymbol{d}_n$), where $\boldsymbol{d}_n \in \mathbb{R}^{k_{tot}}$ is a vector containing $d_n(k)$, $k = 1, \ldots, k_{tot}$.

3.7. RESULTS

This section presents the results of the simulations discussed in the previous section. All parameters have their standard value of Table 3.3 unless mentioned otherwise.

3.7.1. COMPUTATIONAL EFFICIENCY

The main result presented in this chapter is the scalable IKF implementation; therefore, the computational efficiency of the algorithm in terms of execution time will be tested for an increasing system size. In this experiment, the telescope diameter D, number of WFS lenslets $\bar{q}$, and resolution of the reconstruction $\bar{n}$ are increased in a way such that their relative ratios are still the same as in Table 3.3. For each parameter setting, a time sequences of 50 steps is simulated and the execution time is tracked for each time step. The increase in computational burden due to the higher resolution is visualised in Figure 3.2 and compared with the straightforward IKF presentation of Section 3.4. Comparing the results of the efficient IKF with the reference line of $\mathcal{O}(n)$ confirms the almost linear complexity ($\mathcal{O}(n\log(n))$) of the efficient implementation. The improvement in terms of the scalability of the new algorithm opens up the possibility for a real-time implementation.

3.7.2. INFLUENCE OF THE WAVEFRONT DYNAMICS AND RMS-VALUE

Next, the robustness of the method with respect to the wavefront dynamics and value of RMS($\boldsymbol{\phi}$) is investigated by varying v and r_0. For each parameter setting, 10 independent time sequences of 500 steps are simulated in a Monte Carlo simulation. The results in Figure 3.3 show that the IKF algorithm performs significantly better for moderate conditions (low v, large r_0). This can be explained by two factors.

Firstly, since the VAR-1 aberration dynamics model is more accurate at mild conditions, varying v and r_0 will provide information on the limits of the method with respect

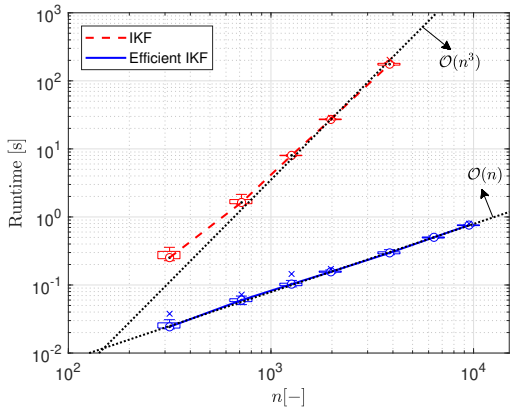

Figure 3.2: Computation time per time step for an increasing resolution n. The boxes indicate the 25th and 75th percentile over the time sequence. Lines are drawn through the medians. The dotted lines present a slope corresponding to a complexity of $\mathcal{O}(n^3)$ and $\mathcal{O}(n)$ for reference purposes. "Efficient IKF" is the new method, "IKF" is the IKF implementation of Section 3.4.

to the accompanying model. This effect explains the decrease in performance when increasing v, as the wind speed has the largest influence on the accuracy of the model.

Secondly, since the IKF relies on a linear Taylor approximation, it is expected to rely significantly on the magnitude of the residual aberrations, RMS($\boldsymbol{\phi}$). When RMS($\boldsymbol{\phi}$) becomes too large, the Taylor approximation will no longer be valid at this range. Consequently, the performance will rely on the accuracy of the controller since the accuracy of the WFS-MVE determines the value of RMS($\boldsymbol{\phi}$). The clear dependence on RMS($\boldsymbol{\phi}$) is visualised in Figure 3.3b, which shows corresponding values of RMS($\boldsymbol{\phi}$) for a certain choice of r_0 on the top horizontal axis. This shows that the method is able to track aberrations up to a value of RMS($\boldsymbol{\phi}$) ≈ 1 rad.

Since the wavefront estimates $\hat{\boldsymbol{\phi}}(k|k)$ are compared and not the predictions $\hat{\boldsymbol{\phi}}(k+1|k)$, the AP-PD algorithm is influenced much less by the atmospheric conditions. This is expected, since it uses multiple simultaneous images and it does not rely on prior information given by a dynamical model or a linear approximation.

The results of Figure 3.3b are particularly interesting since it gives useful insights with respect to the estimation of NCPAs. That is, the residual wavefront $\boldsymbol{\phi}$ represents a mismatch between the WFS-based wavefront reconstruction and the corresponding measured PSF image. Hence, this implies that compensating for NCPAs should not be a problem under two assumptions. The first being that the total residual aberration has RMS($\boldsymbol{\phi}$) < 1 rad, and the second that the dynamics of the NCPAs are contained within the dynamical model.

3.7.3. ROBUSTNESS TO MEASUREMENT NOISE

The robustness to measurement noise was previously addressed in Section 3.4, where it was argued that the KF algorithm is expected to have an increased performance under noisy conditions without user defined tuning parameters. The influence of the shot

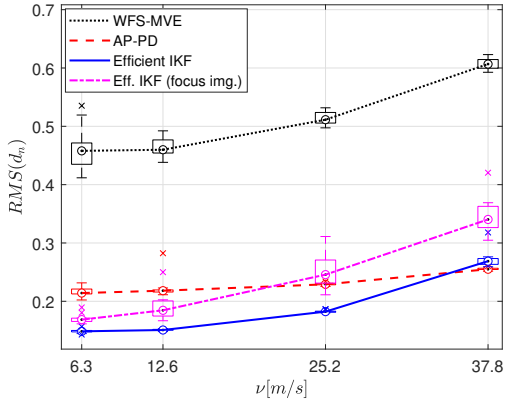

(a) Results for varying v. The value shown on the x-axis is the speed of the layer 1. The speed of layer 2 is changed accordingly.

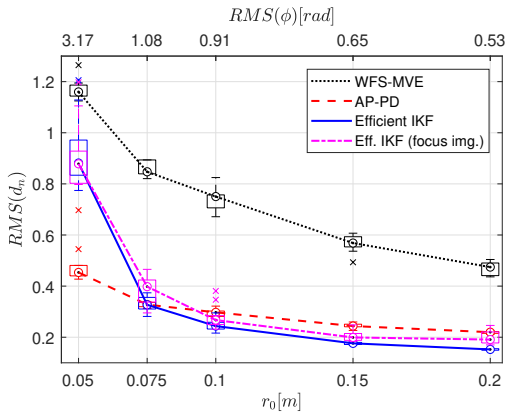

(b) Results when varying r_0. The top horizontal axis shows the value of RMS($\boldsymbol{\phi}$) for the corresponding r_0.

Figure 3.3: Results for varying the atmospheric conditions. The boxplots show the RMS of the normalized distance of (3.42). The boxes indicate the 25th and 75th percentile of the results in a Monte Carlo simulation. Lines are drawn through the medians. "Efficient IKF" has a single focal-plane camera out of focus, whereas "Eff. IKF (focus img.)" has a camera placed in focus. The AP-PD method uses two phase diversity images.

noise is now investigated by varying the brightness of the source. Figure 3.4 shows the performance for an increasing magnitude β_m, i.e. a decreasing brightness in terms of photon flux β_f (see (3.17)). The performance of the IKF deteriorates much less significantly when the magnitude is increased compared to the AP-PD algorithm. This shows that the IKF is more robust for low signal-to-noise ratios, which occur in low brightness conditions, than classical phase diversity methods. Moreover, under low-noise conditions, it shows that the IKF, using only a single focal-plane image, is able to retrieve an estimate that is as accurate as the AP-PD method, which uses two images. The low medians show that even when using a single in focus image, the IKF performs well in most

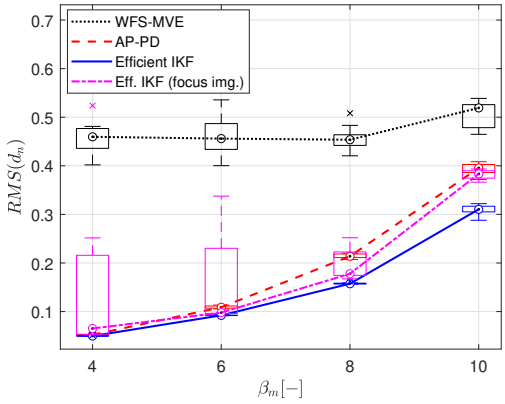

Figure 3.4: Results for varying the brightness of the source. The presentation of the boxplots is the same as Fig. 3.3.

cases, but the performance is much less consistent considering the large spread of the boxplots.

3.8. CONCLUSIONS

A computationally efficient framework has been proposed in which a single focal-plane image is used to obtain a high-resolution reconstruction of dynamic aberrations. The framework is based on a reformulation of the phase retrieval problem for dynamic aberrations into a Kalman filtering framework using a simple identified model of the dynamics. The computationally efficient implementation scales almost linearly with the number of pixels of the focal-plane camera, making the method suitable for high-resolution AO systems and opening up a real-time implementation as a topic for future research. In a simulation study, the low computational complexity was confirmed, and the accuracy of the method was analysed under varying conditions. It was discovered that the Kalman filter (using a single focal-plane image) is able to obtain an estimate that is as accurate as phase diversity methods (using two focal-plane images), even when considering highly dynamic aberrations. Moreover, it was shown that the Kalman filter is able to maintain a much better performance than classical phase diversity methods when considering lower signal-to-noise ratios. Finally, although in general measuring the PSF out of focus usually increases the performance, a single in focus PSF image was able to achieve satisfying results in many cases.

REFERENCES

[1] R. W. Gerchberg, *A practical algorithm for the determination of the phase from image and diffraction plane pictures,* Optik **35**, 237 (1972).

[2] J. R. Fienup, *Reconstruction of an object from the modulus of its Fourier transform,* Optics Letters **3**, 27 (1978).

[3] Y. Shechtman, Y. C. Eldar, O. Cohen, H. N. Chapman, J. Miao, and M. Segev, *Phase retrieval with application to optical imaging: a contemporary overview,* IEEE signal processing magazine **32**, 87 (2015).

[4] N. Hieu Thao, O. Soloviev, and M. Verhaegen, *Convex combination of alternating projection and douglas-rachford operators for phase retrieval,* arXiv .

[5] E. J. Candes, T. Strohmer, and V. Voroninski, *Phaselift: Exact and stable signal recovery from magnitude measurements via convex programming,* Communications on Pure and Applied Mathematics **66**, 1241 (2013).

[6] I. Waldspurger, A. d'Aspremont, and S. Mallat, *Phase recovery, MaxCut and complex semidefinite programming,* Mathematical Programming **149**, 47 (2015).

[7] E. J. Candes, Y. C. Eldar, T. Strohmer, and V. Voroninski, *Phase retrieval via matrix completion,* SIAM review **57**, 225 (2015).

[8] Y. Chen and E. J. Candès, *Solving random quadratic systems of equations is nearly as easy as solving linear systems,* Communications on Pure and Applied Mathematics **70**, 822 (2017).

[9] G. Wang, G. B. Giannakis, and Y. C. Eldar, *Solving systems of random quadratic equations via truncated amplitude flow,* IEEE Transactions on Information Theory **64**, 773 (2017).

[10] C. Ma, X. Liu, and Z. Wen, *Globally convergent levenberg-marquardt method for phase retrieval,* IEEE Transactions on Information Theory **65**, 2343 (2018).

[11] R. A. Gonsalves, *Small-phase solution to the phase-retrieval problem,* Optics Letters **26**, 684 (2001).

[12] C. Smith, R. Marinică, A. Den Dekker, M. Verhaegen, V. Korkiakoski, C. Keller, and N. Doelman, *Iterative linear focal-plane wavefront correction,* Journal of the Optical Society of America A **30**, 2002 (2013).

[13] S. Meimon, T. Fusco, and L. M. Mugnier, *Lift: a focal-plane wavefront sensor for real-time low-order sensing on faint sources,* Optics Letters **35**, 3036 (2010).

[14] V. Korkiakoski, C. U. Keller, N. Doelman, M. Kenworthy, G. Otten, and M. Verhaegen, *Fast & furious focal-plane wavefront sensing,* Applied Optics **53**, 4565 (2014).

[15] C. Smith, R. Marinica, and M. Verhaegen, *Real-time wavefront reconstruction from intensity measurements,* in *Proceedings of the 3rd AO4ELT Conference: Adaptive Optics for Extremely Large Telescopes, Florence, Italy, 26-31 May 2013* (Arcetri Astrophysical Observatory, 2013).

[16] R. Doelman, M. Klingspor, A. Hansson, J. Löfberg, and M. Verhaegen, *Identification of the dynamics of time-varying phase aberrations from time histories of the point-spread function,* Journal of the Optical Society of America A **36**, 809 (2019).

[17] J.-F. Sauvage, T. Fusco, G. Rousset, and C. Petit, *Calibration and precompensation of noncommon path aberrations for extreme adaptive optics,* Journal of the Optical Society of America A **24**, 2334 (2007).

[18] M. Wilby, C. Keller, J.-F. Sauvage, T. Fusco, D. Mouillet, J.-L. Beuzit, and K. Dohlen, *A" fast and furious'" solution to the low-wind effect for sphere at the vlt,* in *Adaptive Optics Systems V*, Vol. 9909 (International Society for Optics and Photonics, 2016) p. 99096C.

[19] H. Hofer, N. Sredar, H. Queener, C. Li, and J. Porter, *Wavefront sensorless adaptive optics ophthalmoscopy in the human eye,* Optics express **19**, 14160 (2011).

[20] Y. N. Sulai and A. Dubra, *Non-common path aberration correction in an adaptive optics scanning ophthalmoscope,* Biomedical optics express **5**, 3059 (2014).

[21] L. A. Poyneer and J.-P. Véran, *Kalman filtering to suppress spurious signals in adaptive optics control,* Journal of the Optical Society of America A **27**, A223 (2010).

[22] B. M. Welsh, *Fourier-series-based atmospheric phase screen generator for simulating anisoplanatic geometries and temporal evolution,* in *Propagation and Imaging through the Atmosphere*, Vol. 3125 (International Society for Optics and Photonics, 1997) pp. 327–338.

[23] S. A. Burns, A. E. Elsner, K. A. Sapoznik, R. L. Warner, and T. J. Gast, *Adaptive optics imaging of the human retina,* Progress in retinal and eye research **68**, 1 (2019).

[24] N. Ji, T. R. Sato, and E. Betzig, *Characterization and adaptive optical correction of aberrations during in vivo imaging in the mouse cortex,* Proceedings of the National Academy of Sciences **109**, 22 (2012).

[25] R. Conan and C. Correia, *Object-oriented matlab adaptive optics toolbox,* in *Adaptive optics systems IV*, Vol. 9148 (International Society for Optics and Photonics, 2014) p. 91486C.

[26] F. Assémat, R. W. Wilson, and E. Gendron, *Method for simulating infinitely long and non stationary phase screens with optimized memory storage,* Optics express **14**, 988 (2006).

[27] M. Verhaegen and V. Verdult, *Filtering and system identification: a least squares approach* (Cambridge university press, 2007).

[28] J. Songsiri, J. Dahl, and L. Vandenberghe, *Graphical models of autoregressive processes,* Convex optimization in signal processing and communications , 89 (2010).

[29] C. Yu and M. Verhaegen, *Structured modeling and control of adaptive optics systems,* IEEE Transactions on Control Systems Technology **26**, 664 (2017).

[30] P. Piscaer, *Sparse VARX Model Identification for Large-Scale Adaptive Optics*, Master's thesis, TU Delft (2016), retrieved from http://resolver.tudelft.nl/uuid:9677ebd9-cf4c-484c-97f8-1f553cd0e873.

[31] B. L. Ellerbroek, *Efficient computation of minimum-variance wave-front reconstructors with sparse matrix techniques,* Journal of the Optical Society of America A **19**, 1803 (2002).

[32] J. Friedman, T. Hastie, and R. Tibshirani, *Sparse inverse covariance estimation with the graphical lasso,* Biostatistics **9**, 432 (2008).

[33] L. M. Mugnier, A. Blanc, and J. Idier, *Phase diversity: a technique for wave-front sensing and for diffraction-limited imaging,* Advances in Imaging and Electron Physics **141**, 1 (2006).

[34] B. M. Bell, *The iterated kalman smoother as a gauss–newton method,* SIAM Journal on Optimization **4**, 626 (1994).

[35] R. A. Gonsalves, *Phase retrieval and diversity in adaptive optics,* Optical Engineering **21**, 215829 (1982).

[36] Y. Saad, *Iterative methods for sparse linear systems*, Vol. 82 (siam, 2003).

[37] A. Haber and M. Verhaegen, *Framework to trade optimality for local processing in large-scale wavefront reconstruction problems,* Optics Letters **41**, 5162 (2016).

[38] B. Ellerbroek and T. Rhoadarmer, *Adaptive wavefront control algorithms for closed loop adaptive optics,* Mathematical and Computer modelling **33**, 145 (2001).

4

PREDICTIVE WAVEFRONT SENSORLESS ADAPTIVE OPTICS FOR TIME-VARYING ABERRATIONS

A new wavefront sensorless adaptive optics method is presented that can accurately correct for time-varying aberrations using a single focal plane image at each sample instance. The linear relation between the mean square of the aberration gradient and the change in second moment of the image forms the basis of the presented method. The new algorithm results in significant improvements when an accurate model of the aberration's temporal dynamics is known, by applying a Kalman filter and optimal control. Moreover, where existing wavefront sensorless adaptive optics methods update all modes sequentially, the information of the Kalman filter is used to select and update the modes that are expected to give the largest improvement in performance. The performance is analyzed in a simulation of an adaptive optics system for atmospheric turbulence. The results show that the new method is able to correct for the aberration more accurately for larger wind speeds and higher noise levels than existing algorithms.

The contents of this chapter have been published in Piscaer, P., Soloviev, O., Verhaegen, M., *Predictive wavefront sensorless adaptive optics for time-varying aberrations*, JOSA A 36, 1810 (2019).

4.1. INTRODUCTION

Wavefront sensorless (WFSless) adaptive optics (AO) systems are systems in which the aberrations of the wavefront have to be corrected without using a dedicated wavefront sensor (WFS). Instead, only the images of a focal-plane camera are used. The correction is applied to a deformable mirror (DM) in order to minimize the effect of the aberration on the image quality. Finding an accurate correction without a WFS is challenging because of the non-linearity of the underlying optimization problem. Various WFSless AO algorithms have been developed [1–4]. The common features of these methods is that they are all iterative and require many measurements to converge. Recently, WFSless AO also has gained attention in free-space optical communication leading to new developments [5, 6].

Alternatively, an accurate correction can be found by solving the phase retrieval problem [7]. However, this either requires additional constraints, such as knowledge of the field's amplitude in the pupil plane, or requires multiple simultaneous measurements at different positions along the optical axis. Furthermore, the phase retrieval problem for AO systems is computationally very demanding and would limit the sampling frequency of the control loop significantly [8].

A recent development in WFSless AO is an approach that only requires $m+1$ measurements, where m is the number corrected modes [9, 10] and is often referred to as model-based or second moment (SM)-based WFSless AO. A modal basis is used that is spanned by the influence functions of the deformable mirror. This type of method has been shown to converge faster than other optimization algorithms [11]. The key of this approach is the linear relation between the mean square of the phase aberration gradient and the change in SM of the point spread function (PSF). By exploiting this linear relation, a closed-form expression of the correction can be computed. In contrast with iterative algorithms, this method is, due to its fast convergence, promising for real-time AO applications in which the aberration is time varying.

However, this method is still only useful when the aberrations are static or changing very slowly over time. Since the method relies on the assumption that the aberration is not changing over taking all $m+1$ measurement images, the performance decreases rapidly when the aberrations are moving faster. In [11], a method is used that requires the aberration not to change over only two measurement images. However, this method does not aim to predict the evolution of the aberration over time, nor discusses the effect of measurement noise on the method's performance. Modelling the aberration's temporal behaviour and the application of Kalman filter theory has been proven to be successful to deal with time-varying aberrations and measurement noise in the field of AO for astronomy [12, 13]. Therefore, the effects of including a temporal aberration model and Kalman filter for WFSless AO are studied in this chapter.

This chapter presents an extension of the methods described in [9, 11, 14] for aberrations that are continuously changing over time and for which an accurate temporal model is available or can be identified. An example of an application that deals with this type of aberrations is AO for astronomy [12]. From now on, these aberrations will be referred to as dynamic or time-varying aberrations. When a dynamic model of the aberration is available, Kalman filter theory and optimal control is applied to close the loop and compute the optimal DM commands. The Kalman filter is used to predict the aber-

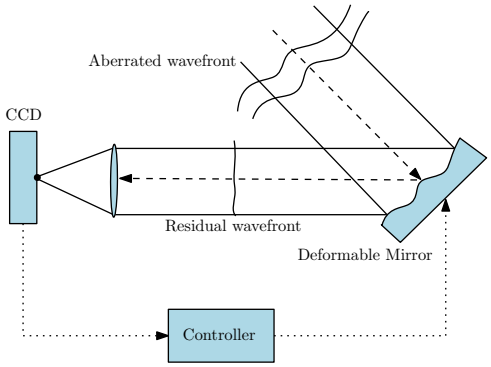

Figure 4.1: Schematic representation of a WFSless AO setup.

ration in the future and to select and update the measurement image(s) that are expected to give the largest improvement in performance. The performance will be analysed in a simulation study of an AO system that corrects for aberrations caused by atmospheric turbulence and is compared to the method in [14].

The remainder of this chapter is structured as follows. First, the existing framework of SM-based WFSless AO is explained and its limitation for dynamic aberration correction is discussed. Section 4.3 presents the new SM-based WFSless AO method for time varying aberrations. The simulation environment is discussed in Section 4.4, which considers a case study of dynamic aberrations caused by atmospheric turbulence. The performance of the new method is presented in Section 4.5, where it is compared to the existing SM-based WFSless AO method [14]. The main conclusions are summarized in Section 4.6.

4.2. SECOND MOMENT-BASED WAVEFRONT SENSORLESS ADAPTIVE OPTICS

A SM-based approach to WFSless AO has already been shown to outperform the iterative algorithms in terms of convergence speeds when applying correction for a static aberration. Recently, this was also applied to the case of dynamic aberrations [14]. For completeness, this section summarizes the theory of this SM-based WFSless AO approach. A scheme of a WFSless AO setup is shown in Figure 4.1.

The main goal of WFSless AO is to correct for a residual phase aberration in the pupil plane, $\phi(\boldsymbol{\chi})$, with pupil-plane coordinates $\boldsymbol{\chi} = \begin{bmatrix}\chi_1 & \chi_2\end{bmatrix}^T \in \mathbb{R}^2$. Define the PSF $I(\boldsymbol{\zeta}, \phi)$ with image-plane coordinates $\boldsymbol{\zeta} \in \mathbb{R}^2$ as

$$I(\boldsymbol{\zeta}, \phi) = \left| \mathscr{F}\left(\mathscr{A}(\boldsymbol{\chi}) e^{i\phi(\boldsymbol{\chi})} \right) \right|^2, \tag{4.1}$$

where $\mathscr{F}(\cdot)$ is the 2D Fourier transform and $\mathscr{A}$ is the amplitude apodization function. The unaberrated PSF will be denoted by $I(\boldsymbol{\zeta}, 0)$. Furthermore, the SM of the aberrated

PSF is defined as

$$z(\phi) = \int_{\mathbb{R}^2} I(\boldsymbol{\zeta}, \phi)|\boldsymbol{\zeta}|^2 d\boldsymbol{\zeta}. \tag{4.2}$$

An important relation that forms the basis of this method is that the difference between SM of the aberrated PSF and that of the unaberrated PSF is proportional to the mean square gradient of the wavefront [10]. It has been shown that

$$\int_{\mathbb{R}^2} \big(I(\boldsymbol{\zeta}, \phi) - I(\boldsymbol{\zeta}, 0)\big)|\boldsymbol{\zeta}|^2 d\boldsymbol{\zeta} = \frac{1}{4\pi^2} \int_{\mathbb{R}^2} \mathscr{A}^2(\boldsymbol{\chi})|\nabla\phi(\boldsymbol{\chi})|^2 d\boldsymbol{\chi}, \tag{4.3}$$

i.e., the SM of the intensity distribution change in the focal plane is proportional to the integral of the square of the phase derivative multiplied by the amplitude apodization function. This can be denoted more compactly as

$$z(\phi) - z(0) = c_0 \|\nabla\phi\|_2^2, \tag{4.4}$$

where $z(0)$ is the SM of the unaberrated PSF and $c_0 = \frac{1}{4\pi^2}$ [10]. Notice that (4.4) is a scalar equation. Decreasing the information of an image into a scalar and the compact modal description of our aberration reduces the dimensionality of the WFSless AO problem and opens the possibility for applying real-time filtering and prediction to improve the performance in the dynamic case.

4.2.1. STATIC ABERRATION CORRECTION

Define the deformable mirror influence functions as $E_j(\boldsymbol{\chi})$ for each actuator $j = 1, \ldots, m$. Each actuator is poked independently such that this phase will be added to the existing residual aberrated wavefront $\phi(\boldsymbol{\chi})$. It is important to notice that, since a residual wavefront is observed by the focal-plane camera, computed control signals will always be incremental and have to be added on top of the current control signal.

An inherent property of the SM-based WFSless AO approach for control is that it will always be unable to compensate for the part of the aberration that is orthogonal to the DM basis. However, the true aberration, $\tilde{\phi}(\boldsymbol{\chi})$, actually is

$$\tilde{\phi}(\boldsymbol{\chi}) = \phi(\boldsymbol{\chi}) + \phi_\perp(\boldsymbol{\chi}), \tag{4.5}$$

where

$$\phi(\boldsymbol{\chi}) = \sum_{j=1}^{m} u_j E_j(\boldsymbol{\chi}), \tag{4.6}$$

such that $\phi(\boldsymbol{\chi})$ represents the part of the aberration that is within the span of the DM influence functions, and $\phi_\perp(\boldsymbol{\chi})$ is the part orthogonal to it. Generally, in the derivation of the control law, it is assumed that $\tilde{\phi}(\boldsymbol{\chi}) = \phi(\boldsymbol{\chi})$, such that only $\phi(\boldsymbol{\chi})$ will be estimated. However, it has to be noted that this is an approximation and that $\phi_\perp(\boldsymbol{\chi})$ will have an influence on the measurements in practice [15]. Also in the simulations, $\phi_\perp(\boldsymbol{\chi})$ will affect the measurements.

SM-based WFSless AO aims to find the coefficients u_j describing the aberration most accurately. In the general SM-based WFSless AO method [9], each actuator is poked sequentially. When poking actuator j with an amplitude β on top of the current control signals, the total phase of the field measured by the camera will be

$$\phi_j(\boldsymbol{\chi}) = \beta E_j(\boldsymbol{\chi}) + \phi(\boldsymbol{\chi}). \tag{4.7}$$

Defining the matrix $S \in \mathbb{R}^{m\times m}$ and vector $\boldsymbol{s} \in \mathbb{R}^m$ as

$$S_{ij} = \int\int_{\mathbb{R}^2} \left(\frac{\partial E_i}{\partial \chi_1}\frac{\partial E_j}{\partial \chi_1} + \frac{\partial E_i}{\partial \chi_2}\frac{\partial E_j}{\partial \chi_2} \right) d\chi_1 d\chi_2, \tag{4.8}$$

$$s_i = \int\int_{\mathbb{R}^2} \left(\frac{\partial E_i}{\partial \chi_1} \right)^2 + \left(\frac{\partial E_i}{\partial \chi_2} \right)^2 d\chi_1 d\chi_2, \tag{4.9}$$

with S_{ij} denoting the element on row i and column j in the matrix S and s_i denoting element i in the vector $\boldsymbol{s}$. Using the linear relation of (4.4), we can form the following system of linear equations:

$$\boldsymbol{y}_m \triangleq \begin{bmatrix} z(\phi_1) - z(\phi) \\ \vdots \\ z(\phi_m) - z(\phi) \end{bmatrix} = C_m \boldsymbol{u} + \boldsymbol{y}_{m,0}, \tag{4.10}$$

where $\boldsymbol{y}_m \in \mathbb{R}^m$, $C_m = 2\beta c_0 S$, $\boldsymbol{y}_{m,0} = \beta^2 c_0 \boldsymbol{s}$, $c_0 = \frac{1}{4\pi^2}$ (see [10] for a more detailed derivation). The vector $\boldsymbol{u} \in \mathbb{R}^m$ contains the ideal increment of DM control commands u_j that have to be added to the current DM control signal. Solving (4.10) for $\boldsymbol{u}$ gives us the modal description of the aberration $\phi(\boldsymbol{\chi})$ as in (4.6). From (4.10), a closed-form solution for $\boldsymbol{u}$ can be expressed as

$$\boldsymbol{u} = C_m^{-1}\left(\boldsymbol{y}_m - \boldsymbol{y}_{m,0}\right). \tag{4.11}$$

Once the control $\boldsymbol{u}$ has been applied, a new measurement $\boldsymbol{y}_m$ is computed by sequentially poking the actuators, and a new control increment $\boldsymbol{u}$ is computed.

4.2.2. CHALLENGES FOR TIME-VARYING ABERRATIONS

When the method described in Section 4.2.1 is applied to time-varying aberrations, some difficulties arise. Denote the dynamic aberrated wavefront by $\phi(\boldsymbol{\chi}, t)$, with t describing the current discrete time instance. Furthermore, assume it takes T_i seconds to collect an image and compute its SM. A total of $m+1$ images have to be taken. First, a reference image is taken, followed by m images, each corresponding to poking a different actuator. When sequentially poking all actuators and including the fact that $\phi(\boldsymbol{\chi}, t)$ is time-varying, the total phase aberration corresponding to the image with the j^{th} actuator poked, previously (4.7), becomes time-varying:

$$\phi_j(\boldsymbol{\chi}, t + jT_i) = \beta E_j(\boldsymbol{\chi}) + \phi(\boldsymbol{\chi}, t + jT_i). \tag{4.12}$$

This causes the reference image to be taken at time instance t, while the image after poking the last actuator is at time $t + mT_i$. Therefore, there is a time difference of mT_i

between the reference image and the image corresponding to poking actuator m. A detailed discussion of the timeline of this control problem is given Section 4.3. When there is no compensation for this delay, this will introduce an error, since the equation (4.10) is no longer valid.

One way of decreasing the effect of this time delay is to update the actuators one by one, taking a new reference image in between. However, the linear system of equations (4.10) is in general not a decoupled system. A new basis can be formulated in order to have a diagonal matrix C. Such a diagonalization is proposed in [11] and used for dynamic aberrations in [14]. For completeness, this is shortly summarized in the next subsection. It should be noted that, although the maximum time difference between the images can be reduced from $(m+1)T_i$ to just $2T_i$, not all problems are resolved. First of all, there is still a (small) delay between the two images that is not taken into account in [11]. Second, there is a time of $2mT_i$ between updating the same mode again. These problems will be treated by the new method proposed in Section 4.3.

4.2.3. DIAGONALIZING THE LINEAR SYSTEM

The closed-form solution of (4.11) can be separated along the elements of $\boldsymbol{u}$ when C_m is diagonal. The singular value decomposition (SVD) of S,

$$S = U\Sigma U^T, \tag{4.13}$$

can be used to formulate a new basis that results in a decoupled linear equation. Σ is a diagonal matrix and is shown to correspond to the correlation matrix (formerly S for the basis of (4.6)) for the basis described by basis functions $\tilde{E}_j(\boldsymbol{\chi}) = E(\boldsymbol{\chi})U_j,\ j = 1,\ldots,m$ [11], where $E = [E_1(\boldsymbol{\chi}), E_2(\boldsymbol{\chi}),\ldots,E_m(\boldsymbol{\chi})]$ and U_j the j^{th} column of U. Consequently, the update in terms of the new basis becomes

$$\boldsymbol{u}_d = C_d^{-1}\left(\boldsymbol{y}_{d,m} - \boldsymbol{y}_{d,0}\right), \tag{4.14}$$

where $\boldsymbol{y}_d$ contains the changes of the SM of the PSF corresponding to actuating the new set of modes $\tilde{E}_j(\boldsymbol{\chi})$, $C_d = 2\beta c_0\Sigma$ and $\boldsymbol{y}_{d,0}$ is a vector containing the diagonal elements of $\beta^2 c_0\Sigma$. Since C_d^{-1} is diagonal, it is no longer necessary to wait until m measurement images are taken, but the elements in $\boldsymbol{u}_d$ can be updated after a reference image and a single measurement image.

4.3. PREDICTIVE SECOND MOMENT-BASED WFSLESS AO

In order to have a more systematic approach of dealing with time varying aberrations, a dynamic model that exploits the spatio-temporal relations in the wavefront will be used. Combining the aberration dynamics with (4.10), a linear state-space model is obtained. The pupil plane coordinates $\boldsymbol{\chi}$ are discretized and sampled on an n-by-n grid, such that the wavefront at time instance t can be represented by the vector $\boldsymbol{\phi}(t) \in \mathbb{R}^{n^2}$. Similarly, the DM influence functions $E_j(\boldsymbol{\chi})$ are sampled on the same square grid and each function is represented by the vector $\boldsymbol{e}_j \in \mathbb{R}^{n^2}$. The influence matrix is defined as $E = [\boldsymbol{e}_1,\ \boldsymbol{e}_2,\ldots,\ \boldsymbol{e}_m] \in \mathbb{R}^{n^2\times m}$. For reasons discussed in the previous section, it is assumed that the wavefront can be written as (4.6), such that only the part of the aberration that is within the span of the DM influence functions will be modelled.

First, without considering the time index yet, a general modal basis with coefficient vector $\boldsymbol{x} \in \mathbb{R}^m$ is defined to represent any wavefront $\phi(\boldsymbol{\chi})$ in (4.6). The relation between the coefficient vector $\boldsymbol{u}$ and $\boldsymbol{x}$ of either basis is given by an invertible matrix $B \in \mathbb{R}^{m\times m}$ such that

$$\boldsymbol{x} = B\boldsymbol{u}. \tag{4.15}$$

Using this modal basis, the observable part of the phase, $\boldsymbol{\phi}$, can per definition be modelled as

$$\boldsymbol{\phi} = E\boldsymbol{u} = EB^{-1}\boldsymbol{x}. \tag{4.16}$$

In the simulations, both $\boldsymbol{x}$ and $\boldsymbol{u}$ will correspond to the same modal basis, i.e. $B = I$. It should be noted that although both $\boldsymbol{x}$ and $\boldsymbol{u}$ represent coefficients belonging to a basis spanning the same space, they will be used to represent different processes $\boldsymbol{x}(t)$ and $\boldsymbol{u}(t)$ in the remainder of this chapter. This will be clarified in Sections 4.3.1 and 4.3.2 of this section, in which a dynamic model of the wavefront will be expressed in terms of $\boldsymbol{x}(t)$ and a Kalman filter is derived.

The output $\boldsymbol{y}(t) \in \mathbb{R}^p$ will be similar to (4.10). Due to the use of a Kalman filter, it is possible to update the DM with a smaller number of images by poking a selection of actuators, i.e., any $p \leq m$ can be taken without diagonalizing the system as in Section 4.2.3. The exact definition of $\boldsymbol{y}(t)$ and the reason that p can be different from m will be explained further in the following subsections. Since the collection of one image is done once every T_i seconds, the total time it takes to collect the data for the measurement vector $\boldsymbol{y}(t)$ is $(p+1)T_i$ seconds. The output is updated every $T = (p+1)T_i$ seconds, while the input will still be updated every T_i seconds. As a result, the model becomes a so-called multi-rate linear time-invariant system, where the input and output are obtained over different sample periods. Although the input and output sampling rate are different, they are uniformly sampled and the sample times coincide every $p+1$ samples. A schematic representation of one output sample time is shown in Figure 4.2.

The next subsection will discuss the temporal model of the open loop aberration. Afterwards, the resulting closed-loop state-space system and a Kalman filter implementation is discussed, followed by an optimal controller using the predictions from the Kalman filter. In the last subsection of this section, it is explained how the information given by the Kalman filter can be used to select which actuator to poke for the next measurement. Table 4.1 gives an overview of important notations that are used throughout this section.

4.3.1. DYNAMIC ABERRATION MODEL

The temporal dynamics of the aberration caused by the turbulence, denoted by $\boldsymbol{x}_t(k) \in \mathbb{R}^m$, will be described by a vector auto regressive (VAR) model of order 1. Two different models are defined. One has the output sample time T, and the other has the input sample time T_i. The two models are the following:

$$\boldsymbol{x}_t(kT_i + T_i) = A_f\boldsymbol{x}_t(kT_i) + \boldsymbol{w}_f(kT_i), \tag{4.17}$$

$$\boldsymbol{x}_t(kT + T) = A\boldsymbol{x}_t(kT) + \boldsymbol{w}(kT) \tag{4.18}$$

Table 4.1: **Table of notations**

m	Number of actuators
p	Number of selected modes per update
$z(\cdot)$	Second moment of the PSF. See (4.2)
$\boldsymbol{x}(t)$	State vector (residual aberration in mode coefficients)
$\boldsymbol{u}(t)$	Input vector (actuator command)
$\boldsymbol{y}(t)$	Output vector (change in second moment)
A, A_f, Q, Q_f	Aberration dynamics. See (4.17) and (4.18).
B	Transformation matrix. See (4.15).
$C(t), \boldsymbol{y}_0(t)$	The rows of C_m or $\boldsymbol{y}_{0,m}$ that are in $\mathscr{I}(t)$
$\mathscr{I}(t)$	The set of p active actuators
T	Output sampling time
T_i	Input sampling time
β	The amplitude of actuation
$\boldsymbol{\phi}(t)$	vectorized residual phase aberration
$\boldsymbol{\phi}_j(t)$	$\boldsymbol{\phi}$ plus actuator j poked. See (4.12)
$\boldsymbol{\chi}$	Pupil plane coordinates

where $\boldsymbol{w}_f(k)$ and $\boldsymbol{w}(k)$ are zero-mean Gaussian processes with covariance matrices Q_f and Q respectively, i.e. $w_f(k) \sim \mathcal{N}(0, Q_f)$ and $\boldsymbol{w}(k) \sim \mathcal{N}(0, Q)$. The simulations will focus on the example of aberrations introduced by atmospheric turbulence. However, it should be noted that the proposed method works for any type of dynamic aberration that can be accurately represented by this type of model.

The matrices A, A_f, Q and Q_f can be derived from first principles, requiring knowledge of the turbulence statistics, wind direction and wind speed. When this knowledge is not available, the system matrices can be identified when a sufficiently large dataset of open-loop aberration data $\{\boldsymbol{x}_t(kT_i),\ k = 1, 2, \ldots, N_{id}\}$ is available. With this data, the identification of the matrices A, A_f, Q and Q_f follows from a linear least-squares problem [16]. The simulations will use a simulated identification dataset to identify the system dynamics. The exact method to obtain this identification dataset in practice is beyond the scope of this chapter. Since the model identification is done offline, a WFS can be temporally included in the AO system or computational complex methods can be used to collect this dataset. When a wavefront sensor is included in the system during the identification data collection, the wavefront sensor measurements can be used to reconstruct a wavefront which is then mapped onto the desired modes to form the identification dataset. Alternatively, when additional constraints are available, such as a sparsity constraint or knowledge of the amplitude in the pupil plane, or when multiple images along the optical axis can be taken, there are existing methods that can obtain the identification dataset from solving the phase retrieval problem on a time series of focal-plane images (see [7] for an overview).

4.3.2. KALMAN FILTER IMPLEMENTATION

The loop is closed by the DM. The influence of the DM on the wavefront is defined as

$$\boldsymbol{x}_m(kT_i) = B\boldsymbol{u}(kT_i - T_i), \tag{4.19}$$

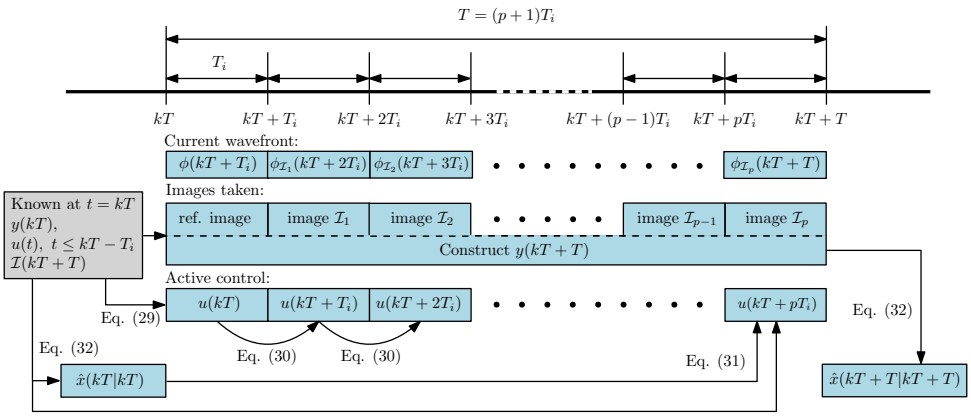

Figure 4.2: Schematic representation of the processes in one output sample time from kT until $(k+1)T$. The lines indicate the computation of the element in the box at it end, using the element(s) in the box it originates. Equation numbers are added to indicate which relation is used.

where the delay represents the fact that the DM can not respond instanteneously, and B is the transformation matrix defined in (4.15). In closed loop, the residual aberration, denoted by $\boldsymbol{x}(t) \in \mathbb{R}^m$, is defined as

$$\boldsymbol{x}(kT_i) = \boldsymbol{x}_t(kT_i) + \boldsymbol{x}_m(kT_i). \tag{4.20}$$

For the output $\boldsymbol{y}(kT) \in \mathbb{R}^p$, only a selection of images are taken and processed. Each output sample time a selection of p actuators, from the total of m actuators in our DM, is poked and the corresponding images are taken. Defining $\mathscr{I}(kT) = \{\mathscr{I}_1, \ldots, \mathscr{I}_p\} \subseteq \{1, 2, \ldots, m\}$ as the set of p distinct integer elements corresponding to the actuators that will be poked for the next measurement, the output equation $\boldsymbol{y}(kT)$, based on (4.10), is

$$\begin{aligned} \boldsymbol{y}(kT) &\triangleq \begin{bmatrix} z(\phi_{\mathscr{I}_1}(kT - (p-1)T_i)) - z(\phi(kT - pT_i)) \\ \vdots \\ z(\phi_{\mathscr{I}_p}(kT)) - z(\phi(kT - pT_i)) \end{bmatrix} \\ &= C(kT)\boldsymbol{x}(kT) + \boldsymbol{y}_0(kT) + \boldsymbol{v}(kT), \end{aligned} \tag{4.21}$$

where $\boldsymbol{v}(kT) \sim \mathcal{N}(0, R(kT))$. Moreover, $C(kT) \in \mathbb{R}^{p \times m}$ and $\boldsymbol{y}_0(kT) \in \mathbb{R}^p$ are chosen to be the selection of rows, given by the elements in $\mathscr{I}(kT)$, of C_m and $\boldsymbol{y}_{m,0}$ in (4.10), respectively. This choice implies that the temporal changes in the aberrated wavefront in between images can still be neglected, i.e., it is assumed that $\boldsymbol{x}(kT - jT_i) = \boldsymbol{x}(kT)$, for $j = 1, \ldots, p$. The validity of this simplification in closed loop will be discussed in the next subsection after introducing the optimal control law.

Combining (4.21) with Eq. (4.18, 4.19, 4.20), the following single-rate state-space model can be derived, which is sampled at the output sampling rate:

$$\boldsymbol{x}(kT + T) = A\boldsymbol{x}(kT) + B\boldsymbol{u}(kT) - AB\boldsymbol{u}(kT - T) + \boldsymbol{w}(kT), \tag{4.22}$$

$$\boldsymbol{y}(kT) = C(kT)\boldsymbol{x}(kT) + \boldsymbol{y}_0(kT) + \boldsymbol{v}(kT). \tag{4.23}$$

Next, a Kalman filter is derived for this system. Kalman filter theory can be found in many textbooks, such as [16], but due to the special nature of the output, the implementation is discussed in detail.

To arrive at an optimal prediction of the state vector, the Kalman filter essentially performs two steps: a measurement update, in which a newly obtained measurement is used to improve the current estimate of the state vector $\boldsymbol{x}(t)$, and a time update, where the model is used to predict that state vector. The measurement update is computed every output sample time and is given by

$$\hat{\boldsymbol{x}}(kT|kT) = \hat{\boldsymbol{x}}(kT|kT-T) + K(kT)\big(\boldsymbol{y}(kT) - C(kT)\hat{\boldsymbol{x}}(kT|kT-T) - \boldsymbol{y}_0(kT)\big), \tag{4.24}$$

where the Kalman gain $K(kT) \in \mathbb{R}^{m\times p}$ is computed using a square root implementation of the Riccati equation [16]. The time update gives the optimal prediction of the state vector one output sample time ahead:

$$\hat{\boldsymbol{x}}(kT+T|kT) = A\big(\hat{\boldsymbol{x}}(kT|kT) - B\boldsymbol{u}(kT-T_i)\big) + B\boldsymbol{u}(kT+pT_i). \tag{4.25}$$

In between the measurements, a different time update is done each input sample time by using the model in (4.17). This prediction of the state vector in between measurements is given by

$$\hat{\boldsymbol{x}}(kT+(j+1)T_i|kT) = A_f\big(\hat{\boldsymbol{x}}(kT+jT_i|kT) - B\boldsymbol{u}(kT+(j-1)T_i)\big) + B\boldsymbol{u}(kT+jT_i), \tag{4.26}$$

for $j = 0,1,\ldots,p-1$. At moment $(k+1)T$, a new measurement is obtained and a new measurement update like (4.24) is performed.

4.3.3. OPTIMAL CONTROL

The derived optimal state prediction in (4.25) and (4.26) is used to create an optimal controller. The control law aims to minimize the norms of the predicted residual wavefront coefficients, i.e.,

$$\min_{\boldsymbol{u}(kT+(j-1)T_i)} \left\|\hat{\boldsymbol{x}}(kT+jT_i|kT)\right\|_2^2, \quad j = 1,2,\ldots,p+1. \tag{4.27}$$

Here, $\hat{\boldsymbol{x}}(kT+jT_i|kT)$, $j = 1,2,\ldots,p$ is defined by (4.26), and $\hat{\boldsymbol{x}}(kT+T|kT)$ by (4.25). Due to the fact that B is invertible, solving (4.27) for $\boldsymbol{u}$, and applying these inputs in (4.25) and (4.26), per definition results in

$$\hat{\boldsymbol{x}}(kT+jT_i|kT) = 0, \quad \text{for } j = 1,2,\ldots,p+1, \tag{4.28}$$

as the least squares problem (4.27) boils down to solving a linear system of equations. (4.28) can be interpreted as follows. When the optimal control action according to (4.27) is applied, the expected residual wavefront is always equal to zero, i.e., it is expected to be a flat wavefront. This does not mean that the wavefront will actually be flat in practice, but it does show that with the available knowledge at time instance kT, the flat wavefront is the optimal estimate. With this insight, it can be concluded that the assumption that the residual wavefront has not changed between taking images, which was implied in (4.21), is optimal as long as an optimal controller is used as described in this paragraph.

Solving (4.27) and using that $\hat{\boldsymbol{x}}(kT+jT_i|kT)=0$, for $j=1,2,\ldots,p+1$, gives the following simplified optimal control actions:

$$\boldsymbol{u}(kT)=B^{-1}A_f\left(\hat{\boldsymbol{x}}(kT|kT)-B\boldsymbol{u}(kT-T_i)\right), \tag{4.29}$$

$$\boldsymbol{u}(kT+jT_i)=B^{-1}A_fB\boldsymbol{u}(kT+(j-1)T_i), \qquad \text{for } j=1,\ldots,p-1, \tag{4.30}$$

$$\boldsymbol{u}(kT+pT_i)=B^{-1}A\left(\hat{\boldsymbol{x}}(kT|kT)-B\boldsymbol{u}(kT-T_i)\right). \tag{4.31}$$

Consequently, the predictions of the state vector in (4.25) and (4.26) never have to be computed explicitly, as they per definition equal zero, and the measurement update simplifies to

$$\hat{\boldsymbol{x}}(kT|kT)=K(kT)\left(\boldsymbol{y}(kT)-\boldsymbol{y}_0(kT)\right). \tag{4.32}$$

4.3.4. ACTUATOR SELECTION ALGORITHM

Besides a more accurate prediction, having a model of the aberration dynamics results in another important advantage of this method. In [14], all modes are actuated sequentially and this is repeated after the last mode was actuated. In this section, a method is proposed that uses the information from the Kalman filter, rather than sequentially poking all modes. In other words, it uses the information in the Kalman filter to decide which set $\mathscr{I}(kT)$ in (4.21) will give the most informative measurements.

The selection method is based on the realization that the state error covariance matrix of the Kalman filter,

$$\begin{aligned}P(kT+jT_i|kT):=E\Big[&\left(\boldsymbol{x}(kT+jT_i)-\hat{\boldsymbol{x}}(kT+jT_i|kT)\right)\\&\left(\boldsymbol{x}(kT+jT_i)-\hat{\boldsymbol{x}}(kT+jT_i|kT)\right)^T\Big],\end{aligned} \tag{4.33}$$

describes the uncertainty of the estimate. In order to have a scalar measure, trace$[P(kT+jT_i|kT)]\in\mathbb{R}$ can be used to quantify the uncertainty. Minimizing this trace will mean a better estimate of the state vector, resulting in a better performance of the method. Therefore, the output channels that cause the biggest expected decrease in the trace of the covariance matrix of the state error in the Kalman filter are selected.

The basis of the actuator selection method lies in the fact that both the time and measurement update of the state error covariance do not require an actual measurement, but can be computed from the Riccati equation [16]. Consequently, at time $t=kT$, the values of e.g. $P(kT+T|kT+T)$ can be computed before actually observing the measurement at $t=kT+T$, assuming the selection of actuators $\mathscr{I}(kT+T)$, i.e. $C(kT+T)$ and $\boldsymbol{y_0}(kT+T)$ in (4.21), is known.

Of course, $\mathscr{I}(kT+T)$ is not known, but is the unknown still to be determined. However, it is known that there are only a finite number of sets possible. Theoretically, it is possible to compute $P(kT+T|kT+T)$ for all possible set $\mathscr{I}(kT+T)$, but for larger values of p there are too many possible combinations of actuators and this is therefore not practical. However, it is possible to compute the state error covariance matrix corresponding to poking a single actuator, i.e. $P(kT+2T_i|kT+2T_i)$. This leads to the following simple algorithm.

The first step is to compute, at $t=kT$, all possible values of $P(kT+2T_i|kT+2T_i)$. This requires solving the Riccati equation m times such that m different matrices are

Parameter	Standard value	Range
r_0 [m]	0.2	$0.1 - 0.35$
v [m/s]	1.6	$0.2 - 16$
σ_y	1	$10^{-2} - 5$
p	3	$1 - 35$
m	37	-
f_s [Hz]	1000	–
L_0 [m]	20	–
D [m]	1	–

Table 4.2: This table contains the simulation parameters. The parameters will have their "standard value" in each experiment when not explicitly mentioned otherwise. The last column shows the range in which they have been varied in an experiment.

obtained. The second step is to compare the value of trace$[P(kT+2T_i|kT+2T_i)]$ for each matrix. The p actuators that have lead to the p smallest values of trace$[P(kT+2T_i|kT+2T_i)]$ are defined as the next set of actuators to be updated, $\mathscr{I}(kT+T)$.

As a result of this actuator selection method, it is expected that the actuators located in an area where the dynamic model of the aberration is less accurate are updated more frequently. The Kalman filter including the optimal control law and actuator selection method are implemented in a simulation study that is discussed in the following section.

4.4. SIMULATION OF AO FOR ATMOSPHERIC TURBULENCE

The performance of the method is shown in a simulation of an AO system for atmospheric turbulence, where the aberrations in the wavefront shown in Figure 4.1 are caused by atmospheric turbulence, and are compared to another SM-based WFSless AO algorithm for dynamic aberrations [14]. This section will discuss the simulation conditions and discusses the implementation details of the algorithm. Table 4.2 summarizes the most important simulation parameters. The results of the simulations are presented in Section 4.5.

4.4.1. ADAPTIVE OPTICS SIMULATION DESIGN

The phase aberrations caused by the atmospheric turbulence is simulated using OOMAO [17]. A single turbulence layer is considered with Fried parameter r_0, outer scale L_0 and wind speed v. The telescope diameter will be fixed at $D = 1$ m and sample frequency at $f_s = 1000$ Hz, i.e. $T_i = \frac{1}{1000}$ s. In order to have a fair comparison between different wind speeds, a collection of wavefronts on a $n \times n$ grid of pixels have been generated at a speed of 1 pixel/T_i over a period of $\tilde{N}$ time samples. The simulated sequence of wavefronts are stored in a three dimensional tensor of dimension $n \times n \times \tilde{N}$. Afterwards, linear interpolation along the third dimension of this tensor is performed to obtain wavefronts at slower or faster wind speeds. A set of 20 turbulent wavefronts, each containing $N = 2000$ time samples, is created for each combination of parameters and the performance of the algorithm is tested in a Monte Carlo simulation.

The DM consists of a square grid of $m_1 \times m_1$ actuators with Gaussian influence func-

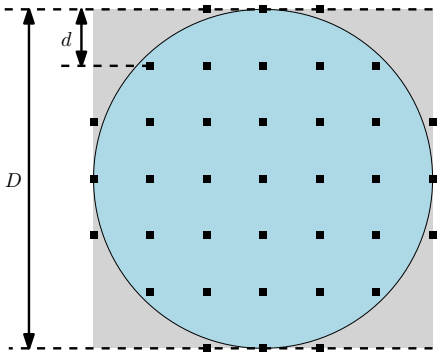

Figure 4.3: Actuator placement for $m_1 = 7$. The $m = 37$ active actuator centers are represented by ■. This center serves as the local origin of this actuators' influence function (i.e. $\chi_1 = \chi_2 = 0$ in (4.34)).

tions:

$$E_i(\boldsymbol{\chi}) = e^{\ln(\lambda)\left((\chi_1^2+\chi_2^2)/d\right)^2}, \tag{4.34}$$

where d is the distance between actuators in the pupil plane and $\lambda > 0$ is the coupling parameter, defining the width of the functions. A schematic representation is shown in Figure 4.3. During the simulations, $m_1 = 7$, $\lambda = 0.1$ and $d = D/(m_1 + 1) = 0.125$ m. The actuators at the corners of the square are removed since they have little influence inside the circular aperture, such that in total of $m = 37$ active actuators are used. The influence of the actuator on the closed-loop aberration is simulated as in (4.20).

The PSF images are simulated according to the definition in (4.1) and sampled on an equally spaced square grid. As a result, the SM of this discretized image becomes a weighted sum of the PSF pixel values.

4.4.2. MEASUREMENT NOISE

The camera noise in each pixel can be modelled as a combination of Gaussian (read-out noise) and Poissonian noise (shot noise). For pixels with large mean values, Poisson distributions can be accurately approximated by a Gaussian distribution. For small pixel values, the influence of the shot noise becomes less significant with respect to the Gaussian read-out noise. Furthermore, low-valued pixels have a very low SNR and are therefore often truncated when processing the images. Since the SM is a weighted sum of the pixel values, the noise contribution to the SM is expected to be approximately Gaussian and can be estimated based on the intensity measurement and camera properties.

In practice, methods such as truncation of low-valued pixels and filtering have to be used to decrease the effect of the measurement noise on the SM. However, it has been decided that this will not be included in the analysis. Instead, in order to have a clear analysis of the noise sensitivity of the algorithm itself, the noise signal $\boldsymbol{v}(kT)$ will be simulated directly as a Gaussian noise, $\boldsymbol{v}(kT) \sim \mathcal{N}(0, \sigma_y^2 I)$.

4.5. SIMULATION RESULTS

The results of the simulations will be discussed in this section. A number of parameters will be varied in order to study the performance of the methods under different circumstances. First, the wind velocity, v, is varied to see whether the improvements of the new method are indeed more clear for faster moving turbulence. Second, the Fried parameter, r_0, is changed to see which method is better to deal with more severe aberrations. Third, the influence of increasing the number of actuators that is updated per measurement, p, is discussed. Finally, the noise sensitivity is analyzed by varying the parameter σ_y in the measurement noise covariance $R = \sigma_y^2 I$. The rest of the parameters will be kept constant in order to have a fair comparison. The standard values of the parameters can be found in Table 4.2.

In the legends of the figures, the new method will be referred to as "Dynamic SM", as it includes a temporal dynamic model of the aberrations plus the SM model (4.10). It is compared to an existing method [14], which is referred to as "Static SM", as it is based on the assumption that the change in aberration between two input sampling times is negligible, i.e., the aberration is approximately static over this time period. The parameter β is seen as an important tuning parameter in both methods. When β is taken too small, the SNR will be very low. Too large values of β will create too many speckles in the PSF for the output to still be informative. Therefore, it has an optimal value that depends on the current simulation conditions and measurement noise level. During the following simulations, β has been tuned for each different set of parameters using a grid search in order to improve the performance for both the static and dynamic SM-based method.

The main goal is to decrease the effect of the aberration on the image. Therefore, the Strehl ratio is used as a measure of performance. The Strehl ratio is computed as the fraction of the maximum pixel value of the aberrated PSF over the maximum pixel value of the unaberrated PSF. A higher Strehl ratio indicates a better performance. Also, since the method is based on minimizing the SM of the PSF, this will be occasionally used as a measure. Since each simulation takes N time samples, the mean Strehl value and SM for each simulation will be used and the Monte Carlo simulation is visualized in boxplots.

4.5.1. INCREASING WIND SPEED

It is expected that the new method, due to its predictive capabilities and smart actuator selection algorithm, can handle much larger wind speeds than the static method for the same AO system. It should be noted that for both the static and dynamic SM-based methods, besides the Fried parameter r_0 and sample frequency f_s, the performance at a certain wind speed is influenced by the number of actuators m and the spatial sample distance of the actuators d. This is due to the fact that only one actuator can be poked at the same time. So when m is increased, more modes have to be updated within the same time span, and when d is decreased, the turbulence is moving the distance between actuators in a shorter time. Therefore, in order to improve the performance under larger wind speeds or when increasing the number of DM actuators, it might be necessary to increase the sample frequency f_s. For the simulations in this paragraph, m and f_s are fixed at the values in Table 4.2.

The wind speed is varied between 0.2 and 16 m/s and the other parameters are kept

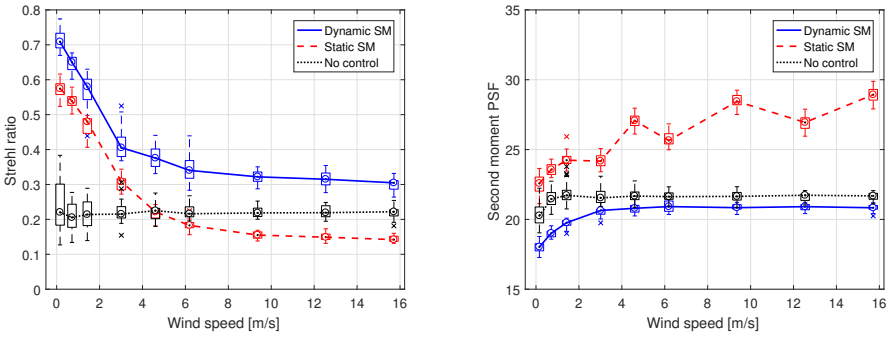

(a) Mean Strehl ratio

(b) Mean second moment of the PSF

Figure 4.4: Results for varying the wind speed. The other simulation parameters are given in Table 4.2. "Dynamic SM" represents the method presented in this chapter, "Static SM" is the existing method presented in [14]. The boxes indicate the 25th and 75th percentile of the results in the Monte Carlo simulation and the lines are drawn through the medians.

constant at their standard values according to Table 4.2. The results of this simulation are shown in Figure 4.4. From observing the Strehl ratio in Figure 4.4a, the new method is clearly better, most notably for higher wind speeds. Even for lower wind speeds, the new method outperforms the existing approach. This can be explained by the fact that the Kalman filter is more suited in dealing with measurement noise. In Figure 4.4b, the SM of the PSF is shown. Even when the static method improves the image quality in terms of the Strehl ratio at lower wind speeds, the SM of the PSF is larger than in the case without adaptive optics. This is caused by the fact that under the noisy conditions in this simulation, the static method introduces high-frequency aberrations erroneously in the compensation. The oscillating trend of the static method's line is due to the different step lengths of the interpolation when generating the wavefront data as discussed in Section 4.4.1. Interpolation of a time-varying aberration has in general a smoothing effect on the SM of the aberrated PSF. This effect is usually very small, as is seen in the line corresponding to no control, but seems to be amplified by the static method. Since this smoothing effect can be seen as a small amount of noise on the data, this issue indicates again the high noise sensitivity of the static method compared to the dynamic method.

It should be noted that due to the small number of DM actuators, the fitting error is relatively large and the maximum achievable Strehl ratio for this AO configuration is approximately 0.83. So at very low wind speeds the new method approaches the theoretical optimum. In order to improve the theoretical maximum closed-loop performance, the fitting error should be decreased by using a DM with more actuators. However, as discussed in the beginning of this paragraph, having more actuators within the same size aperture corresponds to more modes to be updated in the same time. This would require that also the sample frequency f_s is increased in order to maintain a good performance for high wind speeds.

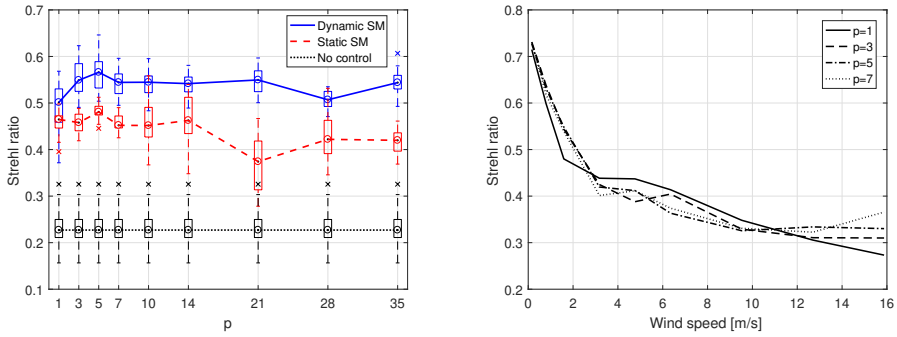

(a) Varying p for both the dynamic and the static method.

(b) Varying p and v for the dynamic method only.

Figure 4.5: Results of the new algorithm for different values of p. (a) p is varied while all the other parameters are kept at their standard values given in Table 4.2. The presentation of the results is similar to Figure 4.4. (b) Influence of the wind speed on the best choice of p, only the median Strehl ratio over the Monte Carlo simulations are shown.

4.5.2. NUMBER OF IMAGES IN OUTPUT

In the previous simulation it was assumed that $p = 3$ such that three output channels are observed within one output sample time. The method allows for any p that satisfies $1 \leq p \leq m$. Varying p can possibly lead to a better performance and needs to be investigated. Decreasing p corresponds to a smaller output sampling time T, having the advantage that the measurement updates are more frequent. However, the drawback is that, since per $(p+1)T_i$ seconds p output channels are created, more time is spent per acquired output channel when p is small. On the other hand, increasing p increases the output sampling time T, but means that less time is spent per acquired output channel. For the sake of a complete comparison, a multivariate output is also considered for the existing method of [14]. It should be mentioned that in the original method, varying p was not discussed and p was chosen to equal 1.

The results for varying p while keeping the other parameters equal to their standard value in Table 4.2, is shown in Figure 4.5a. It clearly shows how $p = 1$ is not the optimal value in this case, but larger values are more optimal. The effect of p for other wind speeds is shown in Figure 4.5b. Only the medians over the Monte Carlo runs are plotted. Although all lines have similar trends, it is visible that $p = 1$ does not always lead to the best results. Especially in the region where the wind speed is low, $p = 5$ is better than $p = 1$ as was also clear from Figure 4.5a.

The effect of the actuator selection method described in Section 4.3.4 is very clearly visible in Figure 4.6. For the same actuator configuration as in Figure 4.3 and a single turbulence layer moving from left to right over this aperture, this figure shows the amount of times a certain actuator was deemed to be in the set of most informative actuators. The actuators located at the edge where the new turbulence comes in are much more regularly chosen than the other actuators. This is expected, since the aberration towards the center and right side of the aperture is merely a shift of the wavefront at a previous time instance. The aberration at the left side of the aperture was unknown at this previ-

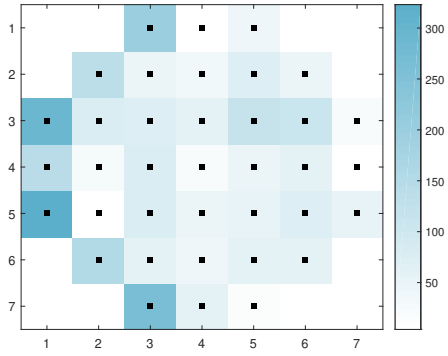

Figure 4.6: Example of the most often selected actuators by the method described in Section 4.3.4. The simulation parameters equal to the standard values in Table 4.2 with $N = 1000$ sample times and the configuration of the DM is as in Figure 4.3. The color scale displays how many times this actuator was chosen to be part of the subset $\mathscr{I}$.

ous time instance and more difficult to model.

4.5.3. STRONGER ABERRATIONS

As the aberrations become more severe, the PSF images will become more distorted. Therefore, a decrease in performance is expected for any algorithm. If the same performance for a lower Fried parameter is desired, the number of actuators have to be increased. Figure 4.7 shows the performance of the method for r_0 varying between 0.1 m and 0.35 m while all other parameters are fixed at their standard value given in Table 4.2. The top line indicated by "DM optimal" corresponds to a controller that assumes perfect knowledge of the residual wavefront and maps it onto the DM. So it represents the theoretical optimal performance when using this DM. When the turbulence strength increases, the performance of both methods decreases as expected. Especially turbulence strengths $r_0 \geq 0.2$, the new method clearly outperforms the existing method.

4.5.4. NOISE SENSITIVITY

As discussed before, the influence of the camera noise on the SM will be approximately Gaussian. Therefore, the Gaussian measurement noise is added to the output $\boldsymbol{y}(kT)$ in order to simulate noisy conditions. In these results, the measurement noise variance is supposed to be known. In practice, this must be calibrated based on the exact noise properties of the camera and PSF intensity. The influence of the measurement noise on the results is shown in Figure 4.8. For low noise, i.e. $\sigma_y \leq 0.1$, the existing method has an advantage. When there is a significant measurement noise, which will be the case in any practical system, the new method is clearly better. This is expected since the Kalman filter is designed to optimally deal with measurement noise, whereas the original method ignored any noise present in the system.

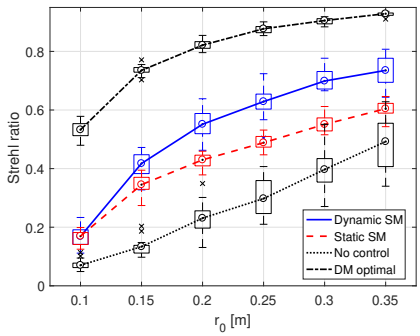

Figure 4.7: The Strehl ratio for different values of the Fried parameter r_0. The presentation of the results is similar to Figure 4.4. The line indicated by "DM optimal" displays the maximum possible performance of the DM for each turbulence strength.

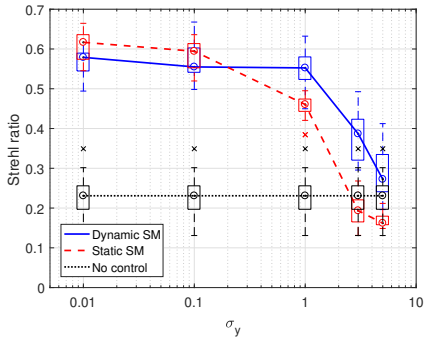

Figure 4.8: The Strehl ratio for different measurement noise values. The presentation of the results is similar to Figure 4.4.

4.6. CONCLUSION

A method has been presented to extend the SM-based WFSless AO to the case of time varying aberrations. It combines the knowledge of an accurate temporal model of the aberration dynamics with the linear relation between the SM of the PSF and the mean square of the residual phase aberration. The result is that the AO problem can be cast into a Kalman filtering and optimal control problem. Where all previous methods had to update the actuators sequentially, the new algorithm automatically selects the actuators that are expected to lead to the most informative update. Actuators placed at locations where the model is accurate can be updated with only a small number of images over time. The improved performance has been shown in a simulation study of an AO system for atmospheric turbulence. It was shown that the new method leads to an improved performance for both lower and higher wind speeds and for higher noise levels.

REFERENCES

[1] M. A. Vorontsov, G. W. Carhart, M. Cohen, and G. Cauwenberghs, *Adaptive optics based on analog parallel stochastic optimization: analysis and experimental demonstration,* Journal of the Optical Society of America A **17**, 1440 (2000).

[2] S. Zommer, E. Ribak, S. Lipson, and J. Adler, *Simulated annealing in ocular adaptive optics,* Optics Letters **31**, 939 (2006).

[3] P. Yang, M. Ao, Y. Liu, B. Xu, and W. Jiang, *Intracavity transverse modes controlled by a genetic algorithm based on zernike mode coefficients,* Optics Express **15**, 17051 (2007).

[4] Q. Yang, J. Zhao, M. Wang, and J. Jia, *Wavefront sensorless adaptive optics based on the trust region method,* Optics Letters **40**, 1235 (2015).

[5] C. E. Carrizo, R. M. Calvo, and A. Belmonte, *Intensity-based adaptive optics with sequential optimization for laser communications,* Optics express **26**, 16044 (2018).

[6] X. He, X. Zhao, S. Cui, and H. Gu, *A rapid hybrid wave front correction algorithm for sensor-less adaptive optics in free space optical communication,* Optics Communications **429**, 127 (2018).

[7] Y. Shechtman, Y. C. Eldar, O. Cohen, H. N. Chapman, J. Miao, and M. Segev, *Phase retrieval with application to optical imaging: a contemporary overview,* IEEE signal processing magazine **32**, 87 (2015).

[8] R. Doelman, N. H. Thao, and M. Verhaegen, *Solving large-scale general phase retrieval problems via a sequence of convex relaxations,* Journal of the Optical Society of America A **35**, 1410 (2018).

[9] H. Linhai and C. Rao, *Wavefront sensorless adaptive optics: a general model-based approach,* Optics express **19**, 371 (2011).

[10] H. Yang, O. Soloviev, and M. Verhaegen, *Model-based wavefront sensorless adaptive optics system for large aberrations and extended objects,* Optics express **23**, 24587 (2015).

[11] W. Lianghua, P. Yang, Y. Kangjian, C. Shanqiu, W. Shuai, L. Wenjing, and B. Xu, *Synchronous model-based approach for wavefront sensorless adaptive optics system,* Optics express **25**, 20584 (2017).

[12] C. Kulcsár, H.-F. Raynaud, C. Petit, J.-M. Conan, and P. V. De Lesegno, *Optimal control, observers and integrators in adaptive optics,* Optics express **14**, 7464 (2006).

[13] K. Hinnen, M. Verhaegen, and N. Doelman, *A data-driven $\mathscr{H}_2$-optimal control approach for adaptive optics,* IEEE Transactions on Control Systems Technology **16**, 381 (2008).

[14] W. Lianghua, P. Yang, W. Shuai, L. Wenjing, C. Shanqiu, and B. Xu, *A high speed model-based approach for wavefront sensorless adaptive optics systems,* Optics & Laser Technology **99**, 124 (2018).

[15] O. Soloviev, *Optimal basis for modal sensorless adaptive optics,* arXiv:1707.08489 (2017).

[16] M. Verhaegen and V. Verdult, *Filtering and system identification: a least squares approach* (Cambridge university press, 2007).

[17] R. Conan and C. Correia, *Object-oriented matlab adaptive optics toolbox,* in *Adaptive optics systems IV*, Vol. 9148 (International Society for Optics and Photonics, 2014) p. 91486C.

5

CONCLUSIONS AND FUTURE RESEARCH

5.1. CONCLUSIONS

This thesis has presented several methods for the estimation of large-scale and/or time-varying wavefronts using focal-plane sensing methods. Each of these methods have their own motivations and contributions, which have been discussed in the corresponding chapters.

In Chapter 2 Gaussian radial basis functions (GRBFs) were used as a modal representation of the GPF. The advantage of a modal basis is that the number of parameters in the phase retrieval problem can be decreased, making modal representations a suitable candidate for wavefront reconstruction for large-scale AO. The GRBFs showed an increased reconstruction accuracy with respect to extended Nijboer-Zernike polynomials for aberrations with high spatial frequencies and for non-circular aperture shapes.

Where Chapter 2 only considered phase retrieval of static aberrations, Chapters 3 and 4 presented focal-plane sensing techniques for time-varying aberrations. In addition, it was assumed that a single focal-plane image was available per time-step. Chapter 3 presented an algorithm for high-resolution time-varying wavefront estimation. Assuming a phase that is small enough, this algorithm is based on an extension of the phase retrieval framework for dynamic aberrations by reformulating it into a non-linear Kalman filtering framework. A computationally efficient non-linear Kalman filter was developed whose computational complexity scales close to linearly with the number of pixels of the wavefront reconstruction.

A different approach to focal-plane sensing from a single image, which does not explicitly consider the phase retrieval problem, was used in Chapter 4. This method was based on the linear relation between the mean square of the aberration gradient and the change in second moment of the PSF, which was then extended to the case of time-varying aberrations. By using a modal basis that spans the same space as the actuator influence functions, the actuators can be updated sequentially. A Kalman filter is used to

design an optimal controller that selects the modes that are expected to give the greatest increase in performance.

The remainder of this chapter can be seen as a discussion regarding the main conclusions and limitations with respect to the motivation of this thesis, followed by a number of suggestions for future research. As presented in Section 1.6, the motivation of this thesis was to develop algorithms that are able to: *use temporal dynamics as a source of useful information* and/or *deal with large-scale AO systems*.

USING TEMPORAL DYNAMICS AS A SOURCE OF USEFUL INFORMATION

The methods presented in Chapters 3 and 4 fall within this category. The presence of temporal dynamics at first seems to be an additional challenge on top of the already complicated focal-plane sensing problem. In these methods, however, the available knowledge of the aberration dynamics is used to their advantage, making them frequently outperform the static methods in the case of quasi-static aberrations.

In Chapter 3, the similarities between the (static) phase retrieval problem and Kalman filtering were discussed. It was argued how the Kalman filter can be seen as a optimally weighted regularized version of classic non-linear least squares underlying the phase retrieval problem. By adopting this reformulation, the issue of non-uniqueness of the phase retrieval problem was shown to be transformed into the, often less restrictive, notion of observability. As a consequence, the Kalman filter is able to obtain an accurate reconstruction using a single focal-plane image only, which is often not possible using focal-plane sensing methods that assume a static wavefront. Although adding a small known defocus to the captured images was shown to significantly improve the performance, even a single in-focus measurement of the PSF often resulted in an accurate wavefront reconstruction.

The Kalman filter relies on the availability of accurate prior information and, hence, on the availability of an accurate model of the wavefront dynamics. If the model is not accurate enough, errors in the prior information used by the Kalman filter measurement update might result in a significant increase of the estimation error. Obtaining such a model is not trivial as it needs to be identified from data. In practice, this puts a limit on the severeness of the wavefront dynamics that can be compensated for, as faster evolving aberrations are typically more challenging to model. Taking the example of aberrations caused by atmospheric turbulence and assuming a frozen flow representation of the phase screens, a measure of the severeness of the dynamics from the perspective of the algorithms is given by the average shift of the phase screens in terms of pixels widths per sampling time. So, for faster wind speeds, decreasing the resolution, i.e. increasing the pixel width, or increasing the sampling frequency, could be ways to improve the accuracy of the dynamic model.

The alternative model-based WFSless AO approach, which used the linear relation between the change in second moment of the PSF and the mean square of the aberration gradient, was extended in order to take the aberration dynamics into account in Chapter 4. In this algorithm, the knowledge of the temporal evolution incorporated in the Kalman filter was used to select the modes, in this case the actuators, to be updated at each sampling time. The remaining modes were updated according to the model of the wavefront dynamics.

An interesting phenomenon was observed, in which the actuators that were located on the edge of the aperture were updated much more frequently than the ones at the center. When assuming aberrations whose temporal evolution have a shifting nature, prediction of the wavefront around the aperture's edges is more challenging, as less information is available. Hence, the results coincide with what intuitively would be expected.

A consequence of this smart updating scheme is that fewer modes have to be updated based on measurements in comparison to a simple sequential updating scheme. As the method is intrinsically limited by the sample time of the focal-plane camera, less frequent measurement updates for modes that can rely on the (open-loop) time updates, means that the algorithm can be used for aberrations that have a significantly faster temporal evolution. However, relying too much on the time updates will result in a significant decrease in the accuracy of the wavefront prediction. Within a certain time span, a minimum amount of measurements have to be taken in order to reach a certain desired accuracy since a perfect model will never be available. This number (for example in number of measurements per second) depends on the wind speed, total number of modes to be estimated and the accuracy of the dynamic model. In practice, this results in the fact that this class of model-based WFSless AO methods is mainly suited for systems with with either slowly evolving aberrations or a small number of basis functions.

DEALING WITH LARGE-SCALE AO SYSTEMS

All the algorithms developed in Chapters 2, 3 and 4 have been developed with computational efficiency in mind. The reduction of parameters in the phase retrieval problem by adopting a modal basis of the GPF in Chapter 2 resulted in a significant decrease in computational complexity. Although effective, this type of complexity reduction has an obvious trade-off with the maximum spatial frequencies that can be reconstructed, as it implicitly decreases the resolution of the reconstruction. It should be stated here that the use of GRBFs is not equivalent to simply reducing the resolution of the reconstruction. Since the smooth set of basis functions acts as a type of smoothness constraint on the phase retrieval problem, the GRBFs are expected to outperform the simple low-resolution pixel basis under noisy circumstances, which is one of the main advantages of a modal representation.

A less straightforward way of reducing the computational complexity is presented by the algorithm of Chapter 3. This method efficiently reconstructs the wavefront in its original resolution by exploiting special matrix structures within the model of the AO system. Other assumptions, however, have to be made in order for this efficient algorithm to work in practice. Most notably, the phase aberrations have to be small enough for the necessary linearizations to hold, making the method suitable for estimating small-phase aberrations only.

The method of Chapter 4 is not limited by such a small-phase approximation. In addition, by reducing the information in the measured images to merely the changes in the second moment, which are scalar values, the computations that need to be performed by this class algorithms are of a much simpler nature than that of phase retrieval-based algorithms. However, the limitations of this method, which were previously discussed, do have consequences on the maximum number of modes (i.e. actuators) for which this

algorithm can be used. Although increasing the sampling frequency of the camera is in theory a method to decrease this limitation, it does not solve this issue, as a decreased time to collect enough photons to capture the image will result in a decreased signal-to-noise ratio. Therefore, the applicability of this method in large-scale AO systems is limited. Especially for aberrations with a fast temporal evolution, this method would only be able to keep up with the estimation of a small number of modes.

5.2. FUTURE RESEARCH

The presented methods in this thesis were all tested in simulations studies. In order to validate the true performance of the algorithms, further testing under more realistic circumstances, such as in laboratory experiments, is required. Although the methods were designed with the application of AO for astronomy in mind, the methods are not limited nor specifically designed for this application. Their applicability in other areas such as microscopy and ophthalmology or for modelling spatial instead of temporal dynamics (e.g. due to anisoplanatic conditions in astronomy) can be an interesting research direction. Besides these general recommendations, the remainder of this chapter will discuss a number of specific topics that could be of interest. Some of the ideas presented have already been investigated during the development of this thesis, and might lead to additional publications in the near future.

SPARSE KALMAN FILTER FOR WFS-BASED AO

Although the focus of this thesis has been on focal-plane wavefront sensing, AO systems with a dedicated pupil-plane WFS still require more research into the development of computationally efficient predictive algorithms. Due to the linear relation between the WFS signal and phase aberrations, WFS-based methods are, for many applications, still preferable over focal-plane sensing methods. During this thesis, the development of efficient Kalman filtering for WFS-based techniques by exploiting sparsity has been investigated. It was decided to not include this research as a chapter of this thesis, but a journal publication is currently under preparation:

Cerqueira, P., Piscaer, P., Verhaegen, M. *Sparse Data-Driven Wavefront Prediction for Large-Scale Adaptive Optics*, JOSA A, (2021)

The main idea in sparse Kalman filters for WFS-based AO is similar to the graphical modelling approach that underlies the sparsity when modelling the wavefront. Due to the local nature of each entry in the SH-sensor measurement vector, a sparse vector auto-regressive (VAR) model similar to the one that was used to describe the temporal evolution of the phase aberrations, can be used to describe the temporal evolution of the output of the WFS-based state-space model (i.e. the SH-signal). As the coefficient matrices of this VAR model can be seen as the Markov parameters of the state-space model, they can be used in the derivation of the Kalman gain.

Unfortunately, the Kalman gain itself is per definition not sparse. The gain describes the relation between the SH-signal, which are the local spatial gradients of the wavefront, and the wavefront itself, such that it can be interpreted as some kind of integration op-

erator. In order to capture global shapes in the wavefronts, e.g. low-order Zernike modes such as tip-tilt, defocus and astigmatism, the Kalman gain should therefore be dense.

The main idea that was pursued in this research is that, although the Kalman filter itself has to be dense in order to capture global modes, a sparse approximation of the Kalman filter might still accurately approximate the local shapes of the wavefront. According to this hypothesis, the main approximation error should mainly consist of low spatial-frequency modes, which could be compensated for by a secondary low-resolution dense Kalman filter. In this manner, a two-step approach is obtained. First, an approximate sparse Kalman gain is used to estimate the high-spatial frequency content in high resolution. Second, a small-scale dense Kalman filter is used to estimate the remaining approximation error, which is expected to contain mainly low spatial-frequency modes.

SYSTEM IDENTIFICATION FOR SINGLE FOCAL-PLANE CAMERA SYSTEMS

An important challenge, which was only briefly addressed in this thesis, is the development of a realistic and systematic method to obtain an accurate dataset containing a time-series of the wavefront aberrations necessary for the system identification step. Errors in the identification dataset will inevitably result in modelling errors, which decrease the accuracy of the wavefront estimation. As the methods of Chapters 3 and 4 assume a single focal-plane camera only and no WFS, obtaining this data-set without or with only limited hardware changes is not trivial. When choosing the identification data collection method, it is therefore important to take into account the hardware changes that have to be made.

The data collection and the corresponding wavefront reconstruction, using either focal-plane or pupil-plane sensing techniques, can be performed offline. That is, these reconstruction algorithms do not need to be able to reconstruct the wavefront in real-time. This does not mean that the system identification step can take arbitrarily long. Throughout this thesis, the aberration dynamics were represented by a time-invariant model. In reality, the conditions (such as the wind speeds and Fried parameter considering the astronomy application) will themselves slowly change over time. After a certain time, it is therefore necessary to re-identify the model or update it accordingly. Updating the model without opening the loop, e.g. using closed-loop system identification techniques, could be another interesting area for future research.

MULTI-LAYER BASIS AND LOCAL UPDATES USING GRBFS

The modal phase retrieval method in Chapter 2 only considered a small number of configurations in which the GRBFs were placed. Depending on the exact application, there might be other possible configurations that could further improve the performance. Due to the local nature of the GRBFs, it might also be beneficial to not limit oneself to a fixed set of GRBFs with a constant shape.

For example, multiple "layers" of GRBFs could be used, where the first layer contains a small number of wide GRBFs (i.e. having a small shape parameter in Chapter 2), the second layer a slightly larger number of GRBFs with a narrower shape, and so on. Another idea is to constantly update the locations and shapes of the GRBFs based on the expected shape of the wavefront. In areas that seem to contain sharp features or require the modelling of local details, the concentration of GRBFs could be increased and their

shapes could be narrowed. In this way, when applying GRBFs to real-time algorithms, the computational power could be focused on local areas that are most crucial during that specific sampling period.

STRUCTURED MODAL BASIS

The GRBFs used in Chapter 2 were shown to perform best when assuming a planar Fibonacci grid. It should be stressed, however, that its capability to accurately represent the GPF is not the only topic of interest when choosing a modal basis. When the basis has to be used in a real-time algorithm, computational efficiency is equally important.

Although the number of parameters can be decreased when assuming a modal representation of the GPF, it does not guarantee that any modal basis with a smaller number of variables will result in a more efficient solution of the phase retrieval problem. The classic pixel-wise representation of the GPF can be exploited in phase retrieval algorithms such as the alternating projection (AP) methods. The efficient structure of the two-dimensional DFT, which defines the relation between the GPF and PSF, is preserved when maintaining the pixel basis and FFT methods can be use to develop computationally efficient algorithms. For an arbitrary modal representation of the GPF, this structure is often lost and FFT algorithms can no longer be used, making them much slower than the pixel-wise representation of the GPF.

Returning to the example of GRBFs, placing the GRBFs on a regular rectangular grid instead of the Fibonacci grid means that the property of separability of the 2D-DFT can be maintained. For this modal decomposition, the matrix representing the linear relation between the focal-plane image and the modal coefficients, can be expressed using a Kronecker product of two smaller matrices. It is not clear whether there are other structures within this set of basis functions that can be exploited further by either AP methods or any other class of phase retrieval algorithms. If a set of modal basis functions would be found that preserves the efficient structures of the DFT or that possesses a different computationally efficient property, the practical applicability of basis functions in phase retrieval and WFSless AO could be further extended.

OPTIMAL CONTROLLER DESIGN USING NON-LINEAR KALMAN FILTER

Although the results of Chapter 3 present a promising computationally efficient algorithm, there is still much to be done before focal-plane sensing can be used for applications that require real-time compensation of high-resolution dynamic aberrations, as is the case for the new generation of extremely large telescopes. Firstly, the provided algorithm has only been tested in an open-loop setting. An optimal controller can be designed to close the loop based on the predictions of the Kalman filter, but performance and stability of such a controller requires separate research. In a closed-loop scenario, modelling errors and measurement noise can potentially be more problematic and the small-phase assumption can become more challenging to enforce over time. Secondly, even though the method presented showed a significant decrease in run-time and a low computational complexity, the run-time of the implemented algorithm was still not fast enough for real-time application. The development of a practical real-time algorithm would require a separate, more detailed, study into the current computational bottlenecks of the algorithm, and a more efficient software implementation is required to sat-

isfy the desired computation time constraints.

NON-LINEAR KALMAN FILTER FOR ESTIMATING THE GPF

The method in Chapter 3 restricted itself to the case in which the amplitude of the GPF was known exactly and in which only the phase had to be estimated. In principle, the theory could be extended to the case in which the amplitude of the GPF was only approximately known, or even to the estimation of the complex-valued GPF at once. This means dropping the prior knowledge of the amplitude and an additional non-linearity to the state-equation. Developing such an algorithm will, therefore, deal with several new challenges, making this extension far from trivial.

CURRICULUM VITÆ

Pieter Piscaer was born in 1993 in Vlissingen, The Netherlands.

Between 2011 and 2014 he studied a Bachelor in Mechanical Engineering at Delft University of Technology, for which he graduated *cum laude* and successfully finished the Honours Programme. At Delft University of Technology, he also obtained his Masters degree in Systems and Control in 2016. His thesis was titled: "Sparse VARX Model Identification for Large-Scale Adaptive Optics" and he graduated *cum laude*.

He stayed at the Delft Center for Systems and Control of Delft University of Technology to do a PhD, which he started in September 2016. His thesis focused on high-resolution focal-plane wavefront sensing for time-varying aberrations. He investigated computationally efficient algorithms, typically involving Kalman filtering theory, for the application of large-scale ground based telescopes. Additionally, he was a member of the PhD council, supervised several Master thesis projects and was a teaching assistant in Masters courses.

Contact details:

E-mail	piscaer.pieter@gmail.com
LinkedIn	https://www.linkedin.com/in/pjpiscaer/

List of Publications

Journal Publications

Cerqueira, P., Piscaer, P., Verhaegen, M. *Sparse Data-Driven Wavefront Prediction for Large-Scale Adaptive Optics*, JOSA A, (2021)

Piscaer, P., Soloviev, O., Verhaegen, M. *Phase retrieval of large-scale time-varying aberrations using a non-linear Kalman filtering framework*, JOSA A 38, 25 (2021)

Piscaer, P., Soloviev, O., Verhaegen, M. *Predictive wavefront sensorless adaptive optics for time-varying aberrations*, JOSA A, 36, 1810 (2019)

Piscaer, P., Gupta, A., Soloviev, O., Verhaegen, M., *Modal-based phase retrieval using Gaussian radial basis functions*, JOSA A, 35, 1233 (2018)

Conference Publications

Piscaer, P., Soloviev, O., Verhaegen, M. *Challenges in simulating advanced control methods for AO*, Proc. SPIE 11448, Adaptive Optics Systems VII (2020)

Gedon, D., Piscaer, P., Batselier, K., Smith, C., Verhaegen, M. (2019). *Tensor Network Kalman Filter for LTI Systems*. In 27th European Signal Processing Conference (IEEE, 2019).